Tuning in to star-planet interactions at radio wavelengths

Proefschrift

ter verkrijging van
de graad van doctor aan de Universiteit Leiden,
op gezag van rector magnificus prof.dr.ir. H. Bijl,
volgens besluit van het college voor promoties
te verdedigen op dinsdag 15 november 2022
klokke 11:15 uur

door

Robert D. Kavanagh
geboren te Dublin, Ireland
in 1995

Promotores:
Dr. A. A. Vidotto
Prof.dr. I. A. G. Snellen

Promotiecommissie:
Prof.dr. H. J. A. Rottgering
Prof.dr. S. F. Portegies Zwart
Dr. Y. Miguel
Prof.dr. M. Güdel (University of Vienna)
Dr. H. K. Vedantham (ASTRON/University of Groningen)

ISBN 978 94 6419 617 7

Cover design by Robert Kavanagh. Planet texture: Solar System Scope. Background image: ESO/Davide De Martin.

Table of contents

1 | Introduction

1.1 The discovery of the solar wind

The first suggestion that the Sun, our closest star, is a source of outflowing hot magnetised plasma came from the Norwegian physicist Kristian Birkeland in the early 1900s, who illustrated a striking similarity between the results of his experiments firing beams of electrons at a spherical magnet and the Northern Lights (Birkeland, 1908). This idea was further reinforced by Biermann (1951), who proposed that the formation of Type I tails from comets could be explained by outflowing ionised plasma from the Sun at supersonic speeds of ~ 1000 km s^{-1}, which we now know as the *solar wind.* In the meantime, evidence began to mount supporting the existence of the solar corona shown in Figure 1.1, the million degree Kelvin (K) region of the Sun's upper atmosphere (Grotrian, 1939; Alfvén, 1941; Edlén, 1945). It was Parker (1958) who first linked the idea of a hot corona to a continuously outflowing solar wind in a self-consistent way.

Parker's approach was simple but very effective. He described the solar wind as being driven by a strong thermal pressure gradient set by the hot corona, offset by the gravitational pull of the Sun. By assuming that the solar wind is isothermal (i.e. the temperature does not change with distance), maintains a negative pressure gradient, and is an ideal gas, Parker derived a differential equation describing the momentum of the solar wind outflow. While Parker found that there were a family of solutions to this equation, only one described a solar wind outflow that monotonically increased in velocity outwards, transitioning from a subsonic regime to a supersonic regime. This was in agreement with the likes of Biermann (1951), who suggested the same scenario for a supersonic solar wind outflow.

While Parker's solar wind solution was initially met with strong criticism, measurements obtained by the Mariner 2 spacecraft in 1962 quickly put to rest any doubts about its existence (Neugebauer & Snyder, 1966). At 1 au, Mariner 2 detected a solar wind outflow with a supersonic velocity of 500 km s^{-1} and a proton density of 5 cm^{-3} on average. Integrating the mass flux over 4π steradians, the solar wind mass-loss rate measured by Mariner 2 was $\sim 6 \times 10^{11}$ g s^{-1}, in close agreement with the now-accepted value of 2×10^{-14} $M_\odot$ yr^{-1} (Feldman et al., 1977; Cohen, 2011; Finley et al., 2019). Parker's solar wind solution for a coronal temperature of 1 MK and mass-loss rate of 2×10^{-14} $M_\odot$ yr^{-1} gives values that are in fantastic agreement with those obtained by Mariner 2 at 1 au, with a predicted velocity and density of 485 km s^{-1} and 5.5 cm^{-3} respectively. The velocity and density profile obtained using his prescription is shown in Figure 1.2.

Our understanding of the solar wind has advanced significantly since the 1960s, thanks to a multitude of in-situ measurements (Verscharen et al., 2019) and evermore sophisticated modelling (for a review, see Gombosi et al., 2018). In terms of modelling, the most significant improvements have been the inclusion of rotation and magnetic fields, aspects which were lacking in the initial model of Parker (1958). While Parker (1958) commented on the likely morphology of the large-scale solar magnetic field (the Parker spiral), it was Weber & Davis (1967) who first provided a solar wind model which accounted for these effects in a self-consistent way. Weber & Davis (1967) illustrated that the Sun loses angular momentum, both through the solar wind outflow, as well as via the torque of the large-scale field magnetic field acting on the wind. Understanding the angular momentum loss-rate of the Sun tells us how it will spin down over time (Gallet & Bouvier, 2013; Ó Fionnagáin & Vidotto, 2018; Vidotto, 2021).

The Sun is magnetised at its surface, and therefore any fluid prescription for the solar wind outflow is governed by magnetohydrodynamics (MHD). Its magnetic field is also not a perfect dipole, but contains fine structure and non-uniformities, requiring a 3-dimensional analysis. Another main improvement to theoretical understanding of the solar wind outflow is a prescription for the energy that drives it. Known as the ‘coronal heating problem’, it is an outlying problem in plasma physics as to what ultimately heats the solar corona to a million degrees K. A widely-accepted solution to this problem is that the energy source is the dissipation of Alfvén waves, which are mechanical waves that travel along magnetic field lines (Alfvén, 1942). Observations of Alfvén waves in the upper regions of the Sun's atmosphere seem to support this hypothesis (De Pontieu et al., 2007; McIntosh et al., 2011). Following this, a 3D MHD solar wind model was developed that is driven by the dissipation of Alfvén waves, known as the AWsom Solar Model (AWSoM, Sokolov et al., 2013; van der Holst et al., 2014). AWSoM has been used to successfully reproduce images of the solar corona in extreme UV (EUV), as shown in Figure 1.3.

1.2 Interactions between the solar wind and the planets

With the discovery of the solar wind, we soon began to understand its interactions and effects on the solar system planets. The most well-known example on Earth is the Northern/Southern lights, also known as the aurora borealis/australis, or more generally, aurorae (shown in Figure 1.4). From as early as the 1700s, it was understood that their appearance in the night sky generally followed the phenomenon of so-called ‘magnetic storms’, which were thought to be some kind of perturbation of the Earth's magnetic field (Stern, 1989). We now understand their formation on Earth as a result of the Dungey cycle (Dungey, 1961), which describes how the magnetic field carried by the solar wind compresses the nightside of the Earth's magnetic field (also known as the magnetotail), causing magnetic reconnection to occur. A sketch of this process is shown in Figure 1.5.

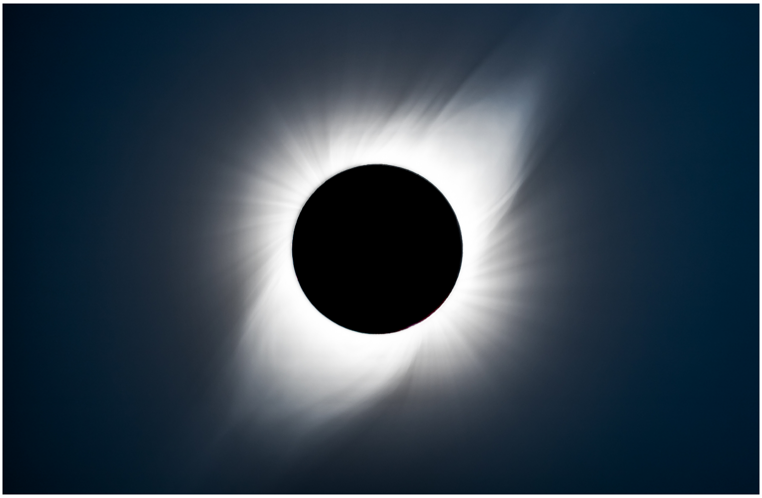

Figure 1.1: Image of the Sun's corona taken during the total solar eclipse on July 2nd 2019 near La Silla observatory in Chile. The dipolar structure of the Sun's magnetic field threading the coronal plasma can be seen clearly. Image credit: Joe Llama.

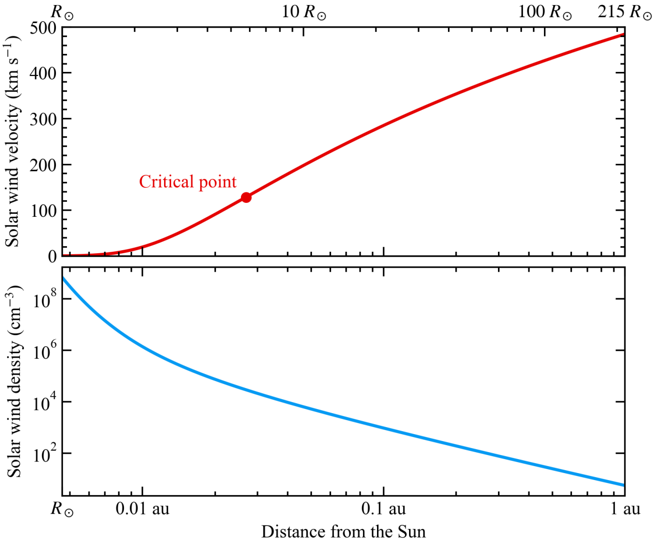

Figure 1.2: *Top*: Velocity profile of the solar wind from the solar surface to 1 au $\equiv 215\ R_\odot$ (the orbital distance of Earth), obtained using the solution from Parker (1958) for a temperature of 1 MK (numerical code developed by Kavanagh & Vidotto, 2020). The critical point, where the solar wind becomes supersonic, is marked. *Bottom*: Density profile of the solar wind for a mass-loss rate of 1.261×10^{12} g s^{-1}.

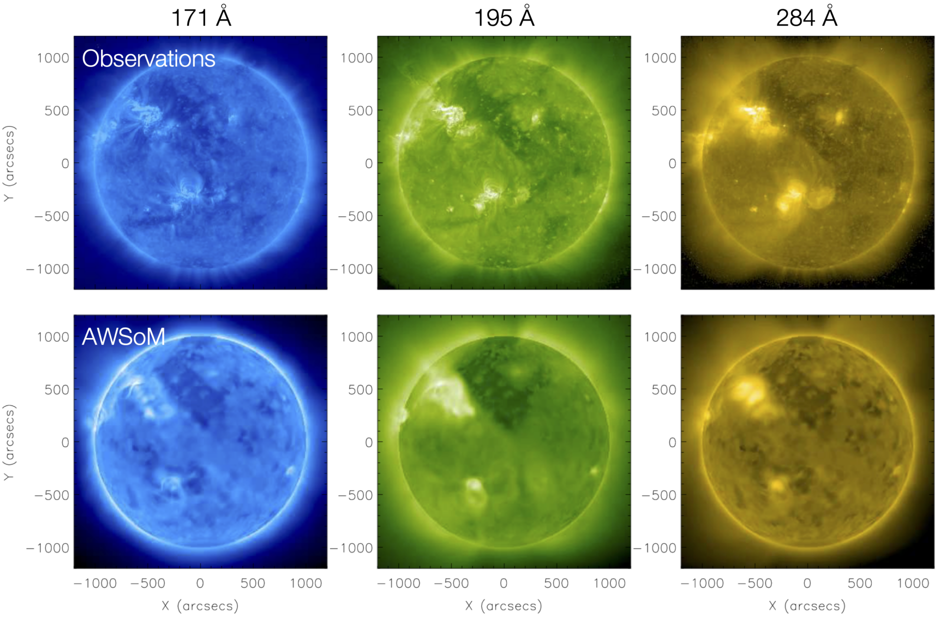

Figure 1.3: Comparison of the solar corona imaged at 3 EUV wavelengths with the STEREO-A satellite on March 11th 2007 (top panels) to those produced with the Alfvén wave-driven solar wind model AWSoM (bottom panels). Figure adapted from van der Holst et al. (2014).

Figure 1.4: The Earth's aurora as seen from the surface over Adventdalen, Svalbard, at a latitude of 78.2 degrees North. The distinct green colour is clearly visible, which is formed via state transitions in oxygen that occur due to the collision of electrons accelerated in the Earth's magnetotail with the atmosphere (He et al., 2020). Image by Sean Coney.

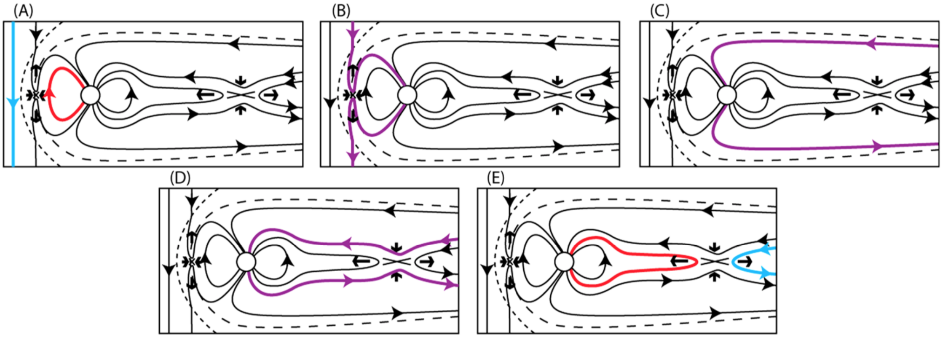

Figure 1.5: Sketch depicting the formation mechanism for the aurorae on Earth proposed by Dungey (1961). Panel A depicts the solar wind magnetic field (blue) interacting with and opening the Earth's magnetic field at the nose of its magnetopause (red). In panels B to D, the two components of this now-open field line (purple) are pushed back towards the magnetotail in the Earth's magnetosphere (right-hand side of each panel). Finally, these two lines reconnect in the magnetotail, releasing energy which accelerates electrons towards the Earth's magnetic pole (red) and into the plasma sheet (blue). The injection of these high-velocity electrons into the Earth's polar regions is thought to be the main driver of the aurorae. Figure from Eastwood et al. (2015).

The energy released during reconnection events in the Earth's magnetotail accelerates electrons towards the magnetic poles of the Earth, resulting in emission across the electromagnetic spectrum. These electrons collide with atoms and molecules in the Earth's upper atmosphere, producing visible light with the distinct red, green, and blue colours that are commonly associated with the aurorae (He et al., 2020), as well as at infrared wavelengths (Espy et al., 1988). Higher energy emission at UV (Paresce, 1979) and X-ray wavelengths (Bhardwaj et al., 2007) is also generated in the Earth's auroral zones, via charge exchange and thermal emission processes respectively. At lower frequencies, the introduction of high-velocity electrons into the polar regions is thought to produce kHz radio emission via the electron cyclotron maser instability (Lamy et al., 2010), which generates 100% circularly polarised radio emission (Dulk, 1985).

Aurorae are not limited to the Earth's magnetic field. In fact, they are ubiquitous in the magnetic polar regions of all the magnetised solar system planets (Mercury, Earth, Jupiter, Saturn, Uranus, and Neptune). It was not until the Voyager spacecraft ventured out into the solar system however that we first learned of their existence on the giant planets, primarily at radio and UV wavelengths (Zarka, 1998; Grodent, 2015). Mercury on the other hand has not been found to exhibit aurorae, primarily due to its lack of an atmosphere (Saur et al., 2021). In Figure 1.6, I show a comparison of the experiments performed by Kristian Birkeland in the early 1900s to Jupiter's aurora imaged in the UV by the Hubble Space Telescope.

Subsequent observations have found that the aurorae of the other magnetised solar system planets appear across the electromagnetic spectrum in a same manner to Earth (Badman et al., 2015). For Jupiter and Saturn, dedicated missions

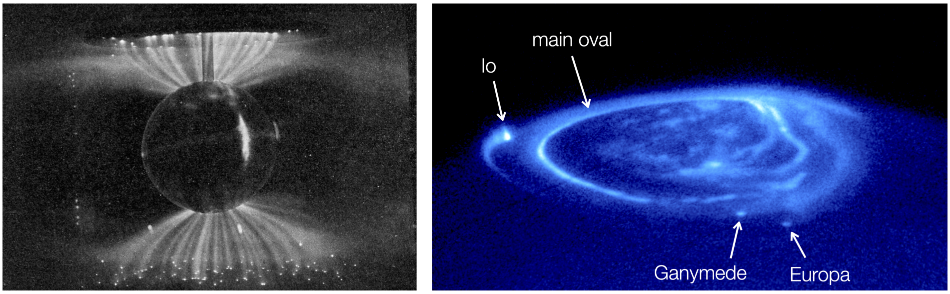

Figure 1.6: *Left*: Photograph of Kristian Birkeland's 'terrella' experiment, wherein he fired an electron beam at a spherical magnet inside a vacuum chamber to investigate the formation of the aurora on Earth. Note the formation of bright rings near the magnetic poles (from Birkeland, 1908). *Right*: UV image of the aurora at Jupiter's North pole, taken with the Hubble Space Telescope (NASA/ESA, John Clarke). The main auroral oval is indicated, along with the footpoints of the field lines of Jupiter connecting to the moons Io, Ganymede, and Europa. The footpoint of Callisto is thought to be obscured by the main auroral oval (Saur et al., 2013).

such as Galileo, Juno, and Cassini have revealed the complexities relating to the formation of their aurorae (see Grodent, 2015; Stallard et al., 2019; Bonfond et al., 2020; Zarka et al., 2021). For Uranus and Neptune however, our understanding of their aurorae is currently limited to the data obtained by the Voyager satellites (Lamy, 2020). Irrespective of these technicalities, the auroral emission of the magnetised planets at radio wavelengths seems to be controlled by the solar wind power incident on their magnetospheres (Desch & Kaiser, 1984; Zarka, 2007). This relation is known as the 'radiometric Bode's law', which is shown in Figure 1.7. At low frequencies ($<$ 100 MHz), Jupiter's auroral emission outshines the Sun by over three orders of magnitude (Zarka, 2007).

Although not directly linked to interactions with the solar wind, prominent features in Jupiter's aurora are bright spots associated with the magnetic field lines linking the planet to its moons Io, Europa, and Ganymede, as shown in the right panel of Figure 1.6. These are thought to be powered by sub-Alfvénic interactions between the moons and Jupiter, which perturb the Jovian magnetic field and produce Alfvén waves (Neubauer, 1980). These waves carry energy back towards Jupiter, which is subsequently dissipated at various different wavelengths, again most notably in the UV and radio (Zarka, 2007). An interesting note is that the radio component of the Jupiter-Io sub-Alfvénic interaction was identified as early as the 1960s by Bigg (1964), who noted that bright radio emission originating from Jupiter was coincident with the quadratures of Io (where the maximum angular separation occurs between the two bodies from our perspective). More recently, moon-induced emission from Enceladus has also been identified on Saturn in the UV (Pryor et al., 2011).

In the context of the weakly/unmagnetised solar system planets like Venus and Mars, interactions with the solar wind are also important for their atmospheric evolution. It is likely that at earlier ages, the solar wind was much stronger

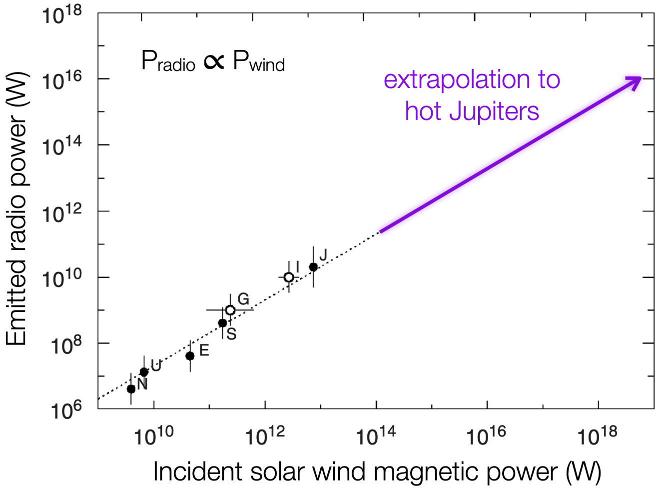

Figure 1.7: The empirically-derived radiometric Bode's law for the magnetised solar system planets, namely Earth (E), Jupiter (J), Saturn (S), Uranus (U), and Neptune (N). The power dissipated onto Jupiter from sub-Alfvénic interactions with its moons Io (I) and Ganymede (G) are also shown, which appears to follow the same trend. The power law relation between the incident solar wind and the emitted radio emission is linear, with an efficiency ratio of $\sim 2 \times 10^{-3}$. The extrapolation of this relation to the likely stellar wind environments of hot Jupiters is also shown. I will discuss this further in Section 1.5. Figure adapted from Zarka (2007).

compared to the present-day (Ó Fionnagáin & Vidotto, 2018). As a result, these two planets were likely to have been subjected to much harsher conditions. Due to the lack of intrinsic magnetic fields, the solar wind can remove a significant amount of material from their upper atmosphere (Kulikov et al., 2007; Curry et al., 2015). Combined with the harsher conditions at earlier ages, the removal of material from the atmospheres of Venus and Mars by the solar wind was likely to be even more significant.

1.3 The stellar wind environments around exoplanets

Wind outflows are not unique to the Sun. In fact, evidence for winds emanating from other stars came prior to Parker (1958) via spectroscopic features, from the likes of Beals (1929), Kosirev (1934), and Deutsch (1956), albeit for stars more massive/evolved than the Sun. Following from Parker's prescription for the solar wind, these signatures of outflowing material from other stars were re-interpreted as stellar winds, which are now evident across the HR diagram (Deutsch, 1969). Their existence also alleviated issues relating to how stars evolve towards the ends of their lives (e.g. Cameron, 1959; Parker, 1960).

An important thing to note is that all the stars identified to be undergoing mass-loss via stellar winds prior to the late 90s were massive/evolved stars (apart from the Sun). The winds of these stars are distinct from the solar wind, in that they are thought to be driven by momentum transfer from the stellar radiation field, via either absorption from dust grains or scattering from the opacity of ions (Lamers & Cassinelli, 1999). These are often referred to as *dust/continuum*-driven and *line/radiatively*-driven winds respectively. This bias towards their earlier detection is due to the fact that their mass-loss rates are many orders of magnitude greater than the solar wind, and therefore have denser and faster winds which can produce strong spectral signatures. These spectroscopic features that are powerful diagnostics tools for the winds of massive and evolved stars are known as P Cygni profiles (see Puls et al., 2008).

While it was the winds of massive/evolved stars that were initially discovered, these are not representative of the majority of stars in our galaxy. The primary stellar components of the galaxy are *low-mass* stars on the main-sequence, which are powered by burning hydrogen in their cores. These stars are of spectral types M, K, G, or F, and have masses ranging from around 0.1 to 1.5 solar masses ($M_{\odot}$), and effective temperatures from 2400 to 7200 K[1]. Within 10 parsecs of the solar system, low-mass stars comprise 93% of all stars, with M dwarfs being the most numerous at 75% (see RECONS, the REsearch Consortium On Nearby Stars).

Like the Sun, low-mass main-sequence stars exhibit hot coronae, as is evident from their prominent X-ray emission (Güdel, 2004; Johnstone & Güdel, 2015). They also possess surface magnetic fields, which are thought to be generated and sustained by convective dynamos (Christensen et al., 2009). The magnetic fields

---

[1] A Modern Mean Dwarf Stellar Color and Effective Temperature Sequence

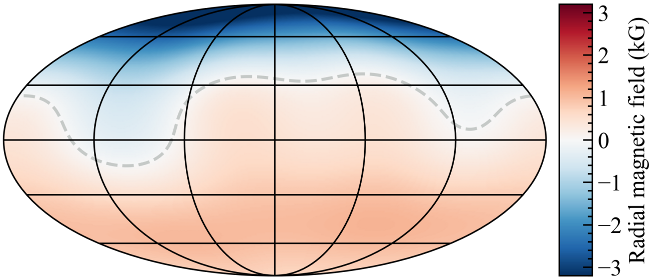

Figure 1.8: The radial surface magnetic field of the active M dwarf WX UMa. Maps such as this are reconstructed from spectropolarimetric observations, using the method known as Zeeman-Doppler imaging (ZDI, Semel, 1989). The field here is well-described by a dipole that is aligned with the rotation axis of the star, with a maximum strength of 3 kilogauss. Figure from Kavanagh et al. (2022) based on Morin et al. (2010).

of M dwarfs can be upwards of a kilogauss in strength (Morin et al., 2010), three orders of magnitude higher than the present-day Sun (see Figure 1.8). There is a strong relationship that holds over many orders of magnitude between the inferred surface magnetic fluxes of low-mass stars and their X-ray emission, implying that their coronae are magnetically heated (see Figure 1.9; Pevtsov et al., 2003; Vidotto et al., 2014). Coronal X-rays have been identified on stars as massive as A7V ($\sim 1.7\ M_\odot$, Schmitt et al., 1985; Peterson et al., 2006). Above this mass threshold, stars are thought to transition to having radiative outer envelopes, lacking convection and therefore the ability to sustain a dynamo-driven magnetic field. The evidence for hot, magnetically-active coronae on low-mass main-sequence stars naturally suggests that they are sources of solar-like *coronal* winds.

Low-mass main sequence stars are not only likely to have coronal winds, but they also are found to host the bulk of the 5000+ exoplanets discovered to date. As these stars can remain on the main-sequence for billions of years, understanding their stellar wind environments is crucial to determining the long-term effects of the wind outflows on the orbiting planets. M dwarfs are of particular interest in this context, as they are both the most numerous in the galaxy, and are expected to host the majority of Earth-like planets (see Gaidos et al., 2016; Burn et al., 2021). This is not currently reflected in exoplanet statistics however, as M dwarfs can exhibit high levels of activity which can hinder the detection of orbiting Earth-like planets through traditional methods (e.g. Lanza et al., 2011; Andersen & Korhonen, 2015). In Figure 1.10, I show the breakdown of the number of exoplanets found to orbit main-sequence stars as a function of their spectral type.

1.4 Measuring the winds of low-mass stars

The first evidence of winds originating from low-mass stars was presented by Wood et al. (1996). Based on density maps of the local interstellar medium (ISM),

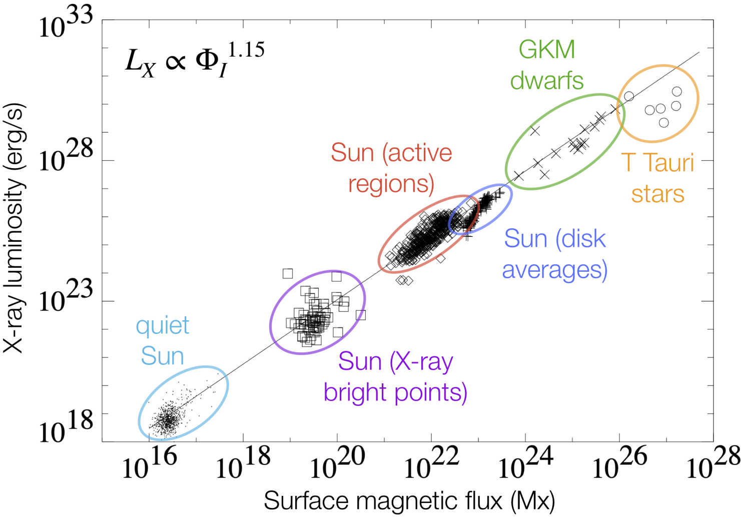

Figure 1.9: The observed relationship between the surface magnetic flux of low-mass stars and their X-ray emission. The data are from the Sun, main-sequence G, K, and M dwarfs, and pre-main-sequence T Tauri stars. A power-law fit to the data indicates that the X-ray luminosity L_{X} is proportional to the magnetic flux ${\Phi_I}^{1.15}$, implying that their X-ray emission is produced via magnetic heating in their coronae. Note that the magnetic flux values here are derived from the Zeeman broadening method, which are typically denoted with the subscript 'I', whereas those derived from maps obtained via the ZDI method (i.e. Figure 1.8) are denoted with the subscript 'V' (see Kochukhov, 2021). Figure adapted from Pevtsov et al. (2003).

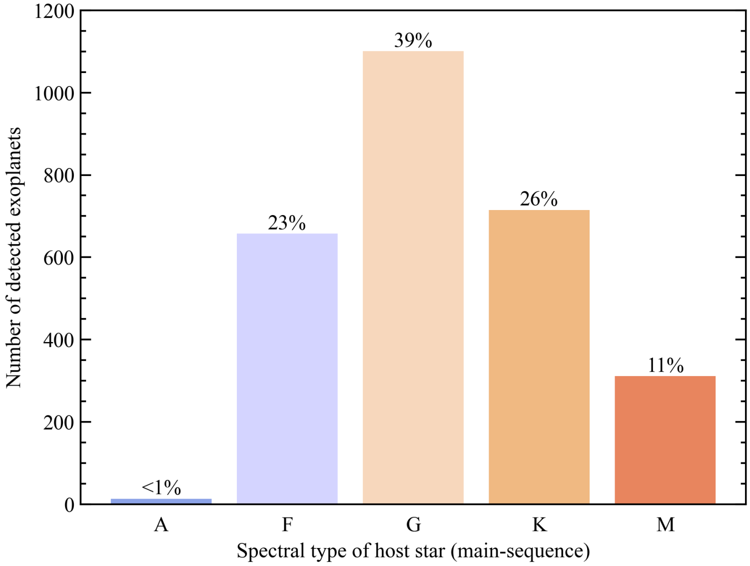

Figure 1.10: The number of exoplanets detected to orbit main-sequence stars as a function of the host star spectral type. The vast majority of exoplanet discovered to date are found to orbit main-sequence F–M stars, which are expected to exhibit coronal, solar-like stellar winds. The percentage of exoplanets detected orbiting main-sequence stars of each spectral type are shown above each bar. Data taken from the NASA Exoplanet Archive on June 14th 2022. Note that many of the host stars in the database used here do not have catalogued spectral types, so I have identified them using their effective temperatures and radii based on “A Modern Mean Dwarf Stellar Color and Effective Temperature Sequence”.

observations with the Hubble Space Telescope revealed that Lyman α emission from some stars was absorbed to a greater extent than what was expected from purely the ISM. At the same time, theoretical models had been proposed which predicted the existence of a 'wall' of hot neutral hydrogen at the heliopause (Pauls et al., 1995), the region where there is pressure balance between the ISM and solar wind outflow. This is effectively a scaled-up version of a planetary magnetopause. This wall of neutral hydrogen is thought to form due to the compression and heating of the ISM due to the motion of the heliosphere, the region inside the heliopause, through the ISM (Wood et al., 2021).

While the excess absorption of Lyman α emission from some stars could be attributed to a neutral hydrogen wall at the Sun's heliopause, Wood et al. (1996) found that it was still not sufficient to explain the Lyman α profiles from the stars ϵ Eri and λ And. Wood et al. (1996) therefore proposed that walls of neutral hydrogen could exist around these stars also at their astropauses, the stellar equivalent of a heliopause, formed in a similar manner as what was proposed for the Sun. The scenario suggested by Wood et al. (1996) is described in Figure 1.11. The implication that these stars had heliospheres of their own, called astrospheres, meant that they also had winds. This fit the narrative of these stars possessing coronae, which had been suggested based on X-ray observations of main-sequence stars up to spectral types of A7 (Schmitt et al., 1985). With a hot coronae, these stars could drive a thermally-expanding stellar wind outflow in the same manner as proposed by Parker (1958) for the Sun.

Since the initial proposal of Wood et al. (1996), around 30 main-sequence stars have been identified to exhibit Lyman α absorption profiles consistent with that expected from hydrogen walls at their astropauses (Wood et al., 2021). Using hydrodynamical models of stellar astrospheres, the Lyman α profiles of these stars have been fit to determine their mass-loss rates. To date, this has been the most successful method for measuring the winds of low-mass stars (Vidotto, 2021). More recently however, other methods have also been used successfully to estimate stellar wind mass-loss rates, namely based on the presence of prominences around the star (Jardine & Collier Cameron, 2019), and the evaporation of exoplanetary atmospheres (Vidotto & Bourrier, 2017). Additionally, non-detections of thermal radio emission from the winds of low-mass main-sequence stars can provide useful upper-limits for their mass-loss rates (e.g. Fichtinger et al., 2017).

In Figure 1.12, I show the inferred mass-loss rate per unit surface area for low-mass main-sequence stars as a function of their surface X-ray fluxes. A power-law fit to the data indicates a relationship between the two quantities, implying that the energy source powering their X-ray emission also drives the wind outflows from the coronae of these stars. This power law can be used to link the mass-loss rates of low-mass main-sequence stars to their magnetic field strengths. Figure 1.9 shows the relation between the X-ray luminosity and surface magnetic fluxes derived using the Zeeman broadening method (Φ_I). However, a large fraction of the stars shown in Figure 1.12 have reconstructed surface magnetic field maps available, such as that shown in Figure 1.8 (see Morin et al., 2008a; Vidotto et al., 2014, 2016; Folsom et al., 2018; See et al., 2019; Klein et al., 2021a). These maps are also one of the main constraints for state-of-the-art models of stellar wind environments

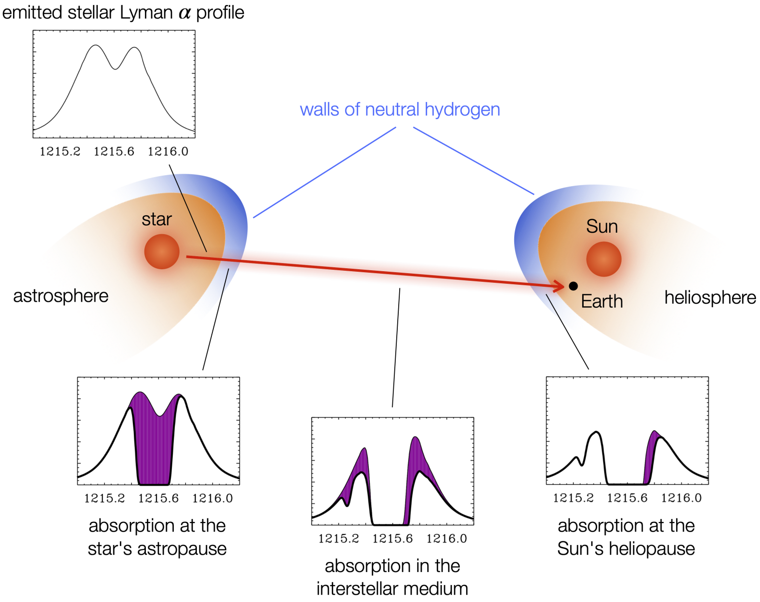

Figure 1.11: Sketch of the formation of the Lyman α absorption profile at 1216 Å initially proposed by Wood et al. (1996). The line profile initially emitted from the star is shown in the top left. Due to the motion of the heliosphere through the interstellar medium, the region where the solar wind plasma dominates, a wall of neutral hydrogen builds up at the heliopause (the edge of the heliosphere). If the star also is a source of a stellar wind, the same process occurs. The wall of neutral hydrogen at the stellar astropause is the first source of absorption of the stellar Lyman α emission as it leaves the system. This is shown in the bottom left panel. The interstellar medium is the next source of absorption (bottom middle panel). Finally, the hydrogen wall at the Sun's heliopause absorbs in the 'red wing' of the line profile (bottom right panel). Depending on the wind mass-loss rate of the star in question, the appearance of the Lyman α at Earth will change. By fitting different models to observed Lyman α, the mass-loss rate of the star can therefore be inferred. Figure adapted from Wood (2004).

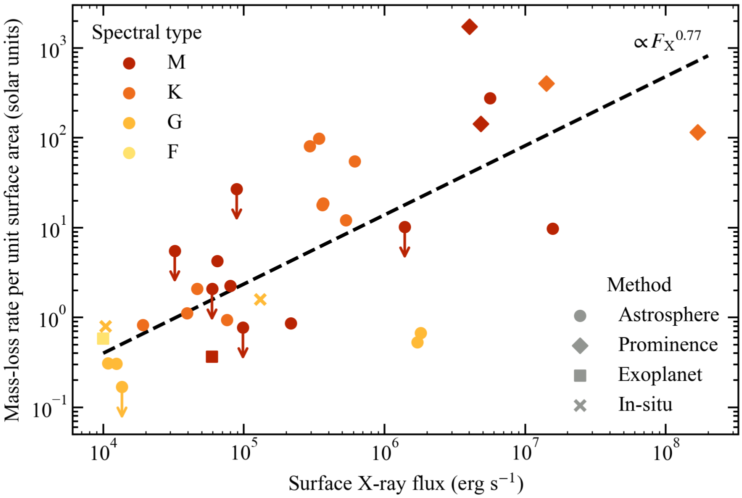

Figure 1.12: Mass-loss rate measurements of all main-sequence low-mass stars obtained to date as a function of their surface X-ray fluxes F_{X}. The mass-loss rate values ($\dot{M}$) are normalised to the stellar surface area $4\pi {R_\star}^2$, where $R_\star$ is the stellar radius. Each point is coloured by its spectral type, and the symbols illustrate the method used to determine the mass-loss rate. Downward-pointing arrows illustrate where the values are upper-limits. The majority of these are obtained via the fitting of the Lyman α absorption profile of the star as described in the text, which are listed in Wood et al. (2021). The estimates from prominence formation are from Jardine & Collier Cameron (2019), and those from exoplanets are from Kislyakova et al. (2014) and Vidotto & Bourrier (2017). I also show the in-situ measurements of the solar wind. The Sun's X-ray luminosity varies by about an order of magnitude between activity minimum and maximum (Judge et al., 2003), and the mass-loss rate varies from 0.8 to 1.6 times the average value of 1.261×10^{12} g s^{-1} (Finley et al., 2019). The power-law fit to the data from Wood et al. (2021) is shown to illustrate the overall increase in stellar wind mass-loss rate with surface X-ray flux.

for low-mass stars (Chapters 2, 4, and 5). Therefore, below I opt to use the readily-available Φ_V values as opposed to Φ_I. Note that Φ_V values underestimate stellar surface magnetic fluxes compared to those obtained with the Zeeman broadening method, as the ZDI method cannot capture the small-scale magnetic field structure of stars (Reiners & Basri, 2009). However, the two values are generally correlated with one another (See et al., 2019).

The relation between the mass-loss rate per unit surface area of low-mass stars and surface X-ray fluxes derived empirically by Wood et al. (2021) is:

$$\dot{M}/{R_\star}^2 \propto {F_{\mathrm{X}}}^{0.77} \propto {L_{\mathrm{X}}}^{0.77}{R_\star}^{-1.54}. \tag{1.1}$$

Similar to the Zeeman broadening case shown in Figure 1.9, Vidotto et al. (2014) derived the following relation between the X-ray luminosity and the surface magnetic fluxes Φ_V obtained using the ZDI method for GKM dwarfs:

$$L_{\mathrm{X}} \propto {\Phi_V}^{1.80}. \tag{1.2}$$

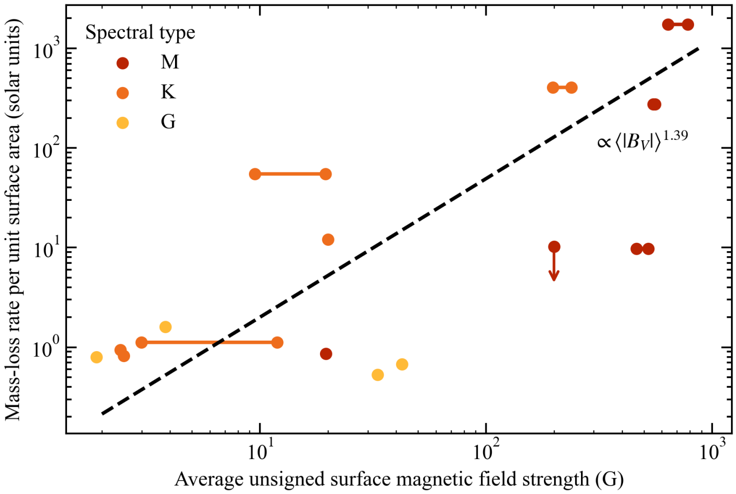

Figure 1.13: Same as Figure 1.12, but for the mass-loss rate per unit surface area as a function of the star's observationally-derived unsigned average surface magnetic field strength $\langle |B_V| \rangle$. For stars with multiple magnetic field maps available, their min/max values of $\langle |B_V| \rangle$ are joined with horizontal lines. The power law derived in Equation 1.3 is overlaid as a dashed line, neglecting the dependence on the stellar radius.

The surface magnetic flux relates to the average unsigned magnetic field strength of the star $\langle |B_V| \rangle$ via $\Phi_V = 4\pi {R_\star}^2 \langle |B_V| \rangle$, giving

$$L_\mathrm{X} \propto \langle |B_V| \rangle^{1.80} {R_\star}^{3.60}.$$

Combining this with Equation 1.1 then gives

$$\dot{M}/{R_\star}^2 \propto \langle |B_V| \rangle^{1.39} {R_\star}^{1.23}. \tag{1.3}$$

In Figure 1.13, I compare this relation to the observationally-derived values for $\dot{M}/{R_\star}^2$ and $\langle |B_V| \rangle$. These are in good agreement with one another, implying that for low-mass main-sequence stars, stronger magnetic fields drive denser and faster stellar wind outflows. This is neglecting the weaker dependence on the stellar radius in Equation 1.3, which varies from around $0.1 - 1$ solar radii for these stars. The values of $\langle |B_V| \rangle$ however span almost three orders of magnitude.

1.5 Star-planet interactions

It was not long after the discovery of the first exoplanet orbiting a main-sequence star in 1995 by Mayor & Queloz (1995) that astronomers began to speculate about interactions occurring between stars and planets. The inspiration for many of these came directly from the theoretical interpretation of observations from RS CVn-type systems. These systems are typically comprised of a main-sequence/subgiant star,

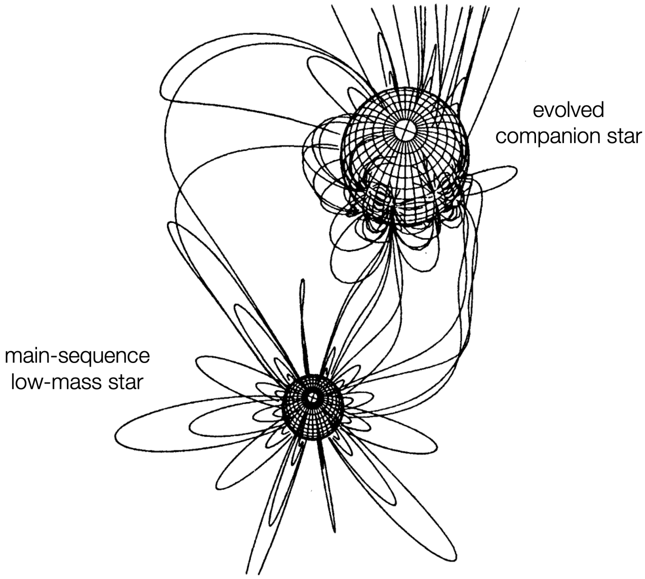

Figure 1.14: Sketch of the magnetic interactions thought to occur in RS CVn binary systems. Reconnection between the magnetic field of the low-mass main-sequence star and the evolved companion star is thought to produce flaring in the system. Although not explicitly shown, tidal interactions between the two bodies are also expected to spin up the main-sequence star, which in turn increases its magnetic activity. In the context of exoplanetary systems, RS CVn systems serve as an analogy for the interactions which may occur between the star and planet. Figure adapted from Uchida & Sakurai (1983).

orbited by a cool, evolved G/K-type companion star (Hall, 1976). The primary star in these systems is thought to be spun-up by the evolved companion star via tidal interactions, enhancing the dynamo of the primary and therefore increasing its activity-related emission compared to if the star was isolated (Drake et al., 1989; Rubenstein & Schaefer, 2000). In addition to this, magnetic interactions between the two stars are also thought to enhance flaring activity, driven by magnetic reconnection. An illustrative sketch is shown in Figure 1.14.

The early population of discovered exoplanets was comprised of Jupiter-sized planets orbiting very close to their stars[2], commonly referred to as 'hot Jupiters'. Soon after their discovery, parallels were made between these hot Jupiter systems and RS CVn binaries. Through similar tidal interactions as in the case of RS CVn systems, hot Jupiters were identified as being sufficient in mass and distance to the star to act as a potential activity enhancer, inducing a tidal bulge on the stellar surface (Cuntz et al., 2000; Saar & Cuntz, 2001). These are often referred to as *tidal* star-planet interactions.

Alongside tidal star-planet interactions, *magnetic* star-planet interactions were also proposed for hot Jupiter systems following from our understanding of RS CVns

---

[2] NASA Exoplanet Archive

(Rubenstein & Schaefer, 2000; Cuntz et al., 2000; Ip et al., 2004). If like Jupiter these planets have magnetospheres of their own (e.g. Shkolnik et al., 2005; Vidotto et al., 2010; Kislyakova et al., 2014; Cauley et al., 2019), a similar reconnection-driven mechanism could occur between the stellar and planetary magnetic fields, producing enhanced emission on the star. Such a mechanism has been well-studied on Jupiter itself, which interacts *sub-Alfvénically* with its moons Io, Europa, and Ganymede (Neubauer, 1980; Hess et al., 2008; Saur et al., 2013). These interactions produce Alfvén waves, which carry energy back towards Jupiter along the magnetic field line connecting the two bodies, producing prominent emission in the radio via the electron cyclotron maser instability and UV (see Section 1.2; right panel of Figure 1.6; Zarka, 2007; Louis et al., 2017). The criteria for sub-Alfvénic interactions is that the relative velocity between the stellar wind and the planet Δu is less than the Alfvén velocity u_A, which depends on the plasma density ρ and magnetic field strength B at the planet's position. This is often written as a ratio, which is known as the Alfvénic Mach number:

$$M_\mathrm{A} = \frac{\Delta u}{u_\mathrm{A}} = \frac{\Delta u}{B/\sqrt{4\pi\rho}} < 1. \tag{1.4}$$

In the reference frame of the planet, the point where $\Delta u = u_\mathrm{A}$ is known as the Alfvén surface, which encloses the region where $M_\mathrm{A} < 1$.

Analogous of the interactions between Jupiter and its moons, sub-Alfvénic interactions have been proposed for exoplanetary systems, with the star and planet taking the roles of Jupiter and the moon respectively (Saur et al., 2013; Turnpenney et al., 2018; Cauley et al., 2019). The criteria for these interactions to occur is that the planet orbits inside the Alfvén surface of the wind of the host star, the magnetic equivalent of the sonic surface. Inside this region, the speed of Alfvén waves exceeds that of the outflowing wind, and the waves can therefore travel back towards the star. The energy they carry is expected to subsequently dissipate near the surface, producing emission at radio (Turnpenney et al., 2018; Kavanagh et al., 2021, 2022), infrared, optical, UV (Shkolnik et al., 2003, 2008; Klein et al., 2022), and X-ray wavelengths (Lanza, 2009; Pillitteri et al., 2011). A sketch outlining this process is shown in Figure 1.15. In late 2021, the first tentative detection of such interactions at radio wavelengths were reported for a sample of main-sequence M dwarfs at radio wavelengths by Callingham et al. (2021).

Another type of interaction thought to occur in exoplanetary systems are those between planets and the winds of their host stars. I will refer to these as *wind-planet* interactions. Signatures of these types of interactions again are predicted to occur across a wide range of wavelengths, and also cover a broad range of different mechanisms. One type of wind-planet interaction is linked to the irradiation of the planet via the star. Close-in exoplanets have been observed to transit their host stars with a much larger effective radius in Lyman α than in the optical (e.g. Lecavelier des Etangs et al., 2012). The theoretical interpretation for this is that the strong stellar X-ray/UV radiation incident on the upper atmosphere of the exoplanet causes it to escape, effectively inflating the planet. This material can readily absorb Lyman α emission, and therefore blocks a much greater fraction of the stellar radiation than in the optical. However, if the wind of the host

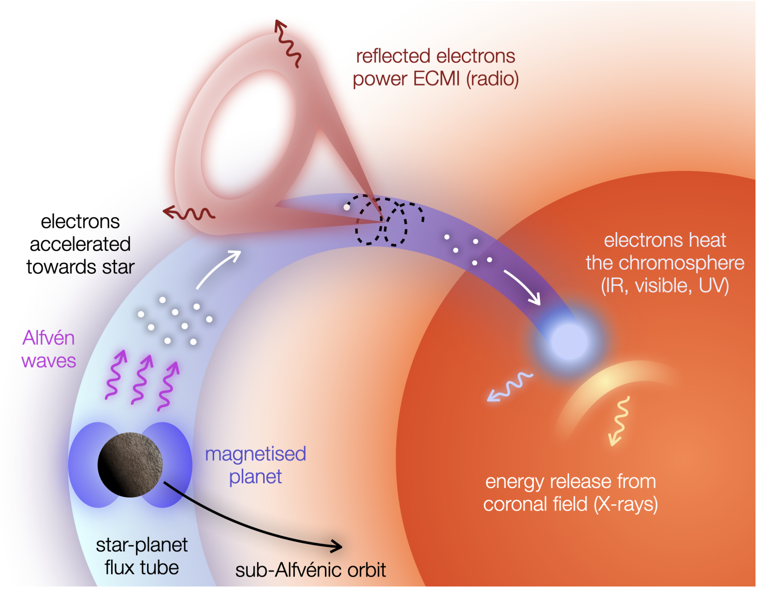

Figure 1.15: Sketch illustrating the different types of radiation associated with magnetic star-planet interactions. Interactions between the planetary and stellar magnetic field produce Alfvén waves, which travel back towards the star. These waves can interact with electrons, accelerating them. Such a process has been identified to power emission via the electron cyclotron maser instability, which produces circularly polarised radio emission. The Alfvén waves can also directly deposit energy at the surface of the star, heating the chromosphere. Signatures of this are thought to occur at infrared, visible, and UV wavelengths. Additional energy may also be released via X-ray emission from the small-scale coronal magnetic field, as suggested by Lanza (2009). Figure from Kavanagh et al. (in prep.).

star is also strong, it may hinder or ‘confine’ the escape of the irradiated upper planetary atmosphere (Vidotto & Cleary, 2020), therefore altering the Lyman α transit compared to if there was no stellar wind present (Carolan et al., 2021). In theory, by observing Lyman α transits of exoplanets, the mass-loss rates of the host star’s wind can be inferred (Vidotto & Bourrier, 2017).

Additional types of wind-planet interactions can also occur if the planet has an intrinsic magnetic field. For instance, if the stellar wind outflow is super-Alfvénic in the reference frame of the planet, a bow shock will form around the planet (Bagenal, 2013). The build-up of material at the nose of the bow shock is thought to form potentially observable signatures in the UV as the planet transits its host star (Vidotto et al., 2010; Llama et al., 2011).

Over the last 30 years, the most searched for signatures of wind-planet interactions are exoplanetary aurorae. In the solar system, the solar wind interaction with the magnetised planets produces bright aurorae that are particularly prominent at radio and UV wavelengths (as discussed in Section 1.2). Zarka (1998) was the first to suggest that the same process could occur on exoplanets providing they are magnetised, which could in theory be used as an alternative way to find new exoplanets and measure their magnetic field strengths.

The main driver in the search for auroral radio emission from exoplanets is firstly that at low frequencies, Jupiter’s auroral emission outshines the Sun by roughly 3 orders of magnitude (Zarka, 2007). If the same scenario holds for exoplanets, there should be no issues with regards to the contrast of their emission relative to their host star, as opposed to at other wavelengths (e.g. UV). The second motivating factor comes from the aforementioned radiometric Bode’s law (Figure 1.7). As hot Jupiters lie much closer to their host stars than any planet to the Sun, they are expected to experience much stronger stellar winds (Vidotto et al., 2015; Kavanagh et al., 2019). Assuming that the radiometric Bode’s law holds for higher incident wind powers, it tells us that the closer a planet gets to its host star, the higher the radio power of its aurora will be. This is also true for planets with larger magnetospheres, which in turn relates to the planet’s magnetic field strength, as they intercept a higher magnetic flux from the wind outflow. With the combination of their close-in nature and their potentially strong magnetic fields (Cauley et al., 2019), hot Jupiters could exhibit intense aurorae at radio wavelengths. While searches have taken place over the last 30 years, the first tentative detection of such emission was only recently presented by Turner et al. (2021), who reported potential auroral-like radio emission originating from the hot Jupiter τ Boo b. The reason for the lack of detections is a main topic of Chapters 2 & 3.

1.6 Thesis outline

Chapter 2: Tuning in to the radio environment of HD189733b

In this chapter of the thesis, I explore scenarios for wind-planet interactions occurring on the well-known hot Jupiter HD189733b. This planet orbits very close to its magnetically-active host star at a distance of 0.03 au (3% of the distance between the Earth and Sun), and is therefore a strong candidate for auroral radio emission following from Sections 1.2 and 1.5. To investigate this, I perform 3D MHD simulations of the wind of the host star, using the BATS-R-US MHD solver (Powell et al., 1999; Tóth et al., 2012). These models are constrained by the observationally-derived surface magnetic field maps of the star during 3 epochs from Fares et al. (2017), providing snapshots of the stellar wind environment around HD189733b. A polytropic index γ is used to mimic the magnetic heating of the corona, wherein the thermal pressure p relates to the density ρ as $p \propto \rho^{\gamma}$.

One of the key findings of this work is that while auroral radio emission could be generated on HD189733b within the detection limits of current-generation radio telescopes such as LOFAR, it may be absorbed significantly by the wind of the star through thermal processes. I refer to these regions as the 'radio photosphere' of the stellar wind, and show that the detection of planetary radio emission is most favourable when the planet is near primary transit, which is very useful for guiding future radio observations. The contents of this chapter were published in the Monthly Notices of the Royal Astronomical Society (MNRAS), 2019, 485, 4529 (Kavanagh et al., 2019).

Chapter 3: Radio eclipses of exoplanets by the winds of their host stars

Following from the results presented in Chapter 2, in this chapter I investigate the effects of different stellar wind properties on the duration where the planet orbits inside the radio photosphere. The morphology of this phenomenon resembles that of an eclipse, and so I refer to it as a 'radio eclipses'. Using a code developed to solve for the wind solution obtained by Parker (1958), I perform a parametric study where I vary the stellar wind temperature and mass-loss rate, as well as the orbital distance and inclination, determining how each affects the duration of the radio eclipses. I show that observing such an eclipse in the radio can be used to infer the properties of the stellar wind, which so far has been limited to a handful of cases (e.g. Figure 1.12). This work was published in MNRAS, 2020, 493, 1492 (Kavanagh & Vidotto, 2020).

Chapter 4: Planet-induced radio emission from the coronae of M dwarfs

The topic of the next chapter shifts towards magnetic star-planet interactions on low-mass stars. The inspiration for this work comes from the recent detections of radio emission from a sample of M dwarfs, some of which are indicative of these types of interactions (i.e. Vedantham et al., 2020; Pérez-Torres et al., 2021; Callingham et al., 2021). In this work, I explore the scenario for magnetic star-planet interactions occurring on the nearby M dwarfs Proxima Centauri (Prox Cen) and AU Microscopii (AU Mic). Both of these stars are host to close-in planets, and have recently had their surface magnetic fields reconstructed by Klein et al. (2021a) and Klein et al. (2021b) respectively. In a similar manner to Chapter 2 I use these maps as constraints for 3D MHD models of the winds of the stars. Note that in this work, I utilised an Alfvén-driven wind model (AWSoM van der Holst et al., 2014), which heats the corona through the dissipation of Alfvén waves, as opposed to via as polytropic index as used in Chapter 2. The estimated mass-loss rate for Prox Cen of $\dot{M} < 4 \times 10^{-13}\ M_{\odot}\ \mathrm{yr}^{-1}$ (Wood et al., 2001) provides an additional constraint in this work.

The main condition that determines if magnetic star-planet interactions can occur is if the planet orbits inside the Alfvén surface of the stellar wind (Equation 1.4). Using the model for the stellar wind, I show that Prox Cen b orbits outside this region for its entire orbit. Therefore, it is not expected that such interactions could occur, which is at odds with the tentative detections of such interactions suggested by Pérez-Torres et al. (2021). For AU Mic on the other hand, its mass-loss rate is relatively unconstrained. I show that in the case where it has a low mass-loss rate, both planets b and c orbit inside the Alfvén surface for most of the time. This finding shows that a detection or non-detection of magnetic star-planet interactions can be used to estimate the mass-loss rate of low-mass stars, complementing the results of Chapter 3. The results of this work were published in MNRAS, 2021, 501, 1511 (Kavanagh et al., 2021).

Chapter 5: Radio masers on the active M dwarf WX UMa

The final chapter of the thesis focusses on the active M dwarf WX UMa from the sample published by Callingham et al. (2021), which is one of two stars in the sample with available surface magnetic field maps (the other being AD Leo, Morin et al., 2008b; Lavail et al., 2018). In the case of WX UMa, Callingham et al. (2021) suggested that its observed radio emission is likely to be attributed to cyclotron emission, which is expected from magnetic star-planet interactions (Section 1.5). The interesting aspect about WX UMa is that there has yet to be a planet detected to orbit it, which may be due to the fact that the star is very active (Morin et al., 2010). To explore this scenario, I utilise a magnetic field map of the star obtained by Morin et al. (2010) as a constraint for the stellar wind using the AWSoM model. The mass-loss rate for the star is not known, so I estimate it based on its surface X-ray flux via Equation 1.1, giving around the solar value of $2 \times 10^{-14}\ M_{\odot}\ \mathrm{yr}^{-1}$.

I then approach the question in the opposite way to the case of Prox Cen and AU Mic in Chapter 4, which have well-established planetary orbits and properties, which is: where can a planet be placed around WX UMa such that the emission it induces reproduces the observations? To answer this question, I develop a model which accounts for the stellar magnetic field line that connects to the planet at any given time, which determines if the emission can be seen by an observer. By exploring a parameter space for the orbit and properties of the hypothetical planet, and using a prescription for the power of the emission from Saur et al. (2013), I show that a Neptune-sized exoplanet orbiting the star around every 5 days at a distance of 0.034 au can reproduce the observed radio emission from the star. I also derive magnetic field strengths for the planet of $10 - 100$ G. The model developed in this work has fantastic applications to future radio observations for identifying planet candidates around active stars.

In this work, I also explore a scenario for generating circularly polarised emission on WX UMa without needing the presence of a planet. This is inspired by the phenomenon on Jupiter, where its auroral emission is in part attributed to the so-called 'breakdown of co-rotation' (Cowley & Bunce, 2001), as well as that expected from massive magnetised stars (Linsky et al., 1992; Trigilio et al., 2004; Owocki et al., 2022). This type of emission could also reproduce the observations relatively well, albeit with a different modulation than that induced by an orbiting planet. Therefore, models such as this should be explored in future in conjunction with planet-induced models when interpreting potential planet-induced signals.

1.7 Outlook

In this thesis, I have explored scenarios for wind-planet and magnetic star-planet interactions, utilising state-of-the-art stellar wind simulations, which are constrained by information derived directly from a variety of observations. These models provide snapshots of the wind environments of stars, which provide a wealth of information about the plasma surrounding the planet, which is not generally obtainable via other means. The plasma environment tells us if and when interactions between the star and planet can occur, and if so, their strength and modulation. Thanks to the ever-increasing sensitivity of current-generation telescopes such as LOFAR, low-mass stars are beginning to light up the sky at radio wavelengths, many of which are indicative of star-planet interactions. Therefore, there is a mounting need for sophisticated models to predict and interpret these signals, such as those presented in this thesis.

Looking forward, my aspirations for the work presented here are for it to be used to guide and interpret upcoming radio observations. Combining predictions for planets around stars with traditional methods such as the radial velocity and transit method will hopefully lead to the first confirmed detection of an exoplanet in the radio regime. The model developed in the final chapter also has great potential to be applied not only to other stars, but to magnetised exoplanets and brown dwarfs, which are also expected to exhibit similar emission.

In terms of specific systems, Prox Cen has recently become a target of renewed interest in the context of magnetic star-planet interactions, as a new planet has been found to orbit it (Faria et al., 2022). Unlike planet b, which is likely to orbit entirely outside the Alfvén surface (Chapter 4), this newly-discovered planet d orbits sub-Alfvénically for over 50% of its orbit, wherein it could produce observable signatures on the star via magnetic star-planet interactions (Kavanagh et al., in prep.). The utilisation of the model developed in the final chapter of this thesis can be used to predict the morphology of both the radio signal, as well as in the UV, as has been done in the case of AU Mic (Kavanagh et al., 2021; Klein et al., 2022). By planning future observations of the system guided by the model, Prox Cen could serve as a fantastic test bed for benchmarking these models of magnetic star-planet interactions.

Other targets detected in the LoTSS survey are also worth exploring with the model developed in Chapter 5. One example is the inactive star GJ1151 in the sample from Callingham et al. (2021). Due to its inactivity and slow rotation, it is unlikely that its radio emission could be attributed to an alternative emission mechanism such as those explored for WX UMa. In addition, recent radial velocity searches hint at the presence of a planet around the star (Mahadevan et al., 2021), in agreement with the suggestions of Vedantham et al. (2020). The current missing piece of this puzzle however is the lack of a surface magnetic field map. With this, the radio emission from the star could be interpreted in the same was as for WX UMa, utilising a stellar wind model for the star.

2 | Tuning in to the radio environment of HD189733b

2.1 Abstract

We present stellar wind modelling of the hot Jupiter host HD189733, and predict radio emission from the stellar wind and the planet, the latter arising from the interaction of the stellar wind with the planetary magnetosphere. Our stellar wind models incorporate surface stellar magnetic field maps at the epochs Jun/Jul 2013, Sep 2014, and Jul 2015 as boundary conditions. We find that the mass-loss rate, angular momentum-loss rate, and open magnetic flux of HD189733 vary by 9%, 40%, and 19% over these three epochs. Solving the equations of radiative transfer, we find that from 10 MHz–100 GHz the stellar wind emits fluxes in the range of 10^{-3}–5 μJy, and becomes optically thin above 10 GHz. Our planetary radio emission model uses the radiometric Bode's law, and neglects the presence of a planetary atmosphere. For assumed planetary magnetic fields of 1–10 G, we estimate that the planet emits at frequencies of 2–25 MHz, with peak flux densities of $\sim 10^2$ mJy. We find that the planet orbits through regions of the stellar wind that are optically thick to the emitted frequency from the planet. As a result, unattenuated planetary radio emission can only propagate out of the system and reach the observer for 67% of the orbit for a 10 G planetary field, corresponding to when the planet is approaching and leaving primary transit. We also find that the plasma frequency of the stellar wind is too high to allow propagation of the planetary radio emission below 21 MHz. This means a planetary field of at least 8 G is required to produce detectable radio emission.

2.2 Introduction

Low-mass stars ($0.1 - 1.3\ M_{\odot}$) lose mass throughout their entire lives in the form of quiescent stellar winds. These stars also exhibit magnetic activity at their surfaces, and are observed to undergo variations in magnetic field strength (e.g. Fares et al., 2017) and polarity reversals over time (e.g. Donati et al., 2008a; Boro Saikia et al., 2016). The Zeeman Doppler imaging (ZDI) technique, used to reconstruct large-scale surface stellar magnetic fields (Donati et al., 1997), has revealed that magnetically active stars exhibit complex magnetic topologies that can vary as rapidly as a few rotation periods (Boro Saikia et al., 2015), over one magnetic cycle (Fares et al., 2009; Boro Saikia et al., 2016), and over evolutionary timescales (Petit et al., 2008; Vidotto et al., 2014). These variations in field strength, both over time and across the stellar surface, drive stellar wind outflows that vary in strength over different timescales (Nicholson et al., 2016).

As the stellar wind propagates out into the interplanetary environment, the variations of its properties are most strongly felt by close-in exoplanets (orbital distances $a < 0.5$ au). These exoplanets form a large proportion of the detected planets orbiting low-mass stars. At such close proximity, these planets are likely to be subjected to much harsher wind conditions from the host star than those experienced by the solar system planets (Vidotto et al., 2015). For example, close-in hot Jupiters have been observed to exhibit extended atmospheres, which is shaped by the interaction of the stellar wind with the planetary atmosphere (Lecavelier des Etangs et al., 2012; Bourrier & Lecavelier des Etangs, 2013; Bourrier et al., 2016). The presence of close-in planets may also enhance the magnetic activity of the host star, both through tidal and magnetic interactions (Cuntz et al., 2000; Ip et al., 2004; Shkolnik et al., 2008).

Stellar winds are believed to power exoplanetary radio emission, similarly to what occurs in the solar system for Earth, Jupiter, Saturn, Uranus, and Neptune. This radio emission occurs via the Cyclotron Maser instability (see Treumann, 2006), wherein energetic electrons spiral through planetary magnetic field lines towards polar regions of strong magnetic field. This emission process has also been observed for low-mass stars (Bingham et al., 2001; Llama et al., 2018). The process for planets is powered by the dissipation of the magnetic flux of the stellar wind on the magnetosphere of the planet. As close-in exoplanets are likely to be subjected to more energetic winds, it is expected that radio emission occurs for these planets at higher powers (Zarka et al., 2001). If detectable, this would serve as a new direct detection method for exoplanets, show that exoplanets are magnetised, and also act as a method to probe the stellar wind of the host star. So far, there has yet to be a conclusive detection of exoplanetary radio emission, despite numerous efforts (Smith et al., 2009; Lazio et al., 2010b; Lecavelier des Etangs et al., 2013; Sirothia et al., 2014; O'Gorman et al., 2018).

However, the detection of planetary radio emission could be inhibited due to dense stellar winds, which can absorb emission at radio wavelengths (Vidotto & Donati, 2017). The winds of low-mass stars are known to be sources of radio emission, arising through thermal free-free processes (Panagia & Felli, 1975; Wright & Barlow, 1975; Güdel, 2002; Ó Fionnagáin et al., 2019a), which depend on both the density and temperature of the wind. By the same process, the wind can self-absorb the generated free-free radio emission if the optical depth is high enough. As a result, if a planet emitting its own radio emission orbits through regions of the wind that are optically thick to the planetary frequency, the planetary emission will also be absorbed.

In this paper, we investigate the radio environment of HD189733b, which orbits the main-sequence K2V star HD189733. As part of the MOVES (Multiwavelength Observations of an eVaporating Exoplanet and its Star, PI: V. Bourrier) collaboration, we model the wind of the star using surface magnetic field maps presented in

Table 2.1: Planetary and stellar parameters of HD189733b and its host star.

Parameter	Value
Star:	
Stellar mass $(M_\star)^1$	0.78 $M_\odot$
Stellar radius $(R_\star)^1$	0.76 $R_\odot$
Rotational period $(P_{\rm rot})^2$	11.94 days
Distance $(d)^3$	19.8 pc
Planet:	
Planetary mass $(M_{\rm p})^4$	1.13 $M_{\rm Jup}$
Planetary radius $(R_{\rm p})^4$	1.13 $R_{\rm Jup}$
Orbital distance $(a)^1$	8.8 $R_\star$
Orbital period $(P_{\rm orb})^1$	2.2 days

1: Llama et al. (2013); 2: Fares et al. (2010); 3: Gaia Collaboration et al. (2018); 4: Stassun et al. (2017)

Fares et al. (2017), and calculate the radio emission from the stellar wind and planetary magnetosphere. Due to the close proximity of the planet to its host star, the system has been the subject of many star-planet interaction studies (Fares et al., 2010; Cauley et al., 2018). The host star is also very active. Its magnetic field has been observed to vary in unsigned average field strength from 18 to 42 G over a 9 year period (Fares et al., 2017). This short-term variation ($\sim$ 1 year), in combination with the small orbital distance of the planet and strong stellar magnetic field, is likely to power time-varying radio emission from the planet that could be orders of magnitudes larger than those from planets in the solar system. The variations of the stellar wind properties at the planetary orbit could also lead to variations in the UV transit lightcurve over time (Lecavelier des Etangs et al., 2012; Bourrier & Lecavelier des Etangs, 2013; Llama et al., 2013).

The layout of this paper is as follows: in Section 2.3, we present our modelling and radio emission calculation of the wind of HD189733. Then, in Section 2.4 we calculate the planetary radio emission. We investigate different scenarios where the planetary radio emission may be unable to propagate out of the planetary system in Section 2.5. We discuss our findings in Section 2.6, and then present a summary and conclusions in Section 2.7.

2.3 Stellar wind of HD189733

2.3.1 Modelling the stellar wind

To model the wind of HD189733, we use the 3D magnetohydrodynamical (MHD) code BATS-R-US (Powell et al., 1999; Tóth et al., 2012), modified by Vidotto et al. (2012). BATS-R-US has been used to model stellar wind outflows in the context of low-mass and planet-hosting stars (e.g. Vidotto et al., 2012; Llama et al., 2013; Cohen et al., 2014; Alvarado-Gómez et al., 2016; Ó Fionnagáin et al., 2019a).

BATS-R-US solves the ideal set of MHD equations, for conservation of mass, magnetic flux, momentum, and energy respectively:

$$\frac{\partial}{\partial t}\rho + \nabla \cdot (\rho \boldsymbol{u}) = 0, \tag{2.1}$$

$$\frac{\partial}{\partial t}\boldsymbol{B} + \nabla \cdot (\boldsymbol{uB} - \boldsymbol{Bu}) = 0, \tag{2.2}$$

$$\frac{\partial}{\partial t}(\rho \boldsymbol{u}) + \nabla \cdot \left[\rho \boldsymbol{uu} + \left(p + \frac{B^2}{8\pi}\right)\boldsymbol{I} - \frac{\boldsymbol{BB}}{4\pi}\right] = \rho \boldsymbol{g}, \tag{2.3}$$

$$\frac{\partial}{\partial t}\varepsilon + \nabla \cdot \left[\left(\varepsilon + p + \frac{B^2}{8\pi}\right)\boldsymbol{u} - \frac{(\boldsymbol{u} \cdot \boldsymbol{B})\boldsymbol{B}}{4\pi}\right] = \rho \boldsymbol{g} \cdot \boldsymbol{u}. \tag{2.4}$$

These equations are solved for a plasma with a mass density ρ, velocity $\boldsymbol{u} = \{u_x, u_y, u_z\}$, magnetic field $\boldsymbol{B} = \{B_x, B_y, B_z\}$, and thermal pressure p. Here, $\boldsymbol{I}$ is the identity matrix, and ε is the total energy density:

$$\varepsilon = \frac{\rho u^2}{2} + \frac{p}{\gamma - 1} + \frac{B^2}{8\pi}, \tag{2.5}$$

where γ is the polytropic index.

The inputs of BATS-R-US are the stellar mass $M_\star$ and radius $R_\star$, which provide the surface gravity $\boldsymbol{g}$, coronal base temperature T_0 and number density n_0, rotational period $P_{\rm rot}$, and surface magnetic field map. In our wind simulations, we make the following assumptions:

1. The wind is an ideal gas: $p = nk_{\rm B}T$, where $n = \rho/(\mu m_{\rm p})$ is the number density, $k_{\rm B}$ is Boltzmann's constant, and T is the temperature. Here, $\mu m_{\rm p}$ is the mean mass per particle.

2. The wind is composed of fully ionised hydrogen, so we adopt a value of $\mu = 0.5$.

3. The wind is polytropic: $p \propto \rho^\gamma$.

Provided that we have derived values for the stellar mass, radius, and rotational period, we are left with the following free parameters in our models: T_0, n_0, and γ. For the coronal base temperature T_0, we adopt a value of 2×10^6 K, which is typical for the coronae of K stars (Johnstone & Güdel, 2015). For the base number density n_0, we assume 10^{10} cm^{-3}. We take $\gamma = 1.1$ for the polytropic index, which is similar to the effective adiabatic index of the solar wind (Van Doorsselaere et al., 2011). This set of parameters produce a mass-loss rate of $\sim 3 \times 10^{-12}$ $M_\odot$ yr^{-1} for HD189733, which is in the range of inferred mass-loss rates for active K stars (see Wood, 2004; Jardine & Collier Cameron, 2019; Rodríguez et al., 2019).

To simulate the wind variability of HD189733, we implement surface magnetic field maps obtained for the star at different epochs, which were reconstructed from observations by Fares et al. (2017) using the ZDI technique. The maps implemented were obtained at the epochs Jun/Jul 2013, Sep 2014, and Jul 2015, and are shown in Figure 2.1. These maps allow us to estimate the yearly variability

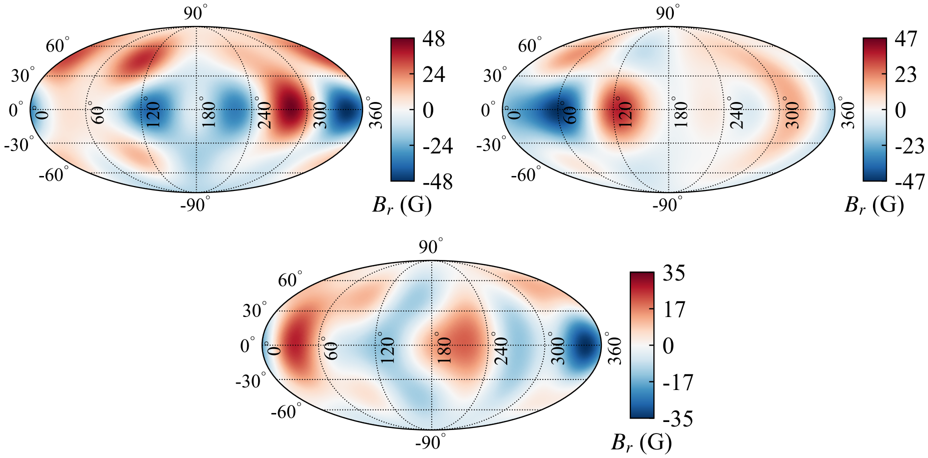

Figure 2.1: Mollweide projections of the radial surface magnetic field of HD189733 at the three epochs Jun/Jul 2013 (top left), Sep 2014 (top right), and Jul 2015 (bottom), which were reconstructed from observations by Fares et al. (2017). We implement these as boundary conditions in our stellar wind simulations.

of the stellar wind properties and the planetary radio emission. The field strength at these epochs are also some of the largest observed for the star, for which we expect should drive strong radio emission from the planet. We simulate the wind with a grid that extends from $-20\ R_\star$ to $+20\ R_\star$ along the x, y, and z axes, with the star at the centre. To solve for the magnetic field in the wind, we fix the radial component B_r based on the ZDI map at each epoch, and assume an outflow or 'float' condition for meridional B_θ and azimuthal B_ϕ components, where we take their derivative with respect to the radial coordinate to be zero. We also incorporate adaptive mesh refinement in our grid. Our grid resolution ranges from $\sim 0.01\ R_\star$ to $0.3\ R_\star$, with the finest resolution occurring in the region from $1\ R_\star$ to $2\ R_\star$. This is equivalent to a refinement level of 10 quoted in Nicholson et al. (2016), and has a total of 39 million cells. Nicholson et al. (2016) investigated the effects of increasing the grid resolution to a refinement level of 11 on the derived global wind properties, and obtained marginally more accurate results. Given that the large number of cells in a grid of this size ($\sim$ 300 million) is very computationally expensive, we adopt a refinement level of 10 in this work.

With everything in place, we set our simulation to run until a steady state is obtained. We take this to be the point where various global wind properties such as the mass-loss and angular momentum-loss rates vary by $< 1\%$ between iterations. The stability of these values as a function of distance from the star also indicates that a steady state has been obtained. When these conditions are satisfied, we take the wind model to be complete.

2.3.2 Stellar wind variability of HD189733

From our simulations, we derive the global wind properties of HD189733 at Jun/Jul 2013, Sep 2014, and Jul 2015, as described by Vidotto et al. (2015). The mass-loss rate $\dot{M}$ of the star is calculated as:

$$\dot{M} = \oint_S \rho u_r dS, \tag{2.6}$$

where S is a spherical surface above the stellar surface at a specified distance. The angular momentum-loss rate of the star $\dot{J}$ is calculated as the flux of angular momentum through S:

$$\dot{J} = \oint_S \left[-\frac{\varpi B_\varphi B_r}{4\pi} + \varpi u_\varphi \rho u_r \right] dS, \tag{2.7}$$

where $\varpi = (x^2 + y^2)^{1/2}$ is the cylindrical radius. The unsigned open magnetic flux of the stellar wind $\Phi_{\rm open}$ is:

$$\Phi_{\rm open} = \oint_S |B_r| dS. \tag{2.8}$$

We compute $\dot{M}$, $\dot{J}$, and $\Phi_{\rm open}$ at concentric spherical surfaces S around the star from 10 $R_\star$ to 20 $R_\star$, and take the average value in this region. Our computed values are listed in Table 2.2. We find that the wind properties of HD189733 vary over time in response to its changing magnetic field topology, with the mass-loss rate, angular momentum-loss rate, and open magnetic flux varying by 9%, 40%, and 19% respectively over the three modelled epochs, relative to the maximum over the three epochs. These results are comparable to those found by other stellar/solar wind models (Vidotto et al., 2012; Nicholson et al., 2016; Réville & Brun, 2017), wherein small variations in $\dot{M}$ (>20%) and large variations in $\dot{J}$ (~50-140%) are seen over timescales of half to multiple magnetic cycles.

As we implement magnetic field maps with complex topologies in our wind simulations, we find that the wind of HD189733 is inhomogeneous. This can be seen in the profiles of the radial wind velocity in Figure 2.2. As a result, the planet experiences a non-uniform wind as it progresses through its orbit. Table 2.3 lists the average values of various wind properties at the planetary orbit at 8.8 $R_\star$, as well as their min/max values in the orbit. We find that the particle number density and velocity of the wind relative to the motion of the planet vary from 29-37% and 25-32% respectively throughout the orbit across the three epochs. These variations are likely to be observable in the UV transit of the planet (Lecavelier des Etangs et al., 2012; Bourrier & Lecavelier des Etangs, 2013). From a previous transit of the planet in 2011, Bourrier & Lecavelier des Etangs (2013) derived a stellar wind velocity of 200 km s^{-1} and density of 10^6 cm^{-3} for HD189733 at the planetary orbit, based on the Lyman-α absorption from the extended atmosphere of the planet in the saturation regime. These values are in good agreement with the stellar wind properties at the planetary orbit in our models. Our temperature however is a factor of ~ 30 higher than their derived value of 3×10^4 K. The cause

Table 2.2: Global wind properties derived for HD189733 in Jul/Jul 2013, Sep 2014, and Jul 2015. The values listed are the mass-loss rate $\dot{M}$, angular momentum-loss rate $\dot{J}$, unsigned open magnetic flux $\Phi_{\rm open}$, and unsigned magnetic flux at the surface Φ_0.

Epoch	$\dot{M}$	$\dot{J}$	$\Phi_{\rm open}$	Φ_0
	(10^{-12} $M_\odot$ yr^{-1})	(10^{31} erg)	(Φ_0)	(10^{23} Mx)
2013	3.2	5.5	0.39	4.5
2014	3.0	5.2	0.48	3.0
2015	2.9	3.3	0.40	2.7

of this discrepancy could be due the fact that our models do not consider detailed heating and cooling mechanisms for the stellar wind (Vidotto & Bourrier, 2017).

We also calculate the average value of the magnetic field strength at the orbit of the planet for each epoch. We find that the ambient field around the planet at the three epochs are 62.1, 55.6, and 44.6 mG respectively, which are about twice the values calculated using the potential field source surface method (PFSS) (Fares et al., 2017). This is due to the assumption in the PFSS method that the stellar magnetic field is in its lowest energy state, which neglects that the stellar wind stresses on the stellar magnetic field lines. From the total pressure values (ram, thermal, and magnetic pressures) listed in Table 2.3, we also see that HD189733b is subjected to a wind pressure that varies by over 2 orders of magnitude throughout its orbit and over time.

In Figure 2.2 we also show that at each epoch the planet orbits outside of the Alfvén surface, where the wind poloidal velocity equals the Alfvén velocity: $v_{\rm A} = B_{\rm pol}/\sqrt{4\pi\rho}$ ($B_{\rm pol}$ is the poloidal magnetic field strenght of the stellar wind). This means the planet is orbiting in the ram pressure-dominated region of the wind. As a result, we do not expect any magnetic star-planet interactions (SPI) at these epochs, as information cannot propagate back to the star (Shkolnik et al., 2008; Lanza, 2012). However, due to the variability of the stellar magnetic field, there may be epochs in which the planet orbits inside the Alfvén surface, and is in direct connection to the star. During these epochs, the planet may induce hot chromospheric spots in the star. For instance, Cauley et al. (2018) recently reported Ca II K modulations with a period coinciding with the planetary orbital period of 2.2 days in Aug 2013, implying that magnetic SPI may have occurred at this epoch.

2.3.3 Radio emission from the stellar wind

We calculate the free-free radio emission of the stellar wind of HD189733, implementing the numerical code developed by Ó Fionnagáin et al. (2019a). In this model, we solve the equations of radiative transfer for our wind models, assuming that it emits as a blackbody. The equations are solved for the line of sight of an observer placed at $x = -\infty$, looking towards the star. The choice of the direction of the line of sight has negligible effects on the results of our calculations. We compute the free-free radio spectrum for the wind of HD189733 in the frequency range of 10 MHz to 100 GHz. In this region, we find that there are negligible dif-

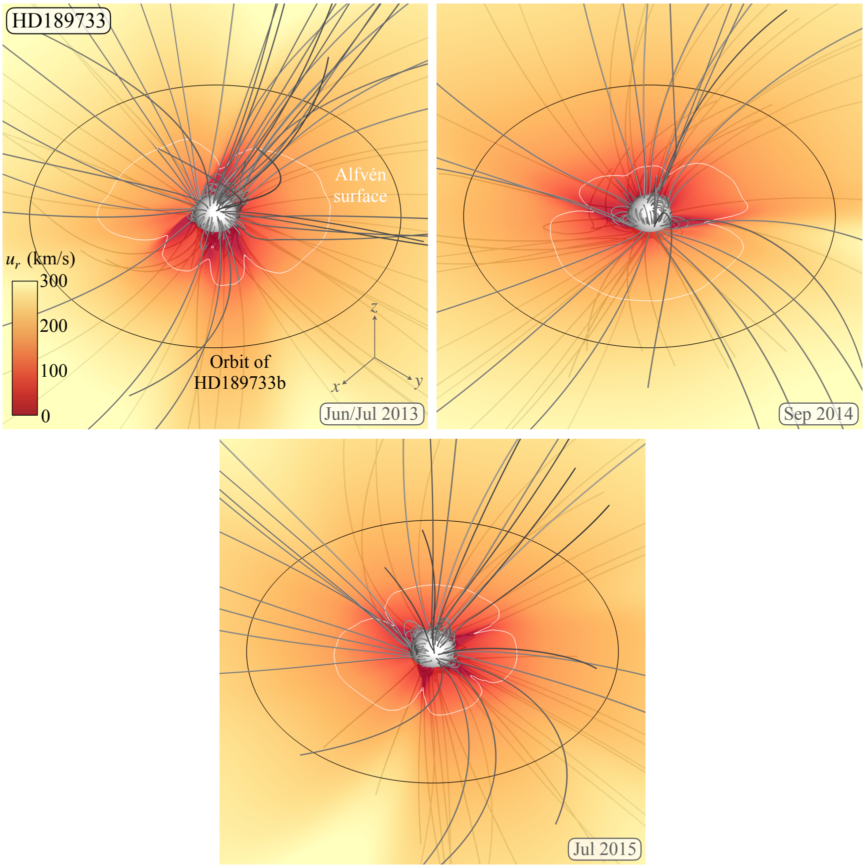

Figure 2.2: Simulated stellar wind of HD189733 in Jun/Jul 2013 (top left), Sep 2014 (top right), and Jul 2015 (bottom). Grey lines show the large-scale structure of the magnetic field of HD189733, which is embedded in the stellar wind. Profiles of the radial velocity (u_r) of the stellar wind in the orbital plane of the planet are shown. The orbit at 8.8 $R_\star$ is shown with a black circle, and Alfvén surfaces are shown in white. The orientation in each panel is the same.

Table 2.3: Average stellar wind parameters of HD189733 at the planetary orbit for each modelled epoch. The values listed are the particle number density n, velocity in the reference frame of the planet Δu, magnetic field strength B, temperature T, and total pressure $p_{\rm tot}$ of the stellar wind. The values quoted in square brackets are the min/max value of each parameter throughout the orbit, respectively.

Epoch	$\langle n \rangle$ (10^6 cm^{-3})	$\langle \Delta u \rangle$ (km s^{-1})	$\langle B \rangle$ (mG)	$\langle T \rangle$ (10^6 K)	$\langle p_{\rm tot} \rangle$ (10^{-4} dyn cm^{-2})
2013	4.0	235	62.1	1.03	1.71
	[3.3, 5.2]	[188, 270]	[2.2, 84.9]	[0.94, 1.22]	[$<$0.01, 2.87]
2014	3.8	220	55.6	0.97	1.37
	[3.0, 4.7]	[183, 271]	[1.9, 79.1]	[0.93, 1.17]	[$<$0.01, 2.49]
2015	3.7	212	44.6	0.95	0.86
	[3.2, 4.5]	[196, 260]	[3.9, 57.8]	[0.92, 1.05]	[0.01, 1.33]

ferences between the fluxes for each epoch. Figure 2.3 shows the spectra calculated for Jun/Jul 2013. The flux densities calculated range from $\sim 10^{-3}$ to 5 μJy. At such low flux densities, this emission is unlikely to be detected with current radio telescopes. However, future developments, such as the Square Kilometre Array (SKA), are likely to allow for the detection of this emission from low mass stars, such as HD189733 (see Section 2.6).

We also find that the wind of HD189733 becomes optically thin at 10 GHz. For frequencies less than this, regions of the wind are optically thick, which become larger towards lower frequencies. Inside these regions or ‘radio photospheres’, the wind will self-absorb its own emission. In addition to this, if the planet emits cyclotron emission and orbits within the radio photosphere for the emitted frequency, this emission would also be absorbed by the stellar wind. We investigate this scenario in Section 2.5.1.

We note that the free-free radio emission from the stellar wind depends on the density profile of the wind, which is determined by coronal base density n_0, a free variable in our simulations. We discuss the effects of a lower density wind on the radio emission in the Appendix.

2.4 Predicting planetary radio emission from HD189733b

To predict the planetary radio emission from HD189733b, we follow the description by Vidotto & Donati (2017) (see also works by Zarka, 2007). Pressure balance between the stellar wind (ram, thermal, and magnetic) and the planet (magnetic) pressures gives us the size of the planetary magnetopause $R_{\rm m}$:

$$R_{\rm m} = 2^{1/3} \left[\frac{(B_{\rm p}/2)^2/8\pi}{\rho \Delta u^2 + p + B^2/8\pi} \right]^{1/6} R_{\rm p}, \tag{2.9}$$

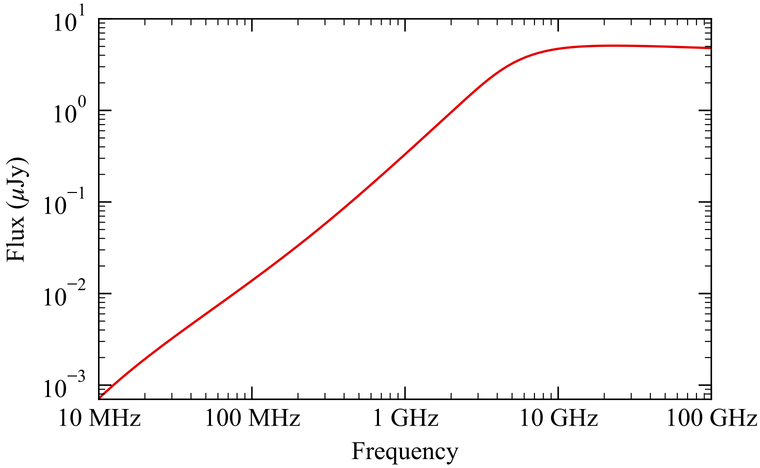

Figure 2.3: Free-free radio emission spectra of the stellar wind of HD189733 at Jun/Jul 2013. There are negligible differences between the wind spectra for the three modelled epochs.

where B_p is the strength of the dipolar planetary magnetic field at the poles, R_p is the planetary radius, and Δu is the magnitude of the relative velocity between the wind u and Keplerian velocity of the planet u_K: $\boldsymbol{\Delta u} = \boldsymbol{u} - \boldsymbol{u}_\mathrm{K}$, $u_\mathrm{K} = \sqrt{GM_\star/a}$. Note that we neglect the ram and thermal components of the planetary pressure. In our model, the radio emission arises from polar cap regions at co-latitudes α_0 from the poles:

$$\alpha_0 = \sin^{-1}\left[\left(\frac{R_\mathrm{p}}{R_\mathrm{m}}\right)^{1/2}\right]. \tag{2.10}$$

Assuming an aligned dipolar planetary magnetic field, the field strength at this co-latitude is:

$$B(\alpha_0) = \frac{B_\mathrm{p}}{2}\left(1 + 3\cos^2\alpha_0\right)^{1/2}. \tag{2.11}$$

Radio emission then occurs via the Cyclotron Maser instability at a maximum frequency of:

$$f_\mathrm{c} = 2.8\left(\frac{B(\alpha_0)}{1\ \mathrm{G}}\right)\ \mathrm{MHz}. \tag{2.12}$$

The polar cap region where this emission originates forms a hollow cone with solid angle ω:

$$\omega = 8\pi\sin\alpha_0\sin\frac{\delta\alpha}{2}, \tag{2.13}$$

where $\delta\alpha$ is the thickness of the cone. We adopt a value of $\delta\alpha = 17.5°$, which is the estimated thickness for Jupiter's emission cone (Zarka et al., 2004).

Combining all this gives us an expression for the radio flux received from the system. The magnetic power dissipated by the wind onto the magnetosphere of the planet is given by:

$$P_B = \frac{B_\perp^2}{4\pi} \Delta u \pi R_\mathrm{m}^2, \tag{2.14}$$

where $B_\perp$ is the magnitude of the magnetic field of the stellar wind perpendicular to the vector $\boldsymbol{\Delta u}$. In our model, we compute this as:

$$B_\perp = \sqrt{B^2 - \left(\frac{\boldsymbol{B} \cdot \boldsymbol{\Delta u}}{\Delta u} \right)^2}. \tag{2.15}$$

The flux density received by an observer at a distance $d = 19.8$ pc is then given by:

$$\Phi_\mathrm{radio} = \frac{\eta_B P_B}{d^2 \omega f_\mathrm{c}}. \tag{2.16}$$

Here, η_B is the efficiency ratio for the magnetic power dissipated onto the planetary magnetosphere, which we take as the solar system value of 2×10^{-3} (Zarka, 2007). This constant arises from the radiometric Bode's law. Numerical studies have found that the radiometric Bode's law is appropriate for estimating radio emission from hot Jupiters (Varela et al., 2018), while some have suggested that it may overestimate the flux densities for close-in planets (Nichols & Milan, 2016). If this is indeed the case, the values we obtain here should be treated as upper limits. As we demonstrate in Section 2.5, there are several scenarios where in fact propagation of planetary radio emission may not be possible.

In the above equations we use the velocity, density, pressure, and magnetic field of the stellar wind at the planetary orbit, obtained from our wind models presented in Section 2.3.2. In our calculations, we assume planetary magnetic field strengths of $B_\mathrm{p} = 1$, 5, and 10 G, which covers the range of values predicted for extrasolar gas giants (Zaghoo & Collins, 2018). Table 2.4 shows the calculated cyclotron frequency, magnetopause size, and co-latitude of the polar cap of HD189733b, as a function of planetary magnetic field strength. We find that these three quantities vary by small amounts throughout the orbit and between the three epochs for a given field strength. The flux densities of the radio emission however varies by around two orders of magnitude throughout the orbit. The variations of the fluxes calculated for $B_\mathrm{p} = 10$ G throughout the orbit of the planet, and the peak fluxes at each epoch for different planetary field strengths, are shown in Figure 2.4. In the top panel of Figure 2.4, we see that the flux density goes to zero at points in the orbit where $B_\perp = 0$ in the stellar wind (see Equation 2.14). We also see a general trend towards lower peak fluxes from Jun/Jul 2013 to Jul 2015 in the bottom panel of Figure 2.4. This correlates to the trend in the average magnetic field strength of the wind at the planetary orbit shown in Table 2.3.

Comparing to recent work, Zaghoo & Collins (2018) estimated a flux of $\sim$ 20 mJy at a peak cyclotron frequency of 20 MHz for HD189733b. Our peak flux densities are ~ 5 times larger than theirs, which is likely due to their assumption for the stellar wind power, which they extrapolated from the solar wind. As we have shown in Section 2.3.2, the wind strength of HD189733 is much stronger than the solar wind. As a result, we expect that HD189733b receives a higher magnetic energy from the wind of its host star, and thus higher fluxes will be emitted.

Table 2.4: Emitted cyclotron frequency, magnetopause size, and co-latitude of the polar cap of HD189733b, calculated for different planetary magnetic field strengths. These values only vary by small amounts through the orbit and between each epoch.

B_p (G)	f_c (MHz)	R_m (R_p)	α_0 (°)
1	2	1.6	53
5	12	2.7	38
10	25	3.3	33

Our findings tell us that while the flux density of the planetary emission is sensitive to inhomogeneities in the stellar wind, the frequency of the emission is not. The combination of these two results could allow for planetary radio emission to be easily distinguished from other sources of radio emission in the system, such as the stellar wind. The fluxes and frequencies calculated for HD189733b also place it within the detection limit of LOFAR. We discuss this further in Section 2.6.

2.5 Propagation of the planetary radio emission

While we have made predictions about the planetary radio emission for different assumed magnetic field strengths, the question remains: can the emission propagate out of the planetary system? We discuss different scenarios where propagation may not be possible below.

2.5.1 Free-free absorption in the stellar wind

One scenario where the planetary radio emission may not propagate from the system is if the planet orbits inside the radio photosphere of the star. From the model utilised in Section 2.3.3, we calculate the boundary of the photospheres of the stellar wind for the calculated cyclotron frequencies of 2, 12, and 25 MHz, which we chose as they correspond to planetary field strengths of 1, 5, and 10 G (see Table 2.4). The radio photosphere is defined as the point where the optical depth $\tau = 0.399$ (Panagia & Felli, 1975).

Figure 2.5 shows a 3D view of the radio photosphere of the wind of HD189733 at 25 MHz for Jun/Jul 2013, as viewed by an observer at $x = -\infty$. The radio photosphere is paraboloidal in shape. Inside the region enclosed by the surface shown, emission at 25 MHz will be absorbed by the stellar wind. We see that part of the planetary orbit is embedded in this region. In Figure 2.6, we show the boundaries of these regions for the three epochs at 2, 12, and 25 MHz in the orbital plane of the planet. The thickness of these boundaries at each frequency arises from the different positions of the radio photosphere for the three epochs. From the boundaries, we find that the planetary radio emission can propagate for 41% of the orbit at 12 MHz, and 67% at 25 MHz. The planet's orbit is fully embedded in the region of the wind that is optically thick at 2 MHz. This frequency is below the ionospheric cutoff of the Earth's atmosphere. As the radio flux densities of the planet are several orders of magnitude higher than those of the stellar wind (see

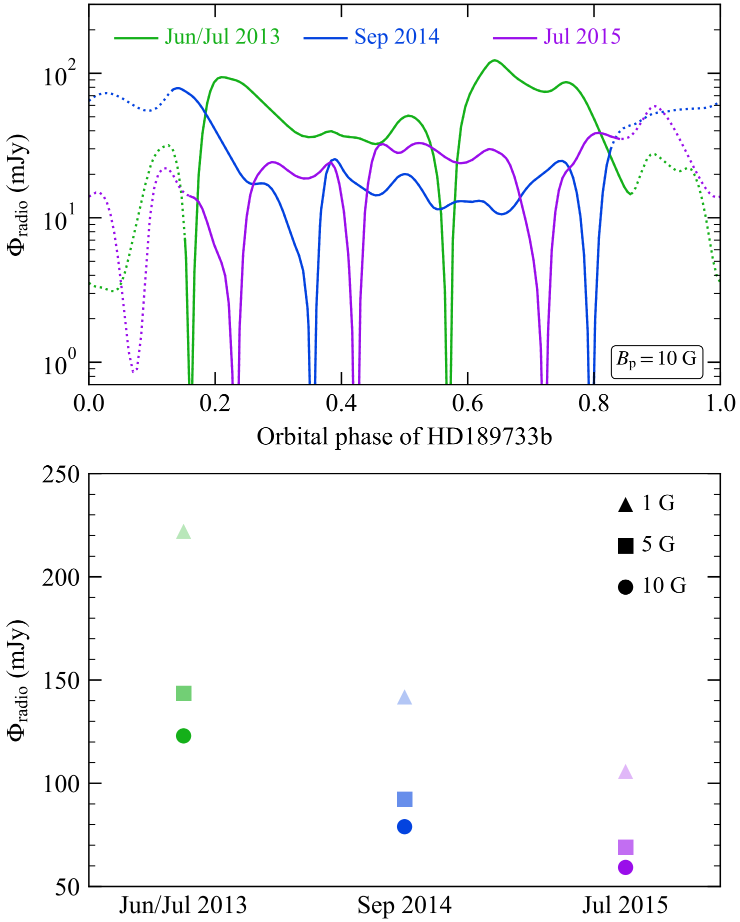

Figure 2.4: *Top*: Variations of the planetary radio flux throughout the orbit of HD189733b for the three epochs, for a field strength of $B_{\rm p} = 10$ G. The dotted segment of each line represents the region of the orbit where the planetary radio emission at 25 MHz, corresponding to a planetary field strength of 10 G, cannot propagate through the stellar wind (see Section 2.5.1). *Bottom*: Peak radio flux densities calculated for HD189733b, for planetary field strengths of 1, 5, and 10 G at each epoch.

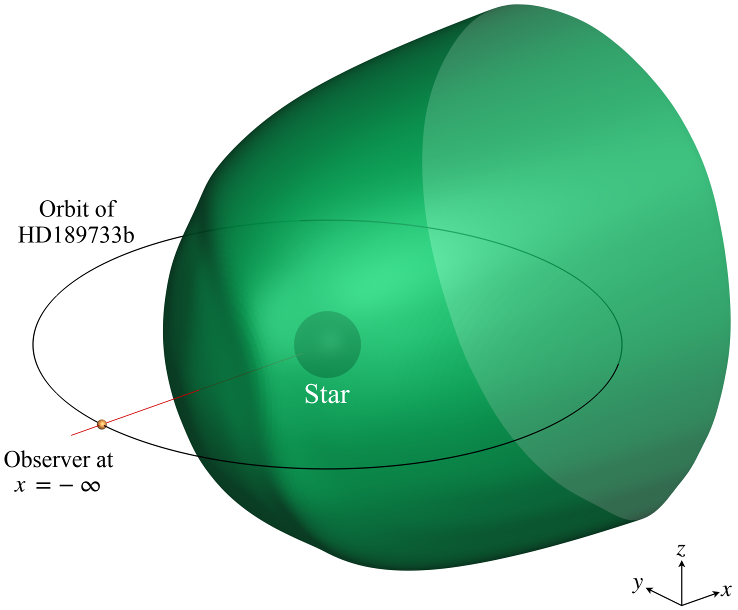

Figure 2.5: Radio photosphere of the stellar wind of HD189733 at 25 MHz for Jun/Jul 2013, as viewed by an observer at $x = -\infty$. The region enclosed by the surface is where planetary radio emission at 25 MHz cannot propagate without being absorbed. The red line illustrates the line connecting the planet to the star seen by the observer. Note that the size of the photosphere, star, planet and its orbit are to scale here. The radio photosphere extends back to $x = 10\ R_\star$.

Figure 2.8), it could be that even after the planetary emission is attenuated inside the radio photosphere of the stellar wind, a fraction of the planetary emission may still escape.

The fraction of the orbit where the emission can propagate unattenuated to an observer at Earth corresponds to when the planet is approaching and leaving primary transit. This may be a useful signature to search for in other exoplanetary radio surveys. Indeed, Smith et al. (2009) reported a non-detection of HD189733b during secondary transit, the region where we expect the wind to be optically thick for frequencies below 10 GHz. We note however that the frequency range of their observations correspond to planetary field strengths of ~ 100 G, which is likely to be too strong for a hot Jupiter planet such as HD189733b (see Zaghoo & Collins, 2018). It is clear however that detection of planetary radio emission is more favourable for higher frequencies, which correspond to strong planetary magnetic field strengths. We caution that the size of the radio photosphere at a specific frequency scales with the density of the stellar wind, which is a free variable in our model. The effects of varying the density on the size of these regions are discussed in the Appendix.

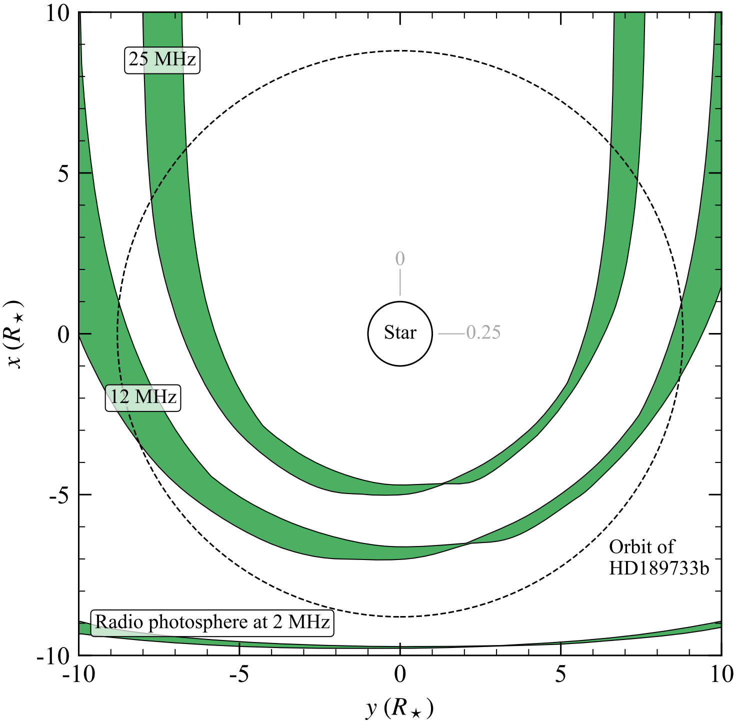

Figure 2.6: Radio photospheres of the stellar wind at the calculated frequencies of 2, 12, and 25 MHz, in the orbital plane of the planet. The planetary orbit is shown as a black dashed circle, and the star is shown in the centre. Orbital phases of 0 and 0.25 are marked near the star. In our calculation, the observer is looking along the x-axis in the positive direction.

2.5.2 Plasma frequency of the stellar wind

Another process by which the planetary emission may not be able to escape the system is if the cyclotron frequency is less than the plasma frequency of the stellar wind at the planetary orbit. The plasma frequency is defined as:

$$f_{\rm p} = 9 \times 10^{-3} \sqrt{\frac{n_e}{1\ {\rm cm}^{-3}}}\ {\rm MHz}. \tag{2.17}$$

where n_e is the number density of free electrons. We take this to be equal to the number density of protons in our wind, as it is fully ionised.

Neglecting the presence of the planetary atmosphere, the radio emission can propagate out from the polar emission region. However, if the emitted frequency is below the plasma frequency of the stellar wind it meets, the planetary radio emission will be reflected back and hence will not propagate out of the planetary system. This is the same process which prevents sources of radio emission below 10 MHz from penetrating the Earth's ionosphere. Figure 2.7 shows the plasma frequency of the stellar wind at the planetary orbit for the three modelled epochs. We find that only cyclotron frequencies above $\sim$ 21 MHz will be able to propagate through the stellar wind for the entirety of the orbit at the three modelled epochs. This requires a minimum planetary field strength of $\sim$ 8 G, based on the values listed in Table 2.4.

We note that the plasma frequency of the stellar wind will also scale with the wind density. For a wind that is 10 times less dense, the plasma frequency of the wind is reduced by a factor of $\sqrt{10}$, thus lowering the minimum planetary field strength required for the planetary emission to propagate to $\sim$ 3 G.

2.5.3 Generation of cyclotron emission in an extended atmosphere

Another potential issue for the detection of planetary radio emission is the planetary atmosphere itself. Recently, Weber et al. (2018) suggested that while close-in hot Jupiters are exposed to more energetic winds that could boost their radio emission, they also receive much higher XUV fluxes from their host stars. As a result, their atmospheres extend far out from the planet and have a higher free electron density. From Equation 2.17, this means that the plasma frequency of the atmosphere becomes very large. Therefore, a planetary field strength of hundreds of G would be required for the generated cyclotron frequency to be above the plasma frequency of the atmosphere. They suggest however that supermassive hot Jupiters may be more suitable targets for detection of planetary radio emission. As their atmospheres would be more tightly bound, the free electron density drops off more sharply with distance from the planet, and thus the radio emission can be generated above the plasma frequency of the atmosphere.

In our planetary radio emission model, we do not account for the presence of a planetary atmosphere, and so we were unable to test the predictions of Weber et al. (2018). Recently however, Daley-Yates & Stevens (2018) modelled the MHD equations of both the stellar and planetary winds of a solar-type star host to a

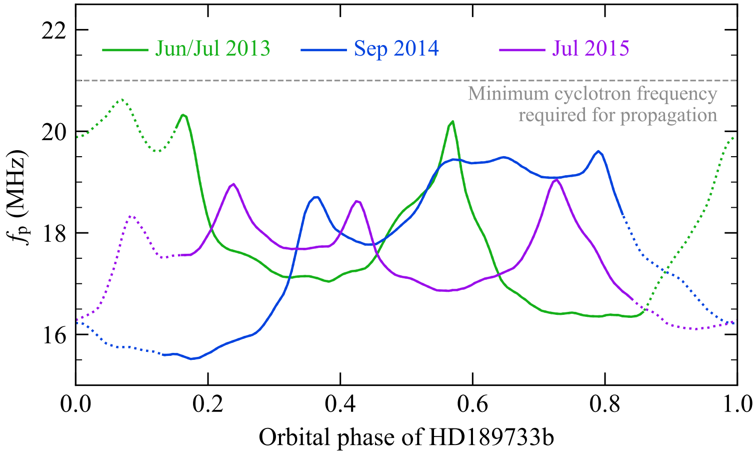

Figure 2.7: Variations of the plasma frequency of the stellar wind at the planetary orbit for each modelled epoch. The minimum cyclotron frequency of ∼ 21 MHz required for the planetary emission to propagate through the stellar wind is marked with a grey dashed line. The dotted line segments illustrate where the planetary radio emission is absorbed by the stellar wind at 25 MHz (see Section 2.5.1).

hot Jupiter-type planet. They found that the generated cyclotron frequency in the planetary magnetosphere was at least a factor of 10 lower than the plasma frequency throughout the planetary atmosphere. As it is expected that the atmosphere of HD189733b is extended (Lecavelier des Etangs et al., 2012; Bourrier & Lecavelier des Etangs, 2013), it could prevent the generation of cyclotron emission in the case of HD189733b.

2.6 Detection potential with current and future radio telescopes

From our calculations of the radio emission from the planetary magnetosphere and the wind of the host star, it is clear that their radio signatures are very different. For the planet, it emits at a constant single frequency for a given planetary field strength, with the flux of its emission varying from ∼ 1 to 10^2 mJy as it progresses through its orbit. The stellar wind on the other hand emits at much lower fluxes across a range of frequencies. In the region of 10 MHz to 100 GHz, the wind fluxes range from ∼ 10^{-3} to 5 μJy. Therefore, the peak flux from the wind emission is four orders of magnitude smaller than the peak flux of the planet. As a result, it should be straightforward to distinguish between the planetary and wind emission.

Figure 2.8 shows a comparison between the predicted fluxes from the planet and wind of the host star, along with the sensitivities of LOFAR and SKA2. We see that for a planetary field strength of 5 G, the corresponding cyclotron frequency of 12 MHz is below the lower frequency limit of LOFAR quoted by

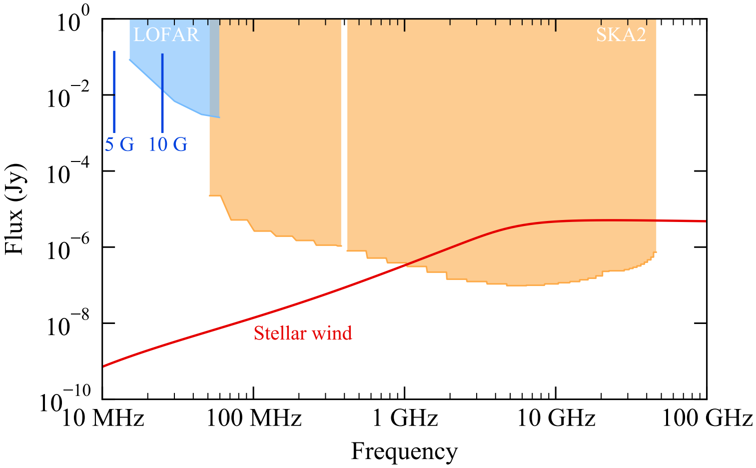

Figure 2.8: Comparison of the predicted radio flux densities and frequencies of HD189733b, for assumed planetary field strengths of 5 and 10 G, and the stellar wind of its host star. The peak planetary flux density shown is the max over the three epochs for a given field strength, with a lower limit set of 1 mJy. The stellar wind spectrum is the same as shown in Figure 2.3. The sensitivities of LOFAR and SKA2 for a 1 hour integration time are also shown, adapted from Grießmeier et al. (2011) and Pope et al. (2019) respectively.

Grießmeier et al. (2011). However, we determined in Section 2.5 that propagation of emission below 21 MHz is unlikely. For the stellar wind, we see that SKA2 is likely to have sufficient sensitivity to determine at which frequency it becomes optically thin. If so, this would allow for the base density of the stellar wind n_0 to be constrained, and consequently the mass-loss rate of the star (see Appendix).

We note that there are likely additional sources of radio emission in planetary system, such as thermal emission from the stellar chromosphere (Villadsen et al., 2014; Fichtinger et al., 2017). However, we do not investigate this in this work.

2.7 Summary & Conclusions

In this work we have characterised the radio environment of the hot Jupiter HD189733b. For its host star HD189733, we performed 3D MHD simulations of its wind, implementing surface magnetic field maps at the epochs Jun/Jul 2013, Sep 2014, and Jul 2015, which were reconstructed from observations. We used our models to calculate the wind variability of HD189733, and determined that the mass-loss rate, angular momentum-loss rate, and open magnetic flux vary by 9%, 40%, and 19% over this period respectively. We also found from our wind models that the planet experiences a non-uniform wind as it progresses through its orbit, with the wind velocity and particle number density varying by 29-37% and 25-32% respectively over the three modelled epochs. Temporal variations were observed in the extended atmosphere of HD189733b (Lecavelier des Etangs et al., 2012), which could arise from interactions with a variable stellar wind (Bourrier & Lecavelier des Etangs, 2013). Our derivation of the stellar wind properties at the planetary orbit for different epochs will thus be useful to the interpretation of our MOVES observations of the upper planetary atmosphere.

Using the numerical code developed by Ó Fionnagáin et al. (2019a), we calculated the free-free radio spectrum of the wind of HD189733. We found that it emits at low fluxes of 10^{-3} to 5 μJy in the frequency range of 10 MHz to 100 GHz. While it is unlikely that this could be detected with current radio telescopes, future endeavours such as SKA are likely to have the sensitivity required to characterise the radio emission from the winds of stars such as HD189733. If detectable, the mass-loss rate of star could be constrained.

Our wind models provided us with the local wind properties at the planetary orbit, which in turn we used to calculate the planetary radio emission. For assumed planetary field strengths of 1, 5, and 10 G respectively, we found that the planet emits at frequencies of 2, 12, and 25 MHz, with little variation in these values over the modelled period and the orbit of the planet. The emitted flux density however varies from 1 to 10^2 mJy in our calculations. Therefore, a frequency corresponding to a field strength $\gtrsim$ 10 G places HD189733b within the detection limit of LOFAR.

We investigated if our predicted planetary radio emission could propagate, and found that HD189733b orbits in and out of regions where the planetary emission will be absorbed by the stellar wind. For the calculated cyclotron frequencies of 12 and 25 MHz, we found that propagation can only occur for 41% and 67% of the orbit respectively. The fraction of the orbit where propagation is possible corresponds to when the planet is approaching and leaving primary transit of the host star. This could be useful information in planning radio observing campaigns of exoplanetary systems. However, as the radio flux densities of the planet are several orders of magnitude higher than those of the stellar wind, some of the planetary emission may still escape even after being attenuated in the stellar wind. We also determined that the plasma frequency of the stellar wind at the planetary orbit is too high for propagation to occur below 21 MHz at the three modelled epochs. In addition to this, the planetary atmosphere itself may prevent the generation of radio emission, as has been recently suggested by Weber et al. (2018).

To conclude, our work has shown that the most favourable candidates for detection of planetary radio emission are hot Jupiters with large magnetic field strengths, orbiting inactive stars with low density winds.

Acknowledgements

The authors thank the anonymous referee for their comments and suggestions. RDK acknowledges funding received from the Irish Research Council through the Government of Ireland Postgraduate Scholarship Programme. RDK and AAV also acknowledge funding received from the Irish Research Council Laureate Awards 2017/2018. VB acknowledges support by the Swiss National Science Foundation (SNSF) in the frame of the National Centre for Competence in Research PlanetS, and has received funding from the European Research Council (ERC) under the European Union's Horizon 2020 research and innovation programme (project Four Aces; grant agreement No 724427). This work was carried out using the BATSRUS tools developed at The University of Michigan Center for Space Environment Modeling (CSEM) and made available through the NASA Community Coordinated Modeling Center (CCMC). The authors also wish to acknowledge the SFI/HEA Irish Centre for High-End Computing (ICHEC) for the provision of computational facilities and support.

Appendix: Radio emission and absorption for a lower density stellar wind

The free-free radio emission spectrum of the stellar wind depends on the density. The density profile is primarily determined by the coronal base density in our wind simulations n_0, which is a free variable. To see the effect of a lower density wind on the free-free radio spectrum of HD189733, we divide our density values from the wind simulations by a factor of 10.

Figure 2.9 shows the comparison of the spectrum shown in Figure 2.3 and the spectrum calculated for the lower base density wind. We find that the lower density wind becomes optically thin at 1 GHz, as opposed to 10 GHz for the higher density wind. We also see that for the lower density wind, the radio flux densities are 1-2 orders of magnitude smaller that those for the $n_0 = 10^{10}$ cm^{-3} wind. So, detection of free-free emission from the stellar wind of HD189733 is more favourable if it has a denser wind. However, the fluxes calculated for the higher density wind are still quite small. While it is unlikely that this could be detected with current radio telescopes, it is expected that future developments such as SKA will allow for radio emission from the winds of nearby low mass stars to be detected (see Ó Fionnagáin et al., 2019a). By determining the frequency at which the wind becomes optically thin, the mass-loss rate of the star could be constrained.

We also show the planetary flux densities for 5 and 10 G in Figure 2.9, which have been scaled for the lower density stellar wind. Assuming the planet remains orbiting in the ram-pressure dominated regime for the lower density wind, the planetary radio flux scales with ${n_0}^{-1/2}$ (Vidotto & Donati, 2017). The frequency of the planetary emission has a very small dependence on the stellar wind density, as the magnetopause size R_m scales with ${n_0}^{-1/6}$ in this regime (see Equations 2.9 to 2.12).

The sizes of the radio photospheres of the wind will also depend on the wind density. Figure 2.10 shows the boundaries of these regions at the three calculated cyclotron frequencies in the orbital plane of the planet for the lower density wind. We see that for a lower density, the regions the planet orbits through where wind is optically thick to the cyclotron frequencies are smaller compared to those shown in Figure 2.6 at a given frequency. Therefore, contrary to the wind radio emission, detection of planetary radio emission is more favourable for planets orbiting stars with low density winds.

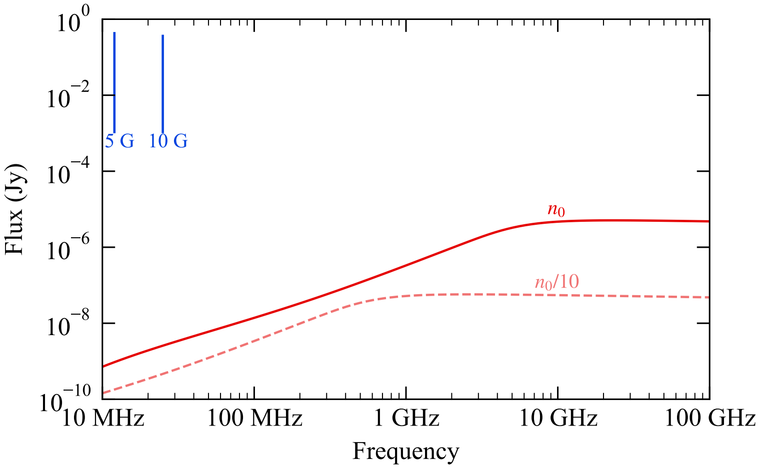

Figure 2.9: Comparison of the free-free radio spectrum of the stellar wind of HD189733 from Figure 2.3 (n_0), with a stellar wind that has a density which is a factor of 10 lower ($n_0/10$). The planetary flux densities for assumed field strengths of 5 and 10 G are also shown in the upper left corner. The peak values of the planetary fluxes have been scaled for the lower density stellar wind from those shown in Figure 2.8.

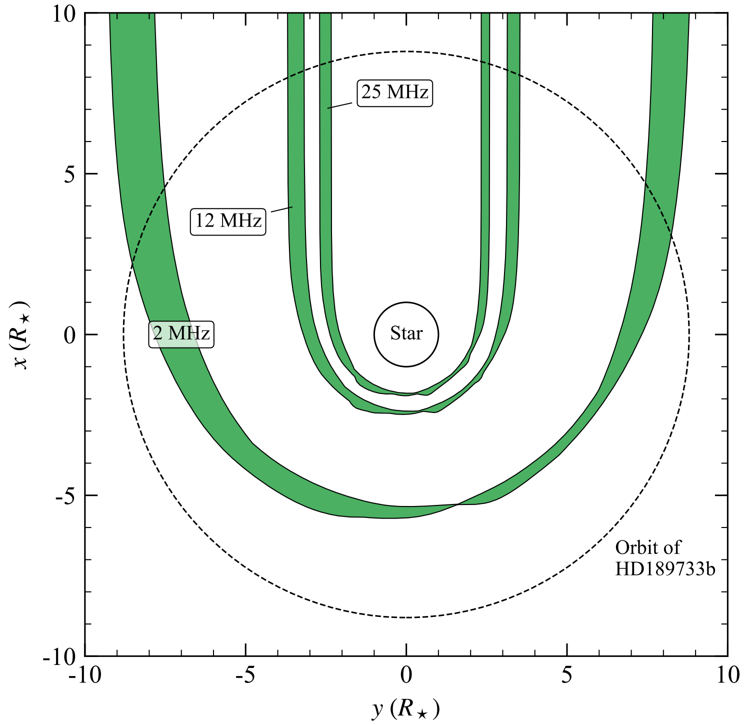

Figure 2.10: Radio photospheres of the stellar wind of HD189733, for a stellar wind that is a factor of 10 lower in density. The sizes of the radio photospheres of the lower density wind at a given frequency are smaller compared to those shown in Figure 2.6.

3 | Radio eclipses of exoplanets by the winds of their host stars

3.1 Abstract

The search for exoplanetary radio emission has resulted in zero conclusive detections to date. Various explanations for this have been proposed, from the observed frequency range, telescope sensitivity, to beaming of the emission. In a recent paper, we illustrated that exoplanets can orbit through the radio photosphere of the wind of the host star, a region that is optically thick at a specific frequency, for a large fraction of their orbits. As a result, radio emission originating from the planet could be absorbed or 'eclipsed' by the wind of the host star. Here we investigate how the properties of the stellar wind and orbital parameters affect the fraction of the orbit where the planet is eclipsed by the stellar wind. We show that planets orbiting stars with low density winds are more favourable for detection in the radio. In terms of the orbital parameters, emission from transiting planets can escape the stellar wind easiest. We apply our model to the τ Boo planetary system, and show that observing the fraction of the planet's orbit where it is eclipsed by the wind of the host star could be used to constrain the properties of the stellar wind. However, our model developed would need to be used in conjunction with a separate method to disentangle the mass-loss rate and temperature of the stellar wind.

3.2 Introduction

Over the last few decades, the search for exoplanetary radio emission has been motivated by the desire for a new method of directly detecting exoplanets. In addition to this, if the mechanism driving the planetary radio emission is due to interactions with the planet's intrinsic magnetic field, detection of exoplanetary radio emission would allow us to assess the strength of the planet's magnetic field (Zarka et al., 2001). This has consequences on the size of the planet's magnetosphere, which in turn can effect the lifetime of the planet's atmosphere. Whether this has a positive or negative effect is still in debate (Blackman & Tarduno, 2018; Carolan et al., 2019; Egan et al., 2019).

Despite many attempts, there have been no conclusive detections of exoplanetary radio emission to date (e.g. Lazio et al., 2010b; Sirothia et al., 2014; O'Gorman et al., 2018). Some possible explanations for this include the frequency range of the observations, the telescope sensitivity, the atmosphere of the planet (Weber et al., 2018; Daley-Yates & Stevens, 2018), and the emission not being beamed in the direction of the observer (Smith et al., 2009). Another possible explanation for this was made by Kavanagh et al. (2019), who illustrated that exoplanets can orbit through the radio photosphere of the winds of their host stars, a region where a large fraction of radio emission can be absorbed through free-free processes. As the radio photosphere is not spherically symmetric, when the planet orbits further into the wind of the host star more of its emission can be absorbed.

There have been hints of a decrease in the flux density at radio frequencies from transiting exoplanets near secondary transit. Smith et al. (2009) observed this in the case of hot Jupiter HD189733b. Similarly, observations of HAT-P-11b system by Lecavelier des Etangs et al. (2013) suggested a dip in the flux density near secondary transit. However, these results are inconclusive, and require follow-up observations with more sensitive instrumentation (Smith et al., 2009; Lecavelier des Etangs et al., 2013; Sirothia et al., 2014). If confirmed, these dips in flux density near secondary transit could be due to the stellar wind of the host star absorbing the emission from the planet, as suggested by Kavanagh et al. (2019).

A similar illustration of this phenomenon is the case of Black Widow pulsar systems (Roberts, 2011). These systems consist of a millisecond pulsar that is host to a low-mass companion with a mass of $\sim 0.01\ M_{\odot}$. As the companion nears primary transit of the pulsar host, radio emission originating from the pulsar is observed to disappear (see Polzin et al., 2019). This is believed to be due to the wind of the low-mass companion star eclipsing the pulsar. For example, Guillemot et al. (2019) observed eclipses of radio emission at 1.4 GHz from the Black Widow pulsar PSR J2055+3829. Due to the time variations of the eclipse, this has been attributed to the clumpy outflow of the companion star.

Radio eclipses have been observed in higher mass binaries as well. For example, Dougherty et al. (2005) observed a similar phenomenon in the massiv binary system WR140. From VLBA observations at 8.4 GHz they resolved that radio emission generated from the collision of the winds of the two star in the system disappears as the O-type star approaches periastron of the Wolf-Rayet star. This has been interpreted as the emission region entering the optically thick region of the wind of the Wolf-Rayet star.

In this paper, we present a model that predicts that radio emission from the planet becomes eclipsed by the wind of the host star as the planet progresses through its orbit. We illustrate how the properties of the wind of the host star and the planetary orbit affect the duration of the radio eclipse, and then apply our model to the τ Boo planetary system. We show how the model presented could be used to constrain properties such as the mass-loss rate and temperature of the stellar wind of the host star.

3.3 Radio eclipse of the planet by the stellar wind

To model the wind of the host star, we consider only forces due to the gravity of the star and the thermal pressure gradient of the wind (Parker, 1958):

$$\rho u \frac{d}{dr} u = -\frac{\rho G M_\star}{r^2} - \frac{d}{dr} p. \tag{3.1}$$

Here, ρ is the mass density, u is the velocity, r is the distance, G is the gravitational constant, $M_\star$ is the mass of the star, and p is the thermal pressure. Assuming that the stellar wind is isothermal and mass is conserved, Equation 3.1 can be re-arranged into the following form:

$$\frac{1}{u} \frac{d}{dr} u = \left(\frac{2a^2}{r} - \frac{G M_\star}{r^2} \right) \Big/ \left(u^2 - a^2 \right), \tag{3.2}$$

where a is the isothermal sound speed:

$$a = \sqrt{\frac{k_\mathrm{B} T}{\mu m_\mathrm{p}}}. \tag{3.3}$$

Here, k_B is Boltzmann's constant, T is the wind temperature, and μm_p is the mean mass per particle in the stellar wind, with m_p being the proton mass. For a fully ionised hydrogen wind, we take $\mu = 1/2$.

We solve Equation 3.2 enforcing a solution that passes through the critical point, where the numerator and denominator on the right-hand side go to zero simultaneously. This is to ensure a wind solution is obtained which monotonically increases in velocity outward (Parker, 1958). Such a critical point occurs at the sonic distance

$$r_\mathrm{c} = \frac{G M_\star}{2a^2}, \tag{3.4}$$

where the velocity of the wind at the critical point is $u = a$. Note that a physical solution is one where r_c is greater than the stellar radius. With that, we obtain the wind velocity profile for a given stellar mass $M_\star$ and wind temperature T. The mass-loss rate of the stellar wind is

$$\dot{M} = 4\pi r^2 \rho u. \tag{3.5}$$

So, for a given stellar mass, wind temperature and mass-loss rate, we obtain a mass number density profile of the stellar wind:

$$n = \frac{\dot{M}}{4\pi r^2 \mu m_\mathrm{p} u}. \tag{3.6}$$

One of the benefits of using a 1D isothermal stellar wind model is that it is much less time consuming than performing a 3D magnetohydrodynamic stellar wind simulation, such as those computed by Kavanagh et al. (2019). A limitation of isothermal stellar wind models is that they neglect the presence of a magnetic field, which is important for determining the angular momentum-loss rates and therefore the rotational evolution of low-mass stars (Weber & Davis, 1967; Réville et al., 2015; Johnstone et al., 2015; Ó Fionnagáin et al., 2019a). However, as we do not consider an evolving stellar wind here, we assume that an isothermal stellar wind model is sufficient for our purposes in this paper.

As the planet progresses further into its orbit, the amount of stellar wind material between the planet and observer increases. Since the wind of the host star can absorb low-frequency radio emission through free free processes (Panagia & Felli, 1975), a larger fraction of radio emission from the planet will be absorbed as it approaches an orbital phase of $\phi = 0.5$. We refer to a region of the stellar wind at a specific frequency as the 'radio photosphere', wherein only a certain fraction (i.e. 50%) of radio emission can escape through the wind. This is illustrated in the top panel of Figure 3.1. Note that there is one further complication: if the plasma frequency of the stellar wind at the planet's orbit

$$\nu_p = 9 \times 10^{-3} \sqrt{n_e} \text{ MHz} \tag{3.7}$$

is greater than the emitted frequency from the planet ν, no emission will generate. Here, n_e is the electron number density of the local stellar wind in cm^{-3}.

We do not model the emission mechanism of the planet here, but rather how such an emission, if existed, would be absorbed by the wind of the host star. We also assume that the emission from the planet is always beamed towards the observer. To determine how much planetary emission is absorbed by the stellar wind, we compute the optical depth at frequency ν at the planet's position x_p along the line of sight in the stellar wind (see Figure 3.1):

$$\tau_\nu = \int_{-\infty}^{x_\mathrm{p}} \alpha_\nu dx. \tag{3.8}$$

Here, α_ν is the free-free absorption coefficient (Cox, 2000):

$$\alpha_\nu = 3.692 \times 10^8 \left(1 - e^{-h\nu/k_\mathrm{B}T}\right) Z^2 g T^{-1/2} \upsilon^{-3} n_\mathrm{e} n_\mathrm{i}, \tag{3.9}$$

where h is Planck's constant, Z is the ionisation state (+1 for ionised hydrogen), and g is the Gaunt factor (Cox, 2000):

$$g = 10.6 + 1.9 \log_{10}(T) - 1.26 \log_{10}(Z\nu). \tag{3.10}$$

In Equation 3.9, n_e and n_i are the electron and ion number densities respectively. Since we treat the wind as being composed of fully ionised hydrogen, the total number density is $n = n_\mathrm{e} + n_\mathrm{i} = 2n_\mathrm{e}$ ($n_\mathrm{e} = n_\mathrm{i}$). The ion number density is the proton number density in this case.

The observer receives a specific intensity I_ν at frequency ν from the planet that has been attenuated by the stellar wind (Rybicki & Lightman, 1986):

$$I_\nu = I_{\nu,0} e^{-\tau_\nu}, \tag{3.11}$$

where $I_{\nu,0}$ is the emitted specific intensity by the planet. This is illustrated in the bottom panel of Figure 3.1. The flux density received by the observer is then:

$$F_\nu = \int I_\nu d\Omega = \frac{1}{d^2} \int I_\nu dA, \tag{3.12}$$

where $d\Omega$ is the element of solid angle of the emitting region, d is the distance to the system, and dA is the area element of the emitting region. Assuming that the specific intensity I_ν is constant through dA, then from Equations 3.11 and 3.12:

$$F_\nu \propto e^{-\tau_\nu}. \tag{3.13}$$

So, if $F_{\nu,0}$ is the flux density one would observe in the absence of a stellar wind, the observed flux density from the planet is:

$$F_\nu = F_{\nu,0} e^{-\tau_\nu}. \tag{3.14}$$

The term $e^{-\tau_\nu}$ therefore gives the fraction of the flux density that is transmitted from the planet to the observer. When computing the optical depth at each point in the planet's orbit with Equation 3.8, we extend the stellar wind out from the planet to a distance of 0.5 au in the direction of the observer ($-x$ direction). This distance is sufficient for the optical depth at the planet's position to converge.

Figure 3.2 illustrates how emission from a transiting planet orbiting its host star disappears as it approaches secondary transit. In this example, the planet orbits a star with a mass of 1 $M_\odot$ and radius of 1 $R_\odot$ at 0.02 au. The wind of the host star has a mass-loss rate of 100 $\dot{M}_\odot$, where $\dot{M}_\odot$ is the solar wind mass-loss rate (2×10^{-14} $M_\odot$ yr^{-1}), and a temperature of 2 MK. The left panel shows the combined thermal spectrum of the wind of the star with that of a planet at different orbital phases. We assume that the planet emits an unattenuated flux density of $F_{\nu,0} = 100$ μJy in the region of 20-40 MHz. The value of $F_{\nu,0}$ chosen here is purely for illustrative purposes. The thermal spectrum of the stellar wind is computed as per the method laid out in Ó Fionnagáin et al. (2019a) and Kavanagh et al. (2019). We compute the spectrum placing the system at 1 pc from the observer.

The right panel of Figure 3.2 shows the number density profile of the stellar wind which the planet orbits through. The orbital phases we compute the spectrum of the planet for in the left panel are marked along the orbit. As the planet progresses through its orbit towards secondary transit ($\phi \gtrsim 0.36$), the flux received from the planet begins to disappear. Past a certain point the wind of the host star eclipses the planet. Towards higher frequencies however, this effect is less pronounced. This was shown by Kavanagh et al. (2019), in that the planet is easier to detect both near primary transit of the host star and at higher emitted frequencies.

3.4 Stellar wind effects on radio eclipses

Here, we investigate how the properties of the stellar wind itself affect how much planetary emission escapes through the wind. Figure 3.3 shows how varying the

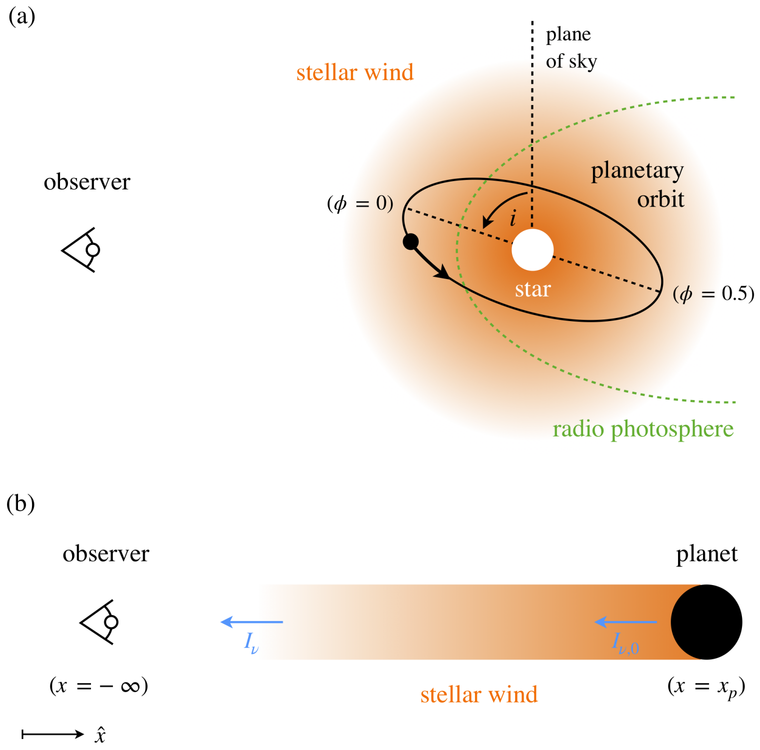

Figure 3.1: *Top*: Sketch illustrating a planet that orbits in a circle through the wind of its host star, inclined at an angle i from the plane of the sky. Orbital phases of $\phi = 0$ and $\phi = 0.5$, corresponding to when the planet is nearest and furthest from the observer respectively, are marked along the orbit. The radio photosphere of the stellar wind is also shown, which the planet orbits through for a fraction of its orbit. *Bottom*: The line of sight radio emission originating from the planet takes through the stellar wind towards the observer. The planet emits a specific intensity of $I_{\nu,0}$, and the observer sees an attenuated specific intensity of $I_\nu = I_{\nu,0} e^{-\tau_\nu}$.

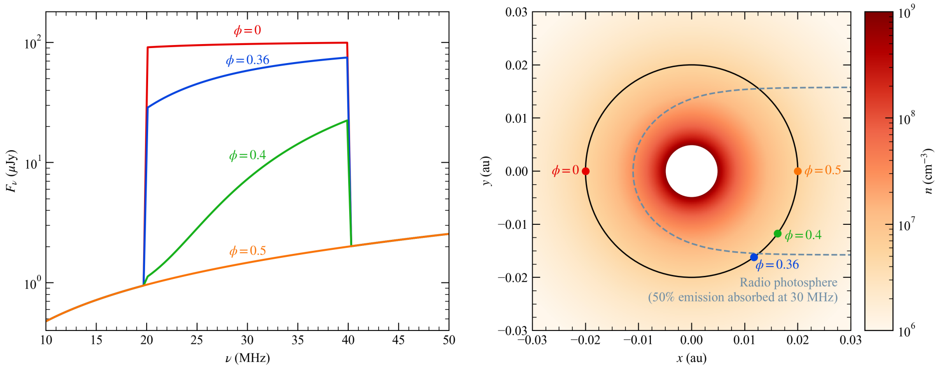

Figure 3.2: *Left:* The combined spectrum of free-free emission from the stellar wind and emission from the planet at different orbital phases. The system is placed at 1 pc for this illustration, with the planet emitting an arbitrary unattenuated flux density of 100 μJy. *Right:* Number density profile of the stellar wind, and the positions of the planet corresponding to the spectra shown in the left panel. The dashed line shows the radio photosphere where 50% of emission is absorbed at 30 MHz by the stellar wind. The observer looks towards the system from $x = -1$ pc along the x-direction.

mass-loss rate of the wind of the host star affects the percentage of escaping emission at 30 MHz as the planet progresses through its orbit. As the planet approaches secondary transit of the star (orbital phase of 0.5), the planetary emission becomes eclipsed by the stellar wind. This effect is more pronounced for higher stellar wind mass-loss rates, which in turn are denser for a fixed temperature. Note that at 30 MHz, a low mass-loss rate stellar wind does not attenuate the planetary emission at primary transit ($\phi = 0$). However at higher mass-loss rates, even when the planet transits part of its emission is attenuated and the flux density would not be observed at this frequency.

In Figure 3.4 we show varying how the temperature of the stellar wind, for a fixed mass-loss rate, affects the amount of escaping emission from the planet. We see that detection of exoplanetary radio emission is favoured for high temperature winds, with the eclipse occurring for a smaller fraction of the planet's orbit. As the wind is accelerated much faster in at higher temperatures, the density of the wind drops off much faster (following from Equation 3.6). As a result, hotter winds tend to be less dense. However, the mass-loss rates of low-mass stars are expected to increase with surface X-ray flux (see Wood, 2018), which in turn is correlated with a hot corona (Johnstone & Güdel, 2015). So while the most favourable detection scenario would be a planet that orbits a star with a hot wind with a low mass-loss rate, it is more likely that if the wind is very hot, the mass-loss rate is high. In general, planets orbiting stars with low density winds are more favourable for detection.

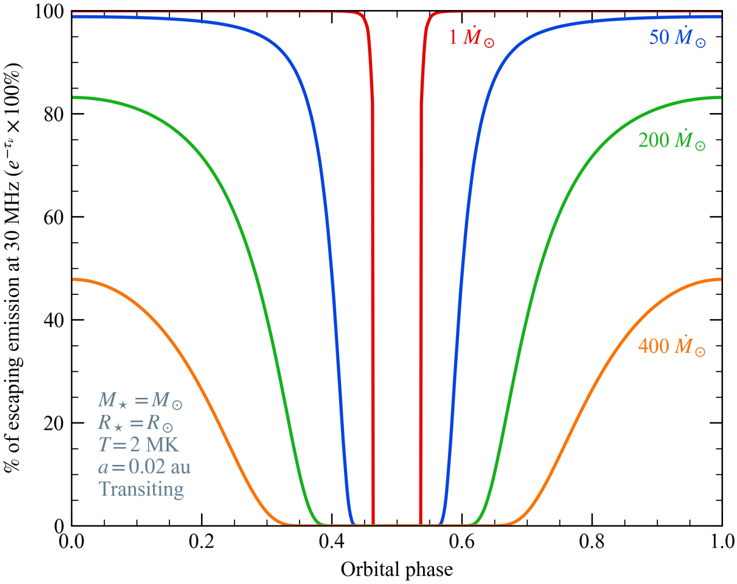

Figure 3.3: The percentage of planetary emission at 30 MHz ($e^{-\tau_\nu} \times 100\%$) that escapes through the stellar wind as a function of orbital phase for different stellar wind mass-loss rates. The stellar, wind, and orbital parameters are listed in the bottom left corner. When $\sim 0\%$ of the emission escapes, the planet is considered to be in 'radio eclipse'. Note that the fraction of the orbit during radio eclipse is larger for winds of higher mass-loss rates.

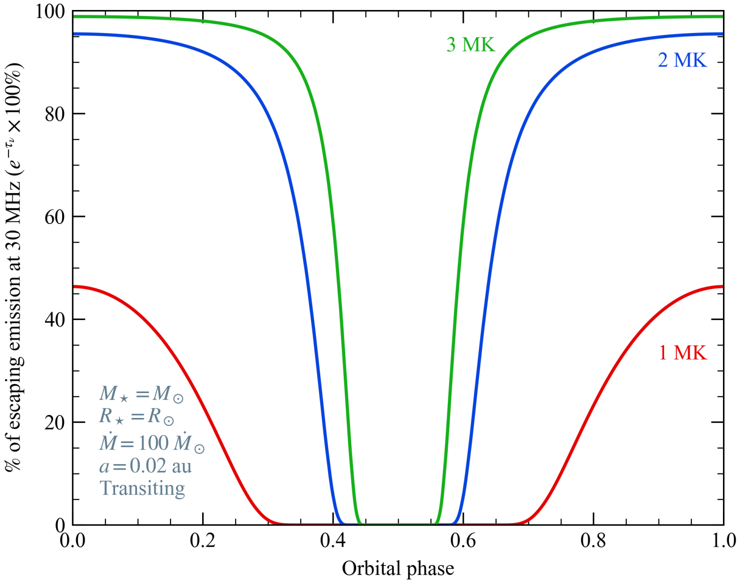

Figure 3.4: Same as Figure 3.3, but for different stellar wind temperatures.

3.5 Orbital effects on radio eclipses

The amount of planetary emission that escapes the wind of the host star also depends on the path it takes as the planet progresses through its orbit. Here, we investigate how the geometry of the orbit affects the duration of the radio eclipses. In Figure 3.5 we show the effects of varying the orbital inclination of the planet. We find that a transiting planet is the most easily detectable, specifically near primary transit ($\phi = 0$). However, in this configuration the planetary emission also is the most attenuated, near secondary transit ($\phi = 0.5$), with the largest amplitude of the eclipse modulation.

The transmitted flux density on the other hand for a planet in a plane of sky orbital configuration is constant, assuming the unattenuated flux density $F_{\nu,0}$ is constant. As a result, a planet orbiting in the plane of the sky will either always be detectable or never be detectable, depending on the instrument sensitivity and the amount of flux that escapes the stellar wind. Detection is also in theory always possible for planets orbiting at inclinations $0 < i < \cos^{-1}(a/R_\star)$, as the planet does not pass behind the stellar disk.

Figure 3.6 show the effects of varying the orbital distance of a transiting planet on the amount of escaping emission. We see that the closer in to the star the planet orbits, the lower the amount of emission escapes as the density of the stellar wind is much larger close in. In addition to this, if the stellar wind plasma frequency is too high the emission will not generate. This is the case for a planet orbiting at 0.01 au for the parameters presented in Figure 3.6. So, planets orbiting further

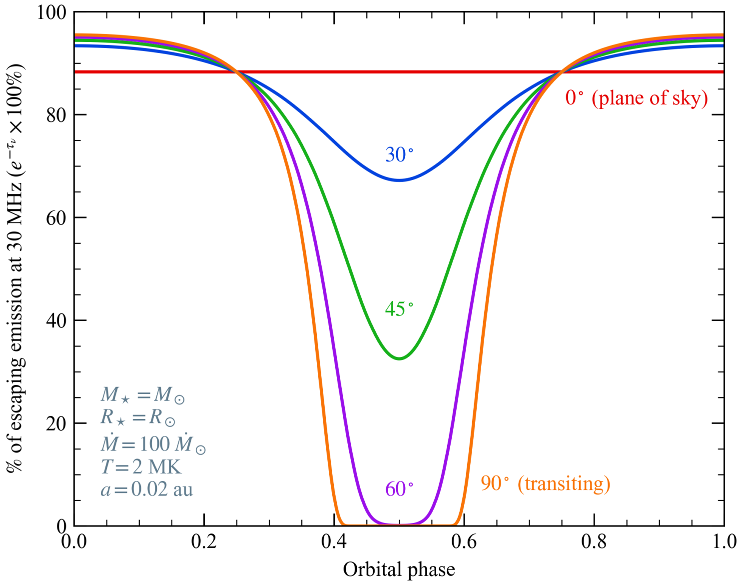

Figure 3.5: Same as Figure 3.3, but for different orbital inclinations. Transiting planets have the most favourable conditions for detection, but also have the largest modulation of their emitted flux density.

out are more easily detectable. However, if the stellar wind power dissipated onto the planetary magnetosphere powers the planetary radio emission, planets further out are likely to emit much lower flux densities than those closer in (Zarka et al., 2001).

3.6 Constraining the stellar wind properties of the hot Jupiter host τ Boo

We now focus on the τ Boo planetary system, which lies 15.6 pc away from Earth. The star is host to the supermassive hot Jupiter τ Boo b which orbits at just 0.046 au, and as a result the planet is expected to be a source of strong radio emission (see Weber et al., 2018). As the planet does not transit its host star ($i = 45°$), in theory it could be detectable for the entirety of its orbit if it emits a high enough flux density, following the results shown in Figure 3.5. The mass and radius of the star are 1.30 $M_\odot$ and 1.33 $R_\odot$ respectively. All parameters listed above are taken from `exoplanet.eu`.

As illustrated in Figures 3.3 and 3.4, the amount of escaping emission from the planet depends on the mass-loss rate and temperature of the wind of the host star, both of which are unknowns in the case of τ Boo. Another two unknown quantities of the system are the emitted flux density and frequency from the planet (if it is indeed a source of exoplanetary radio emission). Turner et al. (2019) showed that

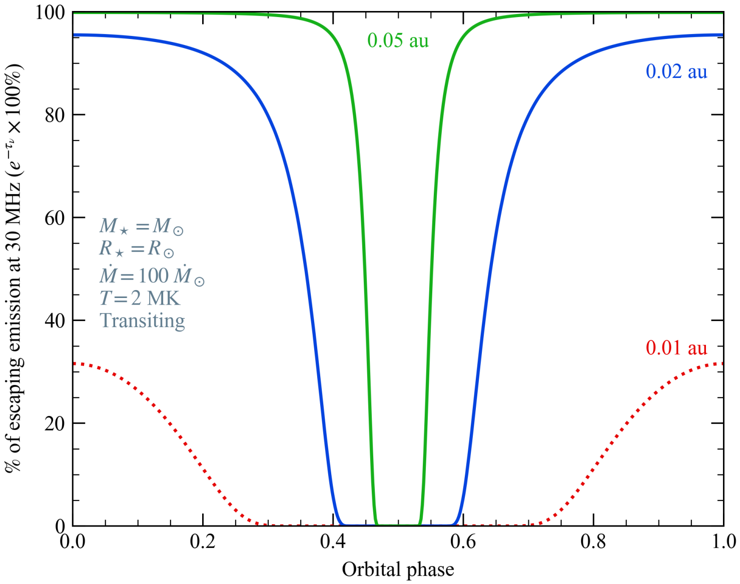

Figure 3.6: Same as Figure 3.3, but for different orbital distances. At 0.01 au, the plasma frequency of the stellar wind at the planet's is greater than 30 MHz and as a result no emission can generate. This is indicated by the dashed line.

emission from τ Boo b would be detectable with LOFAR, if it emits a flux density that is 10^5 times larger than that emitted by Jupiter. During active periods, Jupiter has an observed flux density 10^7 Jy at a distance of 1 au (Zarka et al., 2004). Therefore, at a distance of 15.6 pc, we assume an unattenuated flux density for τ Boo b of $F_{\nu,0} = 96.6$ mJy.

If we also assume that the planet emits at a frequency of 30 MHz, we can determine for what fraction of the planet's orbit it would be detectable with LOFAR. At 30 MHz LOFAR has a sensitivity of $F_\nu^{\rm LOFAR} \sim 7$ mJy for a 1 hour integration time (see Figure 1 of Grießmeier et al., 2011). The planet is then detectable when $F_\nu > F_\nu^{\rm LOFAR}$ or when $e^{-\tau_\nu} > 0.0725$ following Equation 3.14.

Figure 3.7 shows the combination of stellar wind mass-loss rate and temperature that results in detection of emission from τ Boo b at 30 MHz with LOFAR for 25%, 50%, and 75% of its orbit. As can be seen, if emission was detected from the system at 30 MHz for, say, 50% of the planet's orbit, there is a degeneracy between the stellar wind mass-loss rate and temperature. So while observing radio emission alone from the planet for a certain fraction of its orbit does not provide enough information to derive the stellar wind properties, it could nevertheless be used in conjunction with the radiometric Bode's law to provide additional constraints (see Vidotto & Donati, 2017). In Figure 3.7 we also show that the plasma frequency of the stellar wind at the planet's orbit and the maximum temperature of the stellar wind can constrain the parameters of the stellar wind. We derive a maximum coronal temperature (and therefore the wind) for τ Boo of 3.7 MK from

Johnstone & Güdel (2015), using the maximum observed X-ray luminosity for the host star of 8×10^{28} erg s^{-1} (Mittag et al., 2017).

The mass-loss rates of the winds of low-mass stars have proved to be very difficult to measure, and has only been possible in a handful of cases. One such method relies on observations of the absorption of Ly-α from the star due to the build-up of neutral hydrogen at the astrosphere (Wood, 2004). Vidotto & Bourrier (2017) also illustrated how stellar wind mass-loss rates could be derived based on observations of Ly-α absorption due to the presence of an extended planetary atmosphere. Both of these methods however require Hubble Space Telescope observations, and therefore cannot be carried out for a large number of targets. More recently, Jardine & Collier Cameron (2019) showed how the mass-loss rates of low-mass stars could be derived based on the presence of prominences from Hα observations. This method however is only possible for very fast rotators. Mass-loss rates from low-mass stars could also be determined from observations of thermal free-free radio emission from the stellar wind itself (Güdel, 2002), however current radio telescopes are not sensitive enough to detect this emission (Ó Fionnagáin et al., 2019a). Our method presented here could provide a new method of constraining the mass-loss rates of low-mass stars from radio observations with current telescopes (i.e., LOFAR), if combined with another method such as the radiometric Bode's law.

One of the main issues with the application of our model in this section is that in order to determine when a planet would be detectable with a given radio telescopes, we require knowledge of the unattenuated flux density emitted by the planet. In addition to this, it is likely that the emitted flux density varies over the orbit. This has been shown to be the case if the emission mechanism powering the planetary radio emission is the interaction between the stellar wind and planetary magnetosphere, as the wind of the host star is not uniform (see Figure 4 of Kavanagh et al., 2019; Nicholson et al., 2016). For instance, Jupiter is observed to experience active periods where the flux density emitted increases (Zarka et al., 2004).

3.7 Conclusions

In this work, we have presented how the properties of the stellar wind and the orbital characteristics of a planet affect the fraction of the planet's orbit where its radio emission is eclipsed by the wind of the host star. We have illustrated that detection of planetary radio emission is favoured for host stars with low density winds. The ideal case for this would be a star with a hot wind and low-mass loss rate, however low-mass stars with hot winds generally have high mass-loss rates.

In terms of orbital parameters, emission can most easily escape the wind of the host star for transiting planets, specifically in the region near primary transit. However, in this orbital configuration, the emission is also most attenuated near secondary transit. Therefore, transiting exoplanets offer the most extreme case in which radiation escapes the most ($\phi = 0$) or is most attenuated ($\phi = 0.5$). Planets with orbital inclinations in the range $0 < i < \cos^{-1}(a/R_\star)$ can in theory always be

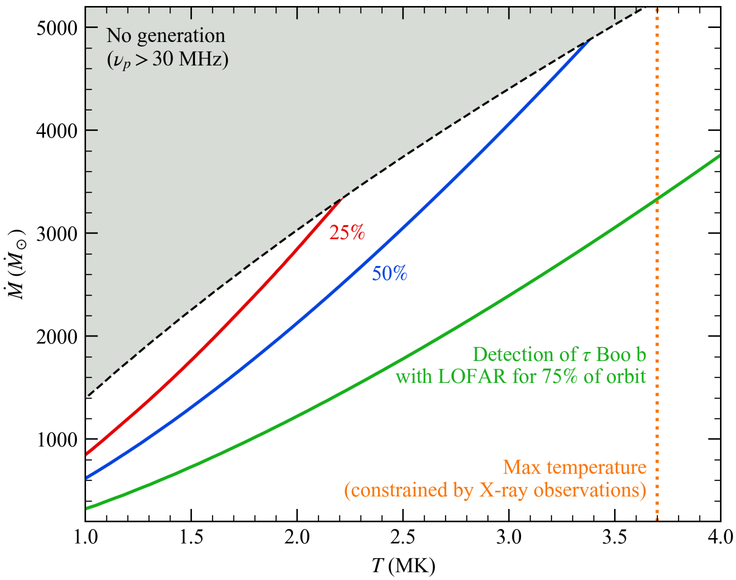

Figure 3.7: The combined stellar wind mass-loss rate and temperature that results in detection of radio emission from τ Boo b at 30 MHz with LOFAR, for 25%, 50%, and 75% of its orbit. The shaded area illustrates where the plasma frequency of the stellar wind at the planet's orbit is too high for generation of radio emission at 30 MHz. The vertical dotted line marks the maximum temperature of the stellar wind, which is constrained by X-ray observations of the host star (see relevant text).

detected, depending on the emitted flux density and density of the stellar wind, as they do not pass behind the stellar disk. We also have illustrated that planets orbiting closer to their host stars are less likely to be detected, as the stellar wind is very dense close in. However, if the planet orbits far out from its host star, the mechanism powering the radio emission of the planet may be too weak (see Zarka et al., 2001).

We applied our model to the τ Boo planetary system, and illustrated that if radio emission is detected from the planet for a certain percentage of the orbit with LOFAR, we can constrain the wind properties of the host star. Observations such as this are not sufficient to disentangle the mass-loss rate and temperature of the wind. In combination with another method however such as the radiometric Bode's law could help to further constrain the stellar wind properties. The plasma frequency of the stellar wind as well as X-ray observations of the host star could also aid constraining the wind properties.

Acknowledgements

RDK acknowledges funding received from the Irish Research Council through the Government of Ireland Postgraduate Scholarship Programme. AAV acknowledges funding from the Irish Research Council Consolidator Laureate Award 2018 and the European Research Council (ERC) under the European Union's Horizon 2020 research and innovation programme (grant agreement No 817540, ASTROFLOW).

4 | Planet-induced radio emission from the coronae of M dwarfs

4.1 Abstract

There have recently been detections of radio emission from low-mass stars, some of which are indicative of star-planet interactions. Motivated by these exciting new results, in this paper we present Alfvén wave-driven stellar wind models of the two active planet-hosting M dwarfs Prox Cen and AU Mic. Our models incorporate large-scale photospheric magnetic field maps reconstructed using the Zeeman-Doppler Imaging method. We obtain a mass-loss rate of 0.25 $\dot{M}_\odot$ for the wind of Prox Cen. For the young dwarf AU Mic, we explore two cases: a low and high mass-loss rate. Depending on the properties of the Alfvén waves which heat the corona in our wind models, we obtain mass-loss rates of 27 and 590 $\dot{M}_\odot$ for AU Mic. We use our stellar wind models to assess the generation of electron cyclotron maser instability emission in both systems, through a mechanism analogous to the sub-Alfvénic Jupiter-Io interaction. For Prox Cen we do not find any feasible scenario where the planet can induce radio emission in the star's corona, as the planet orbits too far from the star in the super-Alfvénic regime. However, in the case that AU Mic has a stellar wind mass-loss rate of 27 $\dot{M}_\odot$, we find that both planets b and c in the system can induce radio emission from $\sim$ 10 MHz – 3 GHz in the corona of the host star for the majority of their orbits, with peak flux densities of $\sim$ 10 mJy. Detection of such radio emission would allow us to place an upper limit on the mass-loss rate of the star.

4.2 Introduction

Many theoretical works have aimed to identify potential targets for the detection of exoplanetary radio emission (Grießmeier et al., 2007; Vidotto et al., 2015; Vidotto & Donati, 2017; Kavanagh et al., 2019). A model that is commonly used to estimate the generation of radio emission from exoplanets is the radiometric Bode's law, which extrapolates the observed relation between the radio power emitted from the magnetised solar system objects and the incident solar wind power (Zarka, 2007). In this model, the interaction between the planet's magnetosphere and the magnetised stellar wind of its host star leads to reconnection in the planet's magnetotail. This reconnection then accelerates electrons towards the planet's poles, creating emission through the electron cyclotron maser instability (ECMI).

In these works, hot Jupiters have often been selected as suitable candidates for radio detection. As they are exposed to harsh stellar wind conditions due to their proximity to their host stars (Vidotto et al., 2015), they are expected to produce much higher radio powers than those observed in the solar system (Zarka et al., 2001). This emission can only be generated if hot Jupiters are magnetised. Given that the emission mechanism is ECMI, it occurs at the cyclotron frequency $\nu = 2.8\ B$ MHz, where B is the magnetic field strength in gauss (G). Zaghoo & Collins (2018) estimated that hot Jupiters could harbour magnetic fields with strengths of 1 – 10 G. In this range, these field strengths would correspond to radio emission from 2.8 – 28 MHz.

Despite hot Jupiters being seemingly favourable sources of detectable low frequency radio emission, many radio surveys of these systems have found little evidence of such emission (Smith et al., 2009; Lazio et al., 2010a; Lecavelier des Etangs et al., 2013; de Gasperin et al., 2020; Narang et al., 2021). Numerous explanations have been proposed for the lack of detections, such as a mismatch between the emitted and observation frequency (Bastian et al., 2000), the emission being beamed out of our line of sight (Smith et al., 2009), and absorption of the emission by the stellar wind of the host star (Vidotto & Donati, 2017; Kavanagh et al., 2019; Kavanagh & Vidotto, 2020). Intriguingly, Turner et al. (2021) recently detected radio emission at $\sim$ 30 MHz from the hot Jupiter host τ Boo. They suggest that this emission could be indicative of ECMI generated in the orbiting planet's magnetic field. Follow-up observations will be required however in order to investigate this further.

An alternative unipolar model for the generation of radio emission via ECMI in exoplanetary systems has also been proposed, analogous to the sub-Alfvénic interaction between Jupiter and its moon Io (Neubauer, 1980; Zarka, 1998; Saur et al., 2004; Zarka, 2007; Grießmeier et al., 2007). In this model, the host star and planet take the roles of Jupiter and Io respectively. If the planet orbits with a sub-Alfvénic velocity relative to the wind of its host star, it can generate Alfvén waves that travel back towards the star (Ip et al., 2004; McIvor et al., 2006; Lanza, 2012; Turnpenney et al., 2018; Strugarek et al., 2019; Vedantham et al., 2020). A fraction of the wave energy produced in this interaction is expected to dissipate and produce radio emission via ECMI in the corona of the host star (Turnpenney et al., 2018).

Due to the increasing sensitivity of radio telescopes such as LOFAR, M dwarfs are beginning to light up the radio sky at low frequencies (Callingham et al., 2021). One such system is the quiescent M dwarf GJ 1151, which was recently detected to be a source of 120 – 160 MHz emission by Vedantham et al. (2020). The authors illustrated that the observed emission is consistent with ECMI from the star induced by an Earth-sized planet orbiting in the sub-Alfvénic regime with a period of 1 – 5 days. Prior to this detection, there had been no evidence to suggest GJ 1151 is host to a planet. There has been some discussion in the literature recently about the existence of such a planet. Mahadevan et al. (2021) have suggested that a planet orbits the star in a 2-day orbit, whereas Perger et al.

(2021) have ruled this out, placing a mass upper limit of 1.2 Earth on a planet in a 5-day orbit. Follow-up observations of the system will be needed to further assess if the radio emission is of a planet-induced origin.

M dwarfs typically exhibit strong magnetic fields, with maximum large-scale strengths ranging from ~ 100 G – 1 kG (Donati et al., 2008b; Morin et al., 2010; Shulyak et al., 2019). If an M dwarf is host to a planet that orbits in the sub-Alfvénic regime, the planet could induce radio emission from the star's corona via ECMI at frequencies up to 280 MHz – 2.8 GHz. Planet-induced emission from M dwarfs therefore could be distinguished from emission predicted with the radiometric Bode's law, due to the different frequency ranges.

The M dwarf Proxima Centauri (Prox Cen) is our closest stellar neighbour, which also hosts a planet that is expected to be Earth-sized (Anglada-Escudé et al., 2016). Naturally, being so close to us we want to understand both the habitability of the orbiting planet and the system's potential for producing planet-induced radio emission. An important step in answering this question is to assess the stellar wind environment around the planet. Prox Cen is expected to have a relatively weak stellar wind, with a mass-loss rate of $\dot{M} < 0.2\ \dot{M}_\odot$ (Wood et al., 2001), where $\dot{M}_\odot = 2 \times 10^{-14}\ M_\odot\ \mathrm{yr}^{-1}$ is the solar wind mass-loss rate. The star also possesses a strong large-scale surface magnetic field of ~ 200 G (Klein et al., 2021a). Its proximity to Earth along with its potentially habitable planet make it an interesting system to search for planet-induced radio emission.

AU Microscopii (AU Mic) is a young M dwarf which also shows potential for detecting planet-induced radio emission. It lies just under 10 pc away from Earth, and has recently been discovered to host two Neptune-sized close-in planets (Plavchan et al., 2020; Martioli et al., 2021). We list the properties of the AU Mic system along with those for Prox Cen in Table 4.1. While planets b and c orbiting AU Mic are not likely to be habitable, their proximity to the host star makes them ideal candidates for inducing radio emission in the corona of the host star. The stellar wind mass-loss rate of AU Mic is relatively unconstrained. Models of interactions between the stellar wind and debris disk in the system estimate a mass-loss rate from 10 $\dot{M}_\odot$ (Plavchan et al., 2009) up to 1000 $\dot{M}_\odot$ (Chiang & Fung, 2017). Its large-scale surface magnetic field is also quite strong, with a strength of ~ 500 G (Klein et al., 2021b). The two close-in planets along with the star's strong magnetic field make it a very suitable candidate for planet-induced radio emission.

In this paper, we use the magnetic field maps reconstructed by Klein et al. (2021a) and Klein et al. (2021b) to model the stellar winds of the two M dwarfs Prox Cen and AU Mic respectively. We use our 3D Alfvén wave-driven stellar wind models to investigate if the orbiting planets can induce the generation of ECMI emission in the coronae of their host stars. We then illustrate how the detection of planet-induced radio emission can be used to constrain properties of the wind of the host star.

Table 4.1: Stellar and planetary parameters for the Prox Cen and AU Mic systems. The superscript after each value denotes its reference, which are listed at the bottom of the table.

Parameter	Prox Cen	AU Mic	
Stellar mass ($M_\star$)	0.12 $M_\odot$[1]	0.50 $M_\odot$[2]	
Stellar radius ($R_\star$)	0.14 $R_\odot$[1]	0.75 $R_\odot$[2]	
Stellar wind mass-loss rate ($\dot{M}$)	$<$ 0.2 $\dot{M}_\odot$[3]	10 $\dot{M}_\odot$[4], 1000 $\dot{M}_\odot$[5]	
Average surface stellar magnetic field strength	200 G[6]	500 G[7]	
Spectral type	M5.5V[1]	M1V[8]	
Stellar rotation period	83 days[1]	4.86 days[2]	
Distance (d)	1.30 pc[1]	9.79 pc[2]	
	Planet b	Planet b	Planet c
Planetary mass (M_p)	$>$ 1.27 $M_\oplus$[1]	1.00 M_Nep[9]	1.7 – 27.7 $M_\oplus$[9]
Planetary radius (R_p)	–	1.13 R_Nep[9]	0.91 R_Nep[9]
Planetary orbital distance (a)	74.0 $R_\star$[1]	18.5 $R_\star$[9]	26.9 $R_\star$[9]
Planetary orbital period	11.2 days[1]	8.46 days[9]	18.9 days[9]

1: Anglada-Escudé et al. (2016); 2: Plavchan et al. (2020); 3: Wood et al. (2001); 4: Plavchan et al. (2009); 5: Chiang & Fung (2017); 6: Klein et al. (2021a); 7: Klein et al. (2021b); 8: Martioli et al. (2020); 9: Martioli et al. (2021)

4.3 Modelling the winds of M-dwarfs

To model the stellar winds of Prox Cen and AU Mic we use the Alfvén wave solar model (AWSoM, van der Holst et al., 2014) implemented in the 3D magnetohydrodynamic (MHD) code BATS-R-US (Powell et al., 1999), which is part of the Space Weather Modelling Framework (Tóth et al., 2012). In the AWSoM model, Alfvén waves are injected at the base of the chromosphere where they propagate, reflect, and dissipate. The dissipation of the Alfvén waves heats the corona, which in turn drives the stellar wind outflow. The AWSoM model has been validated against observations of the solar corona (van der Holst et al., 2014; Jin et al., 2017), and has also been applied to study the stellar wind environments of other systems (see Garraffo et al., 2017; Boro Saikia et al., 2020; Alvarado-Gómez et al., 2020; Ó Fionnagáin et al., 2021).

In our models, we set boundary conditions for the radial magnetic field, Alfvén wave flux, plasma density and temperature at the base of the chromosphere. For the magnetic field we use maximum-entropy maps reconstructed from spectropolarimetric observations for the two stars by Klein et al. (2021a) and Klein et al. (2021b) via the Zeeman-Doppler Imaging method (Donati & Landstreet, 2009). These are shown in Figure 4.1. The input for the Alfvén wave flux in our model is given in units of flux per unit magnetic field strength S_A/B. We refer to this as the 'Alfvén wave flux-to-magnetic field ratio', for which we adopt a variety of values (see Section 4.4). We fix the density and temperature at the base of the chromosphere as 2×10^{10} cm^{-3} and 5×10^{4} K respectively in our models, the same as chosen by Alvarado-Gómez et al. (2020). These values are also typically used

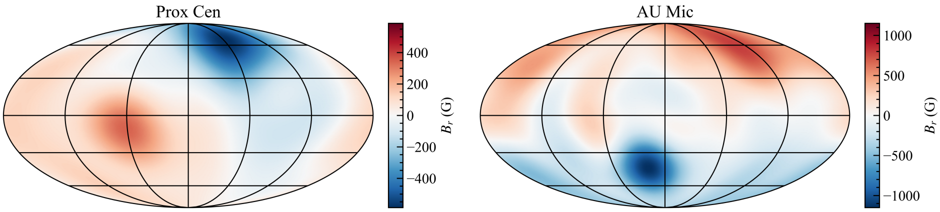

Figure 4.1: Radial photospheric magnetic field of Prox Cen (left) and AU Mic (right), reconstructed by Klein et al. (2021a) and Klein et al. (2021b) respectively. We implement these maps at the inner boundary of our stellar wind simulations for the two stars.

for the Sun (see Sokolov et al., 2013).

The corona is heated through a turbulent energy cascade in our model, which is produced by the reflection and dissipation of Alfvén waves in the local plasma environment. The wave dissipation rate depends on the transverse correlation length $L_\perp$, which in turn is proportional to $B^{-1/2}$ (Hollweg, 1986). In our model the transverse correlation length is given in terms of the proportionality constant $L_\perp\sqrt{B}$. We adopt the default value of $L_\perp\sqrt{B} = 1.5 \times 10^9$ cm $\sqrt{\mathrm{G}}$ for this (van der Holst et al., 2014). We also include both collisional and collisionless heat conduction, radiative cooling, and stochastic heating in our models, as described in van der Holst et al. (2014). We fix the adiabatic index to be 5/3.

Our computational grid is spherical and extends from the base of the chromosphere to 100 times the stellar radius $R_\star$. The maximum resolution in our grid is $\sim 5 \times 10^{-4}$ $R_\star$. We also adaptively-resolve current sheet regions in our grid. The number of cells in our grid is $\sim$ 6 million. We iteratively solve the MHD equations until the model reaches a steady state. We take this to be when the mass-loss rate, open magnetic flux, and angular momentum-loss rate of the wind vary by less than 10 percent between iterations.

4.4 Stellar wind environments of the M-dwarfs

4.4.1 Prox Cen

Using an Alfvén wave flux-to-magnetic field ratio of $S_\mathrm{A}/B = 5 \times 10^4$ erg s^{-1} cm^{-2} G^{-1}, we obtain a stellar wind with a mass-loss rate of $\dot{M} = 0.25$ $\dot{M}_\odot$ for Prox Cen. This is in agreement with the upper limit obtained by Wood et al. (2001). The rest of the free parameters in the model are as described in Section 4.3. Our calculated mass-loss rate is also in line with other published works on the wind of Prox Cen, which used proxies for the surface magnetic field (Garraffo et al., 2016; Alvarado-Gómez et al., 2020).

Figure 4.2 shows a 3D view of the simulated wind for Prox Cen. We see that the planet orbits in a super-Alfvénic regime for the entirety of its orbit. Therefore, we do not expect any unipolar planet-induced radio emission from Prox Cen during the epoch of the observations from which the magnetic field map was reconstructed

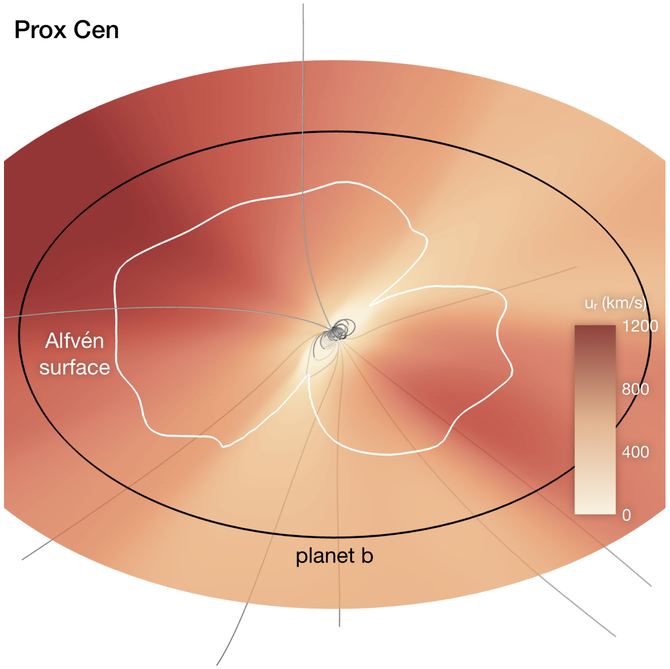

Figure 4.2: Simulated stellar wind of Prox Cen. The grey lines illustrate the large-scale magnetic field of the star which is embedded in the wind. The orbit of Prox Cen b is shown as a black circle, and the white line corresponds to where the Alfvén Mach number $M_{\rm A} = 1$ (see Equation 4.1). The contour in the orbital plane is coloured by the wind radial velocity (u_r).

(April - July 2017, Klein et al., 2021a). Note that we assume that the orbital plane of the planet is perpendicular to the rotation axis of the star.

4.4.2 AU Mic

To investigate the two estimated mass-loss rates for AU Mic, we use two different values for the Alfvén wave flux-to-magnetic field ratio. Again, the values used for the rest of the free parameters in the model are given in Section 4.3. For a value of $S_{\rm A}/B = 1.1 \times 10^5$ erg s^{-1} cm^{-2} G^{-1} (Sokolov et al., 2013), we obtain a stellar wind mass-loss rate of 27 $\dot{M}_\odot$ for AU Mic. We refer to this as the 'Low $\dot{M}$' model for the star. Increasing the Alfvén wave flux-to-magnetic field ratio to $S_{\rm A}/B = 6 \times 10^6$ erg s^{-1} cm^{-2} G^{-1}, we find that the mass-loss rate increases to a value of 590 $\dot{M}_\odot$. We refer to this as the 'High $\dot{M}$' model. Figure 4.3 shows a 3D view of both stellar wind models for AU Mic. We take both planets to orbit perpendicular to the stellar rotation axis, as both planets transit the star with orbital inclinations of $\sim 90°$ (Martioli et al., 2021), with the orbit of planet b being aligned with the rotation axis of the star (Martioli et al., 2020).

In the case of the Low $\dot{M}$ model (left panel of Figure 4.3), we find that both planets b and c orbit in the sub-Alfvénic regime for the majority of their orbit. This means that the two planets could induce the generation of radio emission along the lines connecting the planet to the star (Turnpenney et al., 2018; Vedantham et al., 2020). For the High $\dot{M}$ model however, both planets are in the super-Alfvénic regime for their entire orbit (right panel of Figure 4.3), as the wind is much denser than the Low $\dot{M}$ model. As a result, we do not expect planet-induced radio emission from AU Mic in the case that it has a high mass-loss rate.

We now estimate the maximum mass-loss rate for AU Mic at which the planets can induce radio emission. Using a least-squares method, we fit our data with a power law between the mass-loss rate and maximum size of the Alfvén surface in the orbital plane $R_\text{A, orb}^\text{max}$. For our data, we obtain a fit of $\dot{M} = 9.6 \times 10^5 (R_\text{A, orb}^\text{max})^{-2.6}\ \dot{M}_\odot$, where $R_\text{A, orb}^\text{max}$ is in stellar radii. For both planets to be in sub-Alfvénic orbits at least partially, the maximum size of the Alfvén surface must be greater than the orbital distance of planet c. Substituting this orbital distance of 26.9 $R_\star$ into our power law fit to our data, we find that AU Mic would need to have a mass-loss rate of $\lesssim 190\ \dot{M}_\odot$ in order for planet-induced radio emission to be generated in its corona. Detection of such emission would therefore allow us to place an upper limit of $\lesssim 190\ \dot{M}_\odot$ on the mass-loss rate of AU Mic. Note that in either case, radio emission could still be generated from the planet's own magnetosphere (see Vidotto & Donati, 2017; Kavanagh et al., 2019; Kavanagh & Vidotto, 2020). We explore the scenario for the generation of planet-induced radio emission in AU Mic's corona further in Section 4.5.1.

4.5 Planet-induced radio emission

4.5.1 AU Mic

Here, we describe our model we use to estimate the radio emission induced in the corona of AU Mic by planets b and c, in the scenario where the star has a mass-loss rate of $\lesssim 190\ \dot{M}_\odot$. We use our Low $\dot{M}$ model data in our calculations. A planet is said to be in the sub-Alfvénic regime when the Alfvén Mach number is less than 1:

$$M_\text{A} = \frac{\Delta u}{u_\text{A}} < 1. \tag{4.1}$$

Here, Δu is the relative velocity between the stellar wind velocity u and planet orbital velocity u_p:

$$\boldsymbol{\Delta u} = \boldsymbol{u} - \boldsymbol{u}_\text{p}. \tag{4.2}$$

The orbital velocity of the planet is $\boldsymbol{u}_\text{p} = \sqrt{GM_\star/a}\ \hat{\boldsymbol{\phi}}$, where G is the gravitational constant, $M_\star$ is the stellar mass, a is the orbital distance, and $\hat{\boldsymbol{\phi}}$ is the azimuthal angle. In equation 4.1, u_A is the Alfvén velocity of the stellar wind at the planet:

$$u_\text{A} = \frac{B}{\sqrt{4\pi\rho}}, \tag{4.3}$$

where B and ρ are the stellar wind magnetic field strength and density respectively.

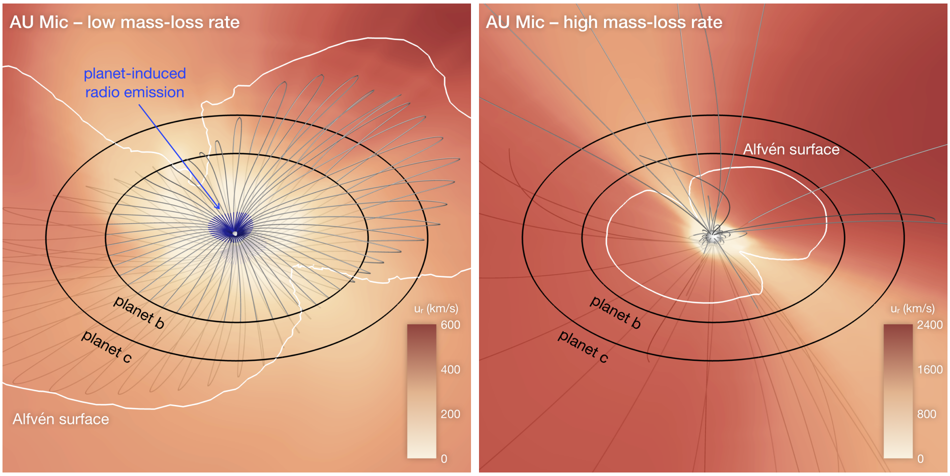

Figure 4.3: *Left*: Low $\dot{M}$ model of the stellar wind of AU Mic. The orbits of planets b and c are shown as black circles, and the white line corresponds to where the Alfvén Mach number $M_\mathrm{A} = 1$ (see Equation 4.1). The contour in the orbital plane is coloured by the wind radial velocity (u_r). The grey lines show the stellar magnetic field lines that connect to the orbit of planet b. Each of these lines is a closed loop, and connects back to the star in both the Northern and Southern hemisphere. The blue shaded region of each line illustrates where planet b can induce the generation of radio emission via ECMI (see Equation 4.6). Note that planet c can also induce generation, but for clarity we omit these field lines. *Right*: High $\dot{M}$ model for AU Mic. Both planets b and c orbit in the super-Alfvénic regime in this scenario. Note that the magnetic field lines shown here do not connect to the orbit of either planet.

The power of the Alfvén waves produced by a planet orbiting in the sub-Alfvénic regime is (Saur et al., 2013):

$$P = \pi^{1/2} R^2 B \rho^{1/2} \Delta u^2 \sin^2 \theta, \tag{4.4}$$

where R is the radius of the obstacle, and θ is the angle between the vectors $\boldsymbol{B}$ and $\boldsymbol{\Delta u}$. Assuming the planet is unmagnetised, we use the planetary radius R_p for the obstacle radius. The waves travel towards the star along the magnetic field line connecting it to the planet, and a fraction of their energy is converted into ECMI emission. The emission occurs at the local cyclotron frequency (Turnpenney et al., 2018):

$$\nu = 2.8 \times 10^{-3} \frac{B}{1\ \mathrm{G}}\ \mathrm{GHz}. \tag{4.5}$$

We assume emission can be generated everywhere along the magnetic field line connecting the planet to the star, provided the cyclotron frequency exceeds the plasma frequency:

$$\nu > \nu_\mathrm{p} = 9 \times 10^{-6} \sqrt{\frac{n_\mathrm{e}}{1\ \mathrm{cm}^{-3}}}\ \mathrm{GHz}. \tag{4.6}$$

Here n_e is the electron number density.

We trace each magnetic field line that connects to the planet's orbit back to the point where it connects to the surface of AU Mic. Both planets orbit through closed-field regions of the star's large-scale magnetic field, which predominantly resembles an aligned dipole (Klein et al., 2021b). This means that ECMI emission can be generated in both the Northern and Southern hemisphere of AU Mic. Checking the condition in Equation 4.6 is satisfied, we extract the magnetic field strength along the line and compute the cyclotron frequency with Equation 4.5. These regions are highlighted in blue in the left panel of Figure 4.3. We then compute the flux density observed at a distance d from the system as

$$F_\nu = \frac{\varepsilon P}{\Omega d^2 \nu}. \tag{4.7}$$

Here ε is the fraction of the wave energy from the interaction which is converted into ECMI emission. Observations of the Jupiter-Io interaction indicate that $\varepsilon \approx 0.01$ (Turnpenney et al., 2018), which we adopt here. Ω is the solid angle of the emission beam. Again, we adopt the observed value for the Jupiter-Io interaction of $\Omega = 1.6$ sr (Zarka et al., 2004).

We show the flux density induced by planet b in the Northern and Southern hemispheres of AU Mic as a function of its orbital phase in Figure 4.4. The flux density is colour-coded with the frequency of the emission. We find that planet b can induce emission from ~ 10 MHz – 3 GHz in both hemispheres, with flux densities ranging from $\sim 10^{-2} - 10$ mJy. Higher flux densities correspond to lower frequencies (see Equation 4.7). Note that planet c also can induce radio emission in this frequency range, albeit with flux densities that are around an order of magnitude lower. This is due to the term $B\rho^{1/2}$ in Equation 4.4 dominating at larger orbital distances, as the density and magnetic field strength drop off radially. As the planets orbit with different rotation periods however, they may produce distinct radio signals at different frequencies and periodicities that could be detected.

In Figure 4.4 we also highlight the emission that is generated at 140 MHz, which corresponds to the middle of the frequency range of 120 – 160 MHz at which some M dwarfs have recently been detected (Vedantham et al., 2020; Callingham et al., 2021). Vedantham et al. (2020) suggested that their observations of emission from the M dwarf GJ 1151 may be generated by a planet orbiting in the sub-Alfvénic regime. At 140 MHz, our results bear a strong resemblance to the observations of GJ 1151: both have flux densities of about 1 mJy which exhibit temporal variations. It would be very useful to obtain radio and near-simultaneous spectropolarimetric observations of M dwarfs similar to these systems so that this scenario could be explored further.

Time-varying nonthermal radio emission from AU Mic at 1.5 GHz was reported by Cox & Gibson (1985), with flux densities ranging from 2 – 3 mJy. Compared to our predicted fluxes induced by planet b at this frequency range, the observed flux densities are about an order of magnitude larger. If this emission was induced by either planet, it would require a much higher radio power than we predict. This could occur if the wind properties were enhanced in response to an increase in the magnetic field strength of AU Mic. Alternatively, if the radius of the obstacle were $R \approx 3.2\ R_\mathrm{p}$, the radio power estimated using Equation 4.4 would increase by an order of magnitude. We estimate that this would be the size of the magnetopause of planet b if it had a dipolar field strength of ~ 6 G (see Vidotto & Donati, 2017; Kavanagh et al., 2019). Therefore, not only could detection of planet-induced radio emission allow us to constrain the mass-loss rate of the host star, but also the magnetic field strength of the planet itself, if it is magnetised. As there is no polarisation information reported by Cox & Gibson (1985) however, we unfortunately cannot assess the origin of this emission this further. Future observations with the VLA, MWA, or upcoming SKA radio telescope would certainly be beneficial to search for radio signals in the frequency range at which we predict AU Mic could emit planet-induced radio emission. A derivable quantity such as the brightness temperature of the emission could allow for detected polarised emission indicative of being planet-induced to be distinguished from flaring emission, as has been illustrated by Vedantham et al. (2020).

4.5.2 Prox Cen

Radio emission from 1.1 – 3.1 GHz was recently detected from Prox Cen by Pérez-Torres et al. (2021). These observations occurred during April 2017, at same epoch the spectropolarimetric observations began for Prox Cen (Klein et al., 2021a). Pérez-Torres et al. (2021) suggested that this emission could be indicative of star-planet interactions. If this is the case, it would require the planet to be orbiting in the sub-Alfvénic regime. Our wind model of Prox Cen however, which has a mass-loss rate in agreement with the upper limit obtained by Wood et al. (2001), shows that planet b orbits in the super-Alfvénic regime for the entirety of its orbit. In order for the planet to induce radio emission from the corona of Prox Cen, the Alfvén surface would need to extend beyond the planet's orbit. This would require

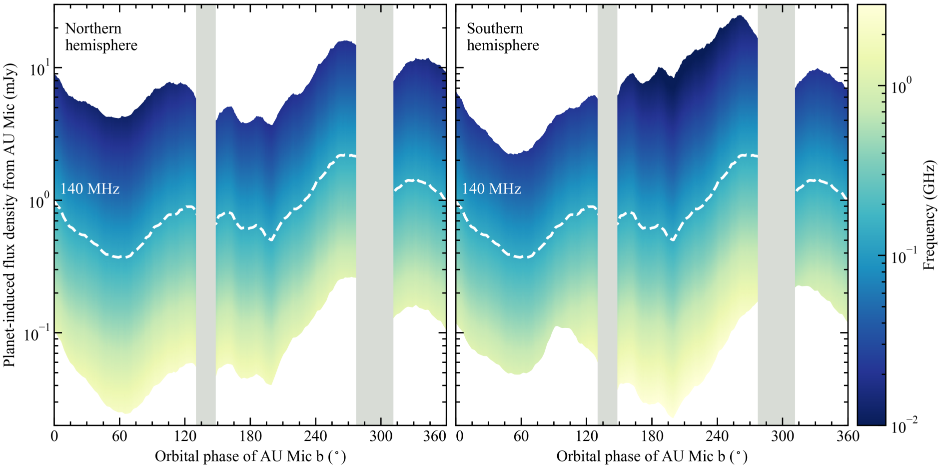

Figure 4.4: Radio spectrum of AU Mic induced by planet b in the Northern and Southern hemispheres of the star's corona (left and right panels respectively). Emission generated at 140 MHz is highlighted with a white dashed line. This is the middle frequency of the observing band at which radio emission was recently detected from the M dwarf GJ 1151 by Vedantham et al. (2020), which is suspected of being induced by an orbiting planet. The grey shaded areas illustrate the region where the orbit of planet is in the super-Alfvénic regime. No emission can generate in these regions (see Equation 4.6).

the mass-loss rate of the star to be significantly lower than the value we obtained of 0.25 $\dot{M}_\odot$.

To investigate this further, we ran two additional stellar wind models for Prox Cen, with Alfvén wave flux-to-magnetic field ratios of $S_\mathrm{A}/B = 1.1 \times 10^4$ erg s^{-1} cm^{-2} G^{-1} and 1.1×10^5 erg s^{-1} cm^{-2} G^{-1}. We obtain mass-loss rates of 0.05 $\dot{M}_\odot$ and 0.57 $\dot{M}_\odot$ respectively for these two simulations. In the case of the lower mass-loss rate model, we find that the planet still orbits entirely in a super-Alfvénic regime. Naturally, this is also the case for the model 0.57 $\dot{M}_\odot$, which has a denser wind than our model presented in Section 4.4.1.

We now use these results, combined with those from Section 4.4.1, to estimate the Alfvén wave flux-to-magnetic field ratio and mass-loss rate needed to place Prox Cen b in a sub-Alfvénic orbit. We first perform a least-squares power law fit between the Alfvén wave flux-to-magnetic field ratio S_A/B and mass-loss rate $\dot{M}$, and find that $\dot{M} = 2.6 \times 10^{-6} (S_\mathrm{A}/B)^{1.06}$ $\dot{M}_\odot$ for Prox Cen, where S_A/B is in erg s^{-1} cm^{-2} G^{-1}. The effects of changing S_A/B on the solar wind mass-loss rate were investigated by Boro Saikia et al. (2020) using the AWSoM model. For comparison, we fit the same power law to their results, and find that during solar minimum $\dot{M} \propto (S_\mathrm{A}/B)^{1.37}$, and during solar maximum $\dot{M} \propto (S_\mathrm{A}/B)^{1.42}$ (using the $l_\mathrm{max} = 5$ data in their Tables F.1 and F.2).

For Prox Cen, we compute the maximum radius of the Alfvén surface $R_\mathrm{A,\,orb}^\mathrm{max}$ in the orbital plane of the planet for each plot, and plot it with its corresponding Alfvén wave flux-to-magnetic field ratio and mass-loss rate in Figure 4.5. Again,

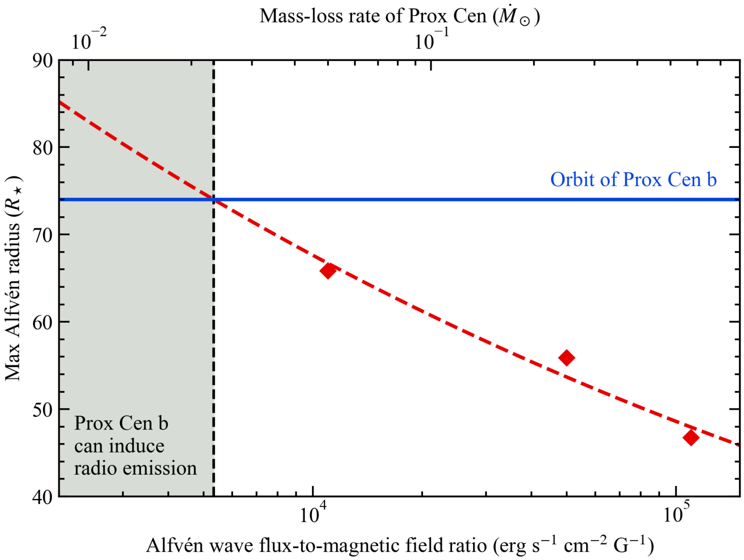

Figure 4.5: Average radius of the Alfvén surface in the orbital plane of Prox Cen b vs. the Alfvén wave flux-to-magnetic field ratio (red diamonds). The upper x-axis is scaled accordingly based on the mass-loss rate of each wind simulation. The red dashed line illustrates our least-squares power law fit to the datapoints. We extrapolate this fit to estimate the Alfvén wave flux-to-magnetic field ratio required for the Alfvén surface to exceed the orbital distance of the planet (blue horizontal line). If this condition is satisfied, the planet can induce the generation of radio emission in the corona of the Prox Cen. This region is shown in grey on the left-hand side. We find that an Alfvén wave flux-to-magnetic field ratio of $\leq 2.7 \times 10^{-3}$ erg s^{-1} cm^{-2} G^{-1} is needed for the planet to orbit inside the Alfvén surface. This corresponds to mass-loss rate of $\leq 1.1 \times 10^{-2}\ \dot{M}_\odot$ for Prox Cen.

performing a least-squares power law fit between $R^{\text{max}}_{\text{A, orb}}$ and S_A/B, we estimate that an Alfvén wave flux-to-magnetic field ratio of $< 5.3 \times 10^3$ erg s^{-1} cm^{-2} G^{-1} is required in order to place the plane in a sub-Alfvénic orbit. This corresponds to a stellar wind mass-loss rate of $< 2.3 \times 10^{-2}\ \dot{M}_\odot$, which is an order of magnitude lower than the upper limit obtained by Wood et al. (2001).

4.6 Discussion

There are some caveats to our planet-induced radio emission model. Firstly, we assume that the emission is always visible to the observer. However, it is well-established from observations of the Jupiter-Io interaction that the emission generated in this interaction is beamed in a hollow cone (see Zarka et al., 2004). As a result, if the emission can be generated it would likely be beamed in and out of the line of sight towards the system. Therefore, our results represent the best-case scenario where we always see the emission. We also do not account for the relative rotational motion between the star and planet, which would effect which stellar magnetic field line connects to the planet at any given time. Doing so would allow for us to estimate the temporal variations one would see observing the system, if this emission were detectable.

We also note that the higher radio fluxes we estimate for AU Mic in the case of a low mass-loss rate correspond to lower frequencies. However, as was shown by Kavanagh & Vidotto (2020), low frequency radio emission could suffer from significant attenuation from the stellar wind. We computed the thermal spectrum of AU Mic's low mass-loss rate wind using the model developed by Ó Fionnagáin et al. (2019a,b), and found that the wind is optically thick below ~ 0.1 GHz. This means that a significant amount of the low frequency planet-induced emission (< 0.1 GHz) we predict could be absorbed by the stellar wind. Note that we compute a peak flux density of ~ 0.5 μJy for the thermal wind spectrum of AU Mic, which is $2-3$ orders of magnitude smaller than the predicted planet-induced emission.

While we do not expect planet-induced radio emission from Prox Cen or AU Mic in the case that it has a high mass-loss rate, radio emission could still be generated in the magnetospheres of the orbiting planets (see Vidotto et al., 2019). For a low mass-loss rate however, AU Mic seems to be promising candidate for detectable planet-induced radio emission. Simultaneous spectropolarimetric and radio data of the system would be very complimentary to investigate this further, which would allow us to assess the stellar wind environment of AU Mic at the time of the radio observations. UV observations of the planetary transits could also be used in parallel, which have been shown to vary depending on the mass-loss rate of the host star (Carolan et al., 2020). In a broader context, the methods presented in the paper could be applied to a wide range of other suitable exoplanetary systems which may be capable of generating planet-induced radio emission.

4.7 Conclusions

In this paper, we presented Alfvén wave-driven stellar wind models for the two active M dwarfs Prox Cen and AU Mic, both of which are hosts to planets. We used our stellar wind models to investigate whether the orbiting planets could orbit sub-Alfvénically and induce radio emission in the coronae of their host stars, through a Jupiter-Io-like interaction. For Prox Cen, we constrained our stellar wind model using the upper limit for the mass-loss rate of 0.2 $\dot{M}_\odot$ obtained by Wood et al. (2001). We found that for this mass-loss rate, the planet orbits in the super-Alfvénic regime for its entire orbit. As a result, we do not expect that the planet could induce radio emission from the corona of the host star. By performing additional stellar wind simulations and extrapolating the results, we estimate that Prox Cen would need to have a mass-loss rate of $\leq 1.1 \times 10^{-2}$ $\dot{M}_\odot$ in order for the planet to orbit sub-Alfvénically. In other words, Prox Cen would need to have a mass-loss rate that is 20 times lower than the expected upper limit in order for the orbiting planet to induce radio emission in its corona.

For AU Mic, we investigated two scenarios, where the star has a low and high mass-loss rate. By adjusting the flux of Alfvén waves propagating out of the photosphere in our models, we obtained mass-loss rates of 27 $\dot{M}_\odot$ and 590 $\dot{M}_\odot$ respectively for the star. In the case of the low mass-loss rate (27 $\dot{M}_\odot$), we found that both planets b and c orbit sub-Alfvénically for the majority of their orbits. This means that both planets could induce the generation of radio emission in the corona of AU Mic. We showed that planet b could induce time-varying radio emission from $\sim$ 10 MHz – 3 GHz, with a peak flux density of $\sim$ 10 mJy. The radio emission we predict also bears a striking resemblance to that reported for the M dwarf GJ 1151 by Vedantham et al. (2020), which is suspected of be induced by a terrestrial planet in a 1 – 5 day orbit. Planet c could also induce radio emission in this frequency range, but with flux densities that are about an order of magnitude lower, and for a smaller fraction of its orbit. Due to the differences in orbital periods, both planets b and c could therefore produce radio emission distinct from one another. Comparing our estimated planet-induced radio emission for AU Mic to observations reported by Cox & Gibson (1985), we found that planet b could be magnetised, with a field strength of $\sim$ 6 G. However, as there is no polarisation information reported by Cox & Gibson (1985), we cannot assess further if this emission is indicative of being induced by the planets.

Our results illustrate that detection of planet-induced radio emission from AU Mic could allow us to constrain both the mass-loss rate of the star, as well as the magnetic field strength of the planet that induces the emission.

Acknowledgements

We thank the anonymous referee for their comments and suggestions. We also thank Dr. Joe Callingham, Dr. Sebastian Pineda, Prof. Harish Vedantham, and Prof. Jackie Villadsen for their insightful discussions. RDK acknowledges funding received from the Irish Research Council (IRC) through the Government of Ireland Postgraduate Scholarship Programme. AAV acknowledges funding from the European Research Council (ERC) under the European Union's Horizon 2020 research and innovation programme (grant agreement No 817540, ASTROFLOW). BK acknowledges funding from the European Research Council under the European Union's Horizon 2020 research and innovation programme (grant agreement No 865624, GPRV). MMJ acknowledges support from STFC consolidated grant number ST/R000824/1. JFD and BK acknowledge the ERC for grant agreement No 740651, NewWorlds. DÓF acknowledges funding from the IRC Government of Ireland Postdoctoral Fellowship Programme. We acknowledge the Irish Centre for High-End Computing (ICHEC) for providing the computational facilities used to perform the simulations published in this work.

5 | Radio masers on the active M dwarf WX UMa

5.1 Abstract

The nearby M dwarf WX UMa has recently been detected at radio wavelengths with LOFAR. The combination of its observed brightness temperature and circular polarisation fraction suggests that the emission is generated via the electron-cyclotron maser instability. Two distinct mechanisms have been proposed to power such emission from low-mass stars: either a sub-Alfvénic interaction between the stellar magnetic field and an orbiting planet, or reconnection at the edge of the stellar magnetosphere. In this paper, we investigate the feasibility of both mechanisms, utilising the information about the star's surrounding plasma environment obtained from modelling its stellar wind. Using this information, we show that a Neptune-sized exoplanet with a magnetic field strength of 10 – 100 G orbiting at ~ 0.034 au can accurately reproduce the observed radio emission from the star, with corresponding orbital periods of 7.4 days. Due to the stellar inclination, a planet in an equatorial orbit is unlikely to transit the star. While such a planet could induce radial velocity semi-amplitudes from 7 to 396 m s^{-1}, it is unlikely that this signal could be detected with current techniques due to the activity of the host star. The application of our planet-induced radio emission model here illustrates its exciting potential as a new tool for identifying planet-hosting candidates from long-term radio monitoring. We also develop a model to investigate the reconnection-powered emission scenario. While this approach produces less favourable results than the planet-induced scenario, it nevertheless serves as a potential alternative emission mechanism which is worth exploring further.

5.2 Introduction

Recent observations with the *LOw Frequency ARray* (LOFAR, Van Haarlem et al., 2013) have begun to shed light on the coherent radio emission mechanisms at play in the coronae of M dwarfs (Vedantham et al., 2020; Davis et al., 2021; Callingham et al., 2021). Many of these observations could be due to interactions between the star's magnetic field and a planet orbiting in the sub-Alfvénic region of the stellar wind, which can extend out to tens of stellar radii in the case of M dwarfs

(Davis et al., 2021; Kavanagh et al., 2021). Within 0.1 au, M dwarfs are expected to host numerous rocky exoplanets (Burn et al., 2021), the same region where the habitable zones of these stars are thought to lie (Kopparapu et al., 2013). Confirmation of such interactions at radio wavelengths would be a game-changer in the world of exoplanet detection, as these types of exoplanets remain largely undiscovered by other techniques. They could also provide a new avenue to probe both the magnetospheres of exoplanets, as well as the stellar wind environment of the host star (Kavanagh et al., 2021).

One such M dwarf that was recently detected by LOFAR as part of the LOFAR Two-metre Sky Survey (LoTSS, Shimwell et al., 2017) is the nearby active star WX Ursae Majoris (hereafter WX UMa) (Callingham et al., 2021). It is a fast rotator, and exhibits a strong and predominantly dipolar magnetic field, with an estimated average unsigned strength of ~ 1 kG derived from Stokes V observations (Morin et al., 2010). Additionally, Zeeman broadening measurements of the star suggest that the surfaced-averaged field strength could be up to 7 kG, the strongest field measured for a cool main-sequence star (Shulyak et al., 2017). The relevant physical parameters of WX UMa are listed in Table 5.1.

Between 2014 and 2016, WX UMa was detected nearly continuously in the radio over three 8-hour intervals (Davis et al., 2021; Callingham et al., 2021). The observed emission exhibits a high degree of circular polarisation ($\gtrsim 70\%$), with a peak flux density of ~ 1.2 mJy. The combined brightness temperature and high degree of circular polarisation of the emission implies that it is generated via a coherent emission mechanism. Two types of processes can produce coherent radio emission: plasma and cyclotron emission (Dulk, 1985). Plasma emission is powered by the conversion of turbulent Langmuir wave energy into electromagnetic energy. Such a scenario can occur when hot plasma is injected into a cooler and denser one, such as during the flaring of coronal loops (Zaitsev & Stepanov, 1983; Stepanov et al., 2001; Vedantham, 2021). However, Callingham et al. (2021) illustrated that the emission from WX UMa cannot be explained by plasma emission, due to the combination of its observed brightness temperature and circular polarisation fraction. Therefore, cyclotron emission is likely to be the mechanism producing the observed radio emission.

Cyclotron emission, or electron-cyclotron maser instability (ECMI) emission, occurs in rarefied, strongly magnetised plasmas (Dulk, 1985). The basic principle in a stellar/planetary context is as follows: electrons are accelerated along magnetic field lines, travelling towards regions of higher magnetic field strengths. This introduces a population of high-velocity electrons into the plasma relative to the already-existing thermal distribution. As the field strength increases, the field lines converge, and the accelerated electrons are reflected due to a magnetic mirroring effect, provided that their pitch angle (the angle between their velocity vector and the magnetic field) is large enough. This produces a so-called 'loss cone' or 'horseshoe' distribution, referring to the shape of the velocity space that the electrons which power the maser occupy (Treumann, 2006). These conditions have been identified as those necessary to drive the maser. If electrons are continuously accelerated, the maser will continue to be powered. The first star discovered to exhibit emission consistent with ECMI was the chemically peculiar star CU Vir

Table 5.1: Stellar parameters of WX UMa used in this work.

Stellar parameter	Value
Mass ($M_\star$)^1	0.095 $M_\odot$
Radius ($R_\star$)^2	0.12 $R_\odot$
Unsigned average large-scale magnetic field strength^2	1 kG
Rotation period ($P_\star$)^2	0.78 days
Inclination ($i_\star$)^2	40°
Distance (d)^3	4.9 pc

1: Newton et al. (2017); 2: Morin et al. (2010); 3: Gaia Collaboration et al. (2018)

(Trigilio et al., 2000).

Two sources of the energy required to power ECMI have been identified for stars. The first of these is analogous of the sub-Alfvénic interactions between Jupiter and Io (Neubauer, 1980; Hess et al., 2008; Saur et al., 2013). In this scenario, Io perturbs Jupiter's magnetic field in a sub-Alfvénic orbit, producing Alfvén waves which travel back towards Jupiter. The mechanical energy carried by the waves is then thought to subsequently dissipate, accelerating electrons and powering ECMI. For close-in exoplanetary systems, a similar process is thought to occur, where the roles of Jupiter and Io are taken by the star and planet respectively. Such interactions are expected to produce bright radio emission, at both MHz (Hess & Zarka, 2011; Turnpenney et al., 2018; Kavanagh et al., 2021) and GHz frequencies (Leto et al., 2017; Pérez-Torres et al., 2021). The current sheet regions of the plasma environments surrounding stars (Linsky et al., 1992; Trigilio et al., 2004; Nichols et al., 2012; Owocki et al., 2022) and planets (Cowley & Bunce, 2001) have also been identified as suitable acceleration sites for electrons in powering ECMI. In this scenario, magnetic reconnection is thought to provide electrons with energy at the edge of the magnetosphere, accelerating them to higher latitudes.

In this paper, we explore the feasibility of these two scenarios in reproducing the observed radio emission from WX UMa, utilising the plasma environment obtained from modelling its stellar wind environment. For the planet-induced scenario, we expand upon the model presented by Kavanagh et al. (2021), accounting for the beaming and polarisation of the generated emission, as well as the stellar rotational and planetary orbital motions for the first time in the literature. We then apply our updated planet-induced radio emission model to WX UMa, and investigate what planetary and orbital properties best-reproduce the radio observed emission of WX UMa. We also develop a model to investigate the reconnection-powered scenario.

5.3 Stellar wind environment of WX UMa

To model the stellar wind of WX UMa, we use the Alfvén wave-driven AWSoM model (van der Holst et al., 2014) implemented in the 3D magnetohydrodynamics

(MHD) code BATS-R-US (Powell et al., 1999). In this model, Alfvén waves propagate outwards from the base of the chromosphere along the stellar magnetic field lines. As they propagate, the waves are partially reflected. The interaction of the outward-propagating and reflected waves produces a so-called 'turbulent cascade', which dissipates the mechanical wave energy into thermal energy, heating the corona and driving the stellar wind outflow (Chandran et al., 2011).

BATS-R-US iteratively solves the ideal set of MHD equations in the stellar co-rotating frame on a three dimensional grid for a set of inputs, providing us with the density, magnetic field, velocity, pressure, current density, and Alfvén wave energy density of the stellar wind plasma in the observer's reference frame (Cohen et al., 2011; Vidotto et al., 2012; Garraffo et al., 2017; Alvarado-Gómez et al., 2019; Kavanagh et al., 2021; Evensberget et al., 2022). For our stellar wind model of WX UMa, we use a spherical grid that extends from the base of the chromosphere to 100 times the stellar radius. Our grid also includes regions of enhanced resolution, in order to mitigate the effects of numerical dissipation. The total number of cells in our grid is around 8,000,000. Once the mass-loss rate of the star changes by less than 10 percent between iterations, we take this to be the steady-state solution for our set of input values.

The main inputs for the AWSoM model are the mass, radius, and rotation period of the star, as well as the stellar surface magnetic field. For the magnetic field we use the map of the star in 2006, which was reconstructed by Morin et al. (2010) using the Zeeman-Doppler imaging method. The radial component of the map is implemented at the inner boundary of our wind model, which is shown in Figure 5.1. Another key parameter in the model is the Alfvén wave flux-to-magnetic field ratio S_A/B, which affects the amount of mass lost via the stellar wind (see Boro Saikia et al., 2020; Kavanagh et al., 2021; Ó Fionnagáin et al., 2021). This is a free parameter in our model. For WX UMa, we adopt an Alfvén wave flux-to-magnetic field ratio of $S_A/B = 1 \times 10^5$ erg s^{-1} cm^{-2} G^{-1}. This produces a stellar wind with a mass-loss rate of 2.1×10^{-14} $M_\odot$ yr^{-1}. With an X-ray luminosity of 3.1×10^{27} erg s^{-1} (Schmitt & Liefke, 2004), the mass-loss rate we obtain for WX UMa is in agreement with emerging trends between the mass-loss rates and surface X-ray fluxes of low-mass stars (see Jardine & Collier Cameron, 2019; Wood et al., 2021; Vidotto, 2021). Note that for the remaining inputs in the model relating to the Alfvén wave physics, we adopt those presented in Kavanagh et al. (2021). In Appendix A, we show the density, electron temperature, and magnetic field strength profiles of the stellar wind of WX UMa.

With a mass-loss rate of 2.1×10^{-14} $M_\odot$ yr^{-1}, we find that the stellar wind of WX UMa is sub-Alfvénic out to $\sim$ 60–80 $R_\star$, in the reference frame of a planet orbiting in the equatorial plane. We also find that the closed-field region of the star's magnetic field extends out to $\sim$ 40 $R_\star$ in the current sheet (where the radial magnetic field is zero). A 3D view of the stellar wind environment is shown in Figure 5.2. The location of the Alfvén surface of the stellar wind in the equatorial plane is of particular interest, as inside this region, an orbiting planet can induce the generation of radio emission along the magnetic field line connecting the planet and star. In the reference frame of an orbiting planet, the sub-Alfvénic region is defined as where the relative velocity between the stellar wind and the planet (Δu)

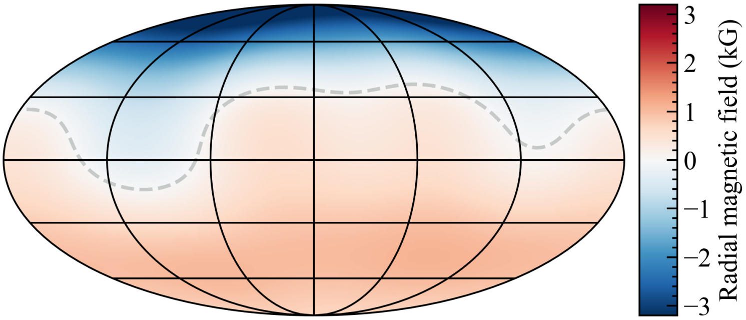

Figure 5.1: Radial surface magnetic field map of WX UMa in 2006, reconstructed by Morin et al. (2010). We implement this at the inner boundary in our stellar wind model. The dashed grey line shows where the polarity is neutral ($B_r = 0$). We refer to the visible hemisphere (the pole with a negative polarity) as the Northern hemisphere.

is less than the local Alfvén velocity:

$$\Delta u < u_{\mathrm{A}} = \frac{B_{\mathrm{w}}}{\sqrt{4\pi\rho_{\mathrm{w}}}}, \tag{5.1}$$

where B_{w} and ρ_{w} are the magnetic field strength and density of the stellar wind at the position of the planet.

The location of the Alfvén surface in the current sheet of the stellar wind plasma is also of interest in the context of radio emission, in that it is thought to be a point of significant acceleration for electrons at the edge of planetary and stellar magnetospheres, powered via magnetic reconnection (Linsky et al., 1992; Trigilio et al., 2004; Cowley & Bunce, 2001; Nichols et al., 2012; Owocki et al., 2022). In the following Sections, we explore the feasibility of both the planet-induced and reconnection scenarios in producing the observed emission of WX UMa at 144 MHz, utilising the information about the plasma environment obtained from our modelling of the stellar wind.

5.4 Emission induced by an orbiting planet

If there is a planet orbiting inside the Alfvén surface of WX UMa (i.e. at an orbital distance of $\lesssim 80\ R_\star$), it can perturb the magnetic field of the star and produce Alfvén waves (Neubauer, 1980). These waves can travel back to the star along the field lines connecting to the planet, producing radio emission via ECMI (Saur et al., 2013; Turnpenney et al., 2018). In Kavanagh et al. (2021), we developed a model to compute the emission generated in this type of interaction, which accounts for the realistic magnetic field structure and plasma environment of the star obtained from stellar wind simulations such as that shown in Figure 5.2. Here, we expand upon this model further, accounting for both the beaming and polarisation of the

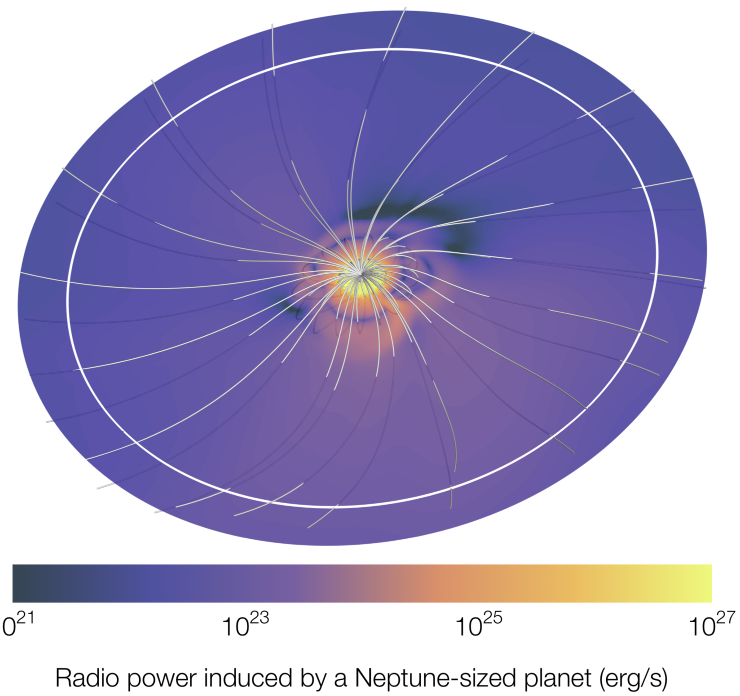

Figure 5.2: Simulated stellar wind environment of WX UMa out to a distance of 70 $R_\star$ ($\sim$ 0.039 au). The equatorial plane is coloured with the radio power that can be induced in the star via Alfvén waves generated through a sub-Alfvénic interaction with a Neptune-sized planet with a 10 G magnetic field at that location. Around 1% of the Alfvén wave energy is expected to be converted into radio emission. In the case of WX UMa, sub-Alfvénic interactions can occur out to $\sim$ 80 $R_\star$ in the equatorial plane. The white circle shows the orbital distance (0.034 au) we identify where a Neptune-sized exoplanet could orbit and induce emission at 144 MHz, comparable to that recently detected with LOFAR (see Section 5.4.1). The grey lines show the large-scale magnetic field of the star.

generated emission, as well as the respective stellar rotational and orbital motions of the potential planet.

ECMI emission is beamed in a hollow cone (Dulk, 1985), which will only be seen by the observer if the beam points along the line of sight. We take the emission cone to have an opening angle α and thickness $\Delta\alpha$. The angle α is measured from the tangent $\boldsymbol{L}$ of the magnetic field that points away from the stellar surface, and the unit vector $\hat{\boldsymbol{x}}'$ points towards the observer. For WX UMa, the visible (Northern) hemisphere exhibits a predominantly negative polarity (Figure 5.1), and therefore $\boldsymbol{L} = -\boldsymbol{B}$, where $\boldsymbol{B}$ is the magnetic field. A sketch of the geometry described here is shown in Figure 5.3.

The angle formed between the emission cone and line of sight in the Northern hemisphere is given by

$$\cos\beta = \frac{\boldsymbol{L}\cdot\hat{\boldsymbol{x}}'}{B\hat{x}'} = \frac{-\boldsymbol{B}\cdot\hat{\boldsymbol{x}}'}{B\hat{x}'} = \frac{-{B_x}'}{B}, \tag{5.2}$$

where ${B_x}'$ is the magnetic field component at the emission site that points towards the observer. Note that in the Southern hemisphere, the tangent vector is $\boldsymbol{L} = \boldsymbol{B}$. In general, the radial magnetic field at the emitting point B_r tells us the direction of the tangent vector. The emission is beamed towards the observer if the angle β is in following range:

$$\alpha - \frac{\Delta\alpha}{2} < \beta < \alpha + \frac{\Delta\alpha}{2}. \tag{5.3}$$

100% circularly polarised ECMI emission is generated at either the fundamental or second harmonic of the local cyclotron frequency:

$$\nu_{\mathrm{c}} = \frac{eB}{2\pi m_e}, \tag{5.4}$$

where e and m_e are the electron charge and mass respectively. Note that for ECMI emission to be generated, the cyclotron frequency must exceed the local plasma frequency (Dulk, 1985):

$$\nu_{\mathrm{c}} > \nu_{\mathrm{p}} = \sqrt{\frac{e^2 n_e}{\pi m_e}}, \tag{5.5}$$

where n_e is the electron number density.

The polarisation of ECMI emission depends on the magnetic polarity of the point on the field line where it is generated relative to the observer, as well as the magnetoionic mode. For LOFAR, the convention for emission in the o-mode is that the Stokes V flux is observed with a positive sign for a positive polarity ($B_r > 0$), and negative for a negative polarity ($B_r < 0$) (Davis et al., 2021). For x-mode emission, the reverse is true. The predominantly negative flux density of WX UMa presented by Davis et al. (2021) therefore implies that the emission either originates from the Northern hemisphere via o-mode emission, or from the Southern hemisphere via x-mode emission (refer to the respective magnetic polarities in Figure 5.1).

Provided that Equations 5.3 and 5.5 are satisfied, an observer at a distance d from the star receives a planet-induced flux density of

$$F_\mathrm{p} = \frac{\varepsilon P}{\Omega d^2 \Delta\nu}, \tag{5.6}$$

where the sign of the received flux depends on the magnetic polarity of the emitting point (the sign of ${B_x}'$), and the magnetoionic mode of the emission. Here, $\Delta\nu$ is the bandwidth of the emission, which we take as the difference between the maximum and minimum frequency along the field line where Equation 5.5 is satisfied. For a given field line, the bandwidth of second harmonic emission is twice that of fundamental emission. We assume that the flux density is constant with the emitted frequency, which is consistent with the observed spectra of ECMI emission on Jupiter (Zarka, 2004).

We consider emission at the middle of the observing band here ($\nu = 144$ MHz), where ν is either ν_c (fundamental emission) or $2\nu_\mathrm{c}$ (second harmonic emission). In Equation 5.6, ε is the fraction of the Alfvén wave energy that is converted into radio emission, which from observations of the Jupiter-Io sub-Alfvénic interaction imply that $\varepsilon = 0.01$ (Turnpenney et al., 2018). We use the same value in our calculations. Ω is the solid angle of the emission cone, which we compute as

$$\Omega = \int_0^{2\pi} \int_{\alpha-\Delta\alpha/2}^{\alpha+\Delta\alpha/2} \sin\theta d\theta d\phi = 4\pi \sin(\alpha)\sin(\Delta\alpha/2). \tag{5.7}$$

The emission cone produced in the Jupiter-Io sub-Alfvénic interaction is observed to have an opening angle of $\alpha = 75°$ and thickness of $\Delta\alpha = 15°$ (Zarka et al., 2004), giving a solid angle of $\Omega = 1.58$ sr. Again, we adopt the same value here.

The power of the Alfvén waves generated by the sub-Alfvénic interaction is (see Appendix B):

$$P = \pi^{1/2} {R_\mathrm{m}}^2 B_\mathrm{w} \rho_\mathrm{w}^{1/2} \Delta u^2 \sin^2\theta. \tag{5.8}$$

Here, R_m is the effective radius of the planet, which in the case of a magnetised planet, can be approximated as the size of its magnetopause. The magnetopause extends out to where the magnetic pressure of the planet equals that of the incident stellar wind, which is predominantly magnetic in the sub-Alfvénic region. Therefore, with an incident stellar wind with a magnetic field strength of B_w, and a planetary field strength at the magnetopause of $B_\mathrm{p,m}$, pressure balance gives (Vidotto et al., 2013):

$$\frac{{B_\mathrm{w}}^2}{8\pi} \simeq \frac{{B_\mathrm{p,m}}^2}{8\pi}. \tag{5.9}$$

For a dipolar magnetic field that is aligned with the stellar rotation axis, the strength of the planetary field at the magnetopause is

$$B_\mathrm{p,m} = \frac{B_\mathrm{p}}{2}\left(\frac{R_\mathrm{p}}{R_\mathrm{m}}\right)^3, \tag{5.10}$$

where B_p and R_p are the planetary polar magnetic field strength and radius. Plugging this in to Equation 5.9, we can obtain an expression for the magnetopause size:

$$R_{\mathrm{m}} = \left(\frac{1}{2}\frac{B_{\mathrm{p}}}{B_{\mathrm{w}}}\right)^{1/3} R_{\mathrm{p}}. \tag{5.11}$$

As the large-scale magnetic field of WX UMa resembles an aligned dipole, the equatorial field strength exhibits small variations in a circular orbit around the star. Combined with the weak dependence on the stellar wind magnetic field strength in Equation 5.11, the size of the magnetopause is effectively constant for a given orbital distance.

In terms of the remaining terms in Equation 5.8, ρ_{w} is the density of the stellar wind at the position of the planet respectively, and Δu is the relative velocity between the stellar wind and planet. At a distance a from the star, we assume that the planet is in a circular orbit in the equatorial plane of the star, moving in the positive azimuthal direction $\hat{\boldsymbol{\phi}}$ (prograde orbit). The planet orbits with a Keplerian velocity of $\boldsymbol{u}_{\mathrm{p}} = \sqrt{GM_\star/a}\hat{\boldsymbol{\phi}}$, where G is the gravitational constant. The relative velocity between the stellar wind and planet is given by $\boldsymbol{\Delta u} = \boldsymbol{u}_{\mathrm{w}} - \boldsymbol{u}_{\mathrm{p}}$, and θ is the angle between the vectors $\boldsymbol{\Delta u}$ and $\boldsymbol{B}_{\mathrm{w}}$.

We assume that the planet has an initial orbital phase of $\phi_{\mathrm{p},0}$ at the start of the stellar rotation phase covering the beginning of the 2014 radio observations. The star subsequently progresses by rotation phase $\phi_\star$, and the planet phase increases by ϕ_{p}. A sketch of the geometry described here is shown in Figure 5.4. At the stellar rotation phase $\phi_\star$, the planet intercepts the magnetic field line at longitude

$$\phi_l = \phi_{\mathrm{p},0} + \phi_{\mathrm{p}} - \phi_\star = \phi_{\mathrm{p},0} + \left(\frac{P_\star}{P_{\mathrm{p}}} - 1\right)\phi_\star. \tag{5.12}$$

In the stellar coordinate system, Equation 5.12 describes the position of the planet in the equatorial plane of stellar wind as a function of stellar rotation. The two phases $\phi_\star$ and ϕ_{p} relate to one another via the stellar rotation and orbital periods $P_\star$ and P_{p}:

$$\phi_{\mathrm{p}} = \frac{P_\star}{P_{\mathrm{p}}}\phi_\star, \tag{5.13}$$

and P_{p} is given by Kepler's third law:

$$P_{\mathrm{p}} \approx 2\pi\sqrt{\frac{a^3}{GM_\star}}. \tag{5.14}$$

5.4.1 Can the emission from WX UMa be explained by an undetected planet?

Our goal here is to determine whether the observed emission from WX UMa presented by Davis et al. (2021) can be reproduced by a planet orbiting in the sub-Alfvénic regime of the stellar wind. If so, what are the planetary and orbital parameters that best-reproduce the radio emission of the star? In our model, the planet's magnetopause size R_{p}, orbital distance a, and initial orbital phase $\phi_{\mathrm{p},0}$ are free parameters. For orbital distances $\lesssim 5\ R_\star$, fundamental ECMI emission

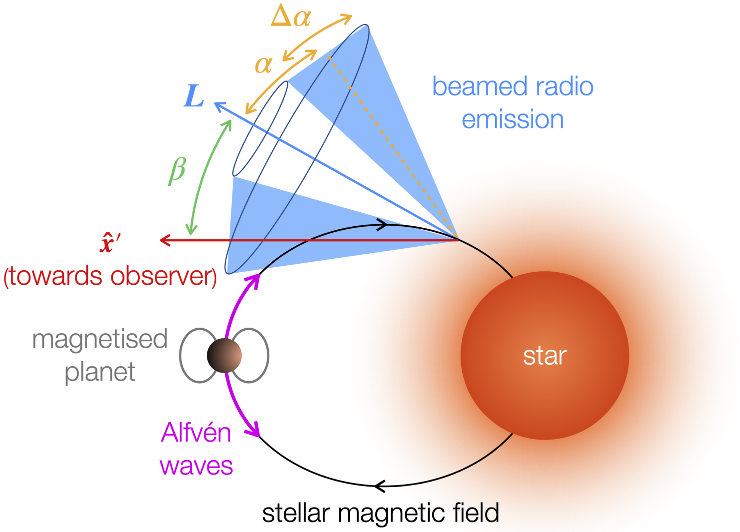

Figure 5.3: Sketch of the emission cone geometry for the planet-induced scenario. If a planet orbits its host star with a sub-Alfvénic velocity (Equation 5.1), it can produce Alfvén waves which carry energy back towards the star along the field line connecting the star and planet. This energy then dissipates near the surface, producing radio emission via ECMI. In the closed-field region of the star's magnetic field, the field line connects the planet back to the star in both hemispheres, producing emission in two locations. For clarity here we show emission generated in the Northern hemisphere only. If the planet orbits in the open-field region however, the generation of ECMI is limited to one hemisphere. The emission generated is beamed in a hollow cone, with an opening angle α and a thickness $\Delta\alpha$. The angle α is measured from the tangent to the magnetic field line $\boldsymbol{L}$ which points away from the stellar surface, in the opposite direction of the Alfvén wave propagation. The vector $\hat{\boldsymbol{x}}'$ points towards the observer, and β is the angle between $\boldsymbol{L}$ and $\hat{\boldsymbol{x}}'$. If β is in the range of $\alpha \pm \Delta\alpha$, the emission is seen by the observer.

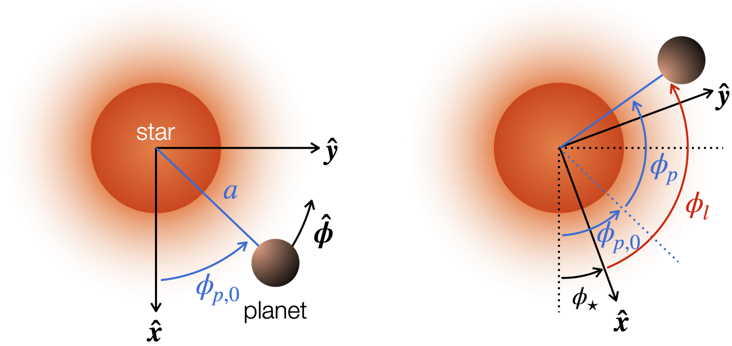

Figure 5.4: Top-down view of the equatorial plane of the star, defined by vectors $\hat{\boldsymbol{x}}$ and $\hat{\boldsymbol{y}}$. The rotation axis points out of the figure. The planet orbits in the direction of the vector $\hat{\boldsymbol{\phi}}$. Initially, it is at an orbital phase of $\phi_{\mathrm{p},0}$, at a distance a from the star (left). Then, the star rotates by phase $\phi_\star$, and the planet progresses by phase ϕ_{p} (right). The phase ϕ_l is the longitude of the magnetic field line in the stellar coordinate system that the planet intercepts as it orbits the star. For clarity, we do not show the planet's own magnetosphere.

cannot be generated, as the magnetic field strength of each line exceeds that required for fundamental ECMI at 144 MHz (the middle of the observing band). Similarly, second harmonic ECMI emission is limited to orbital distances $\gtrsim 7\ R_\star$. At $\sim 80\ R_\star$, the stellar wind also becomes super-Alfvénic, and for orbits greater than this distance, an orbiting planet can no longer induce radio emission from the star. Therefore, we limit our range of orbital distances to 5–80 $R_\star$ for fundamental ECMI, and 7–80 $R_\star$ for second harmonic ECMI respectively.

Within these ranges of orbital distances, we vary the value of $\phi_{\mathrm{p},0}$ from 0 to 1, and find the point on the magnetic field line connecting to this location in the orbital plane that corresponds to fundamental and second harmonic ECMI emission via Equation 5.4. For each position of the planet, we linearly interpolate the relevant stellar wind properties to compute the power of the Alfvén waves generated via Equation 5.8, as well as those needed to determine the beaming angle at a given frequency on the connecting field line via Equation 5.2. Provided that the emission from each point is beamed towards the observer (Equation 5.3), and the cyclotron frequency exceeds the local plasma frequency (Equation 5.5), we compute the flux density that the observer sees for a range of radii using Equation 5.6. We also consider emission in both the x and o-mode, accounting for the respective sign of the flux density, which depends on the orientation of the magnetic field relative to the observer (see Section 5.4). We perform our calculations for all stellar rotation phases covered by the radio observations of WX UMa, using Equation 5.12 to determine the magnetic field line the planet intercepts as the star rotates. This gives us the flux density of fundamental and second harmonic ECMI emission induced by the planet as a function of stellar rotation, which we refer to as the 'radio lightcurve' of the star.

To determine which set of parameters best-reproduce the observed radio lighcurve of WX UMa, we use a χ^2 test as a guide. We calculate the value of χ^2 as

$$\chi^2 = \sum \frac{(F_{\rm obs} - F_{\rm p})^2}{n_{\rm obs}{\sigma_{\rm obs}}^2}, \tag{5.15}$$

where $F_{\rm obs}$ and $\sigma_{\rm obs}$ are the observed flux and its respective error, $n_{\rm obs}$ is the number of observed flux values, and $F_{\rm p}$ is the planet-induced flux density computed using Equation 5.6. The lightcurve presented in Davis et al. (2021) is binned in to 2-hour windows, which is too coarse for comparison to our model. Therefore, following the same procedure described in Davis et al. (2021), we extract the 144 MHz lightcurve with a temporal resolution of $\sim$ 20 minutes, giving a total number of observations of $n_{\rm obs} = 72$ (24 for each epoch).

We compute the value of χ^2 for each set of inputs, and then visually check the lightcurves that produce values of $\chi^2 \approx 1$. For fundamental ECMI emission, we find that the observed lightcurve of WX UMa is best-reproduced by a planet orbiting the star at $\sim$ 0.034 au (60.6 $R_\star$), with a χ^2 value of 0.97. The magnetoionic mode we identify here is the *o*-mode, with the induced emission occurring in the Northern hemisphere. The initial orbital phase of the planet relative to the 2014 radio observations is 0.15, and the corresponding magnetopause size for these values is 11.9 $R_{\rm Nep}$. For reference, the size of Jupiter's magnetopause varies from $\sim$ 50 to 100 Jupiter radii depending on the solar wind conditions (Bagenal, 2013). Using Equation 5.11, the resulting planetary radius is 0.9 – 1.9 Neptune radii ($R_{\rm Nep}$) for polar magnetic field strengths from 10 — 100 G, which is the range of inferred field strengths for hot Jupiters (Table 3 of Cauley et al., 2019, neglecting their values for an efficiency of 100%).

For second harmonic ECMI emission, the planet that best-reproduces the observed emission also orbits at $\sim$ 0.034 au, with an initial orbital phase of 0.13 and a corresponding χ^2 of 0.92. Again, we identify the emission to occur in the *o*-mode here. The size of the magnetopause is 16.6 $R_\star$, which is larger than that for fundamental ECMI, to compensate for the larger bandwidth $\Delta\nu$ in Equation 5.6 (for a given field line, the bandwidth of second harmonic emission is twice that of fundamental emission). For polar magnetic field strengths of 10 – 100 G, the planetary radius is 1.3 – 2.7 $R_{\rm Nep}$. We list the orbital phases of the planet in each case across the 3 observing epochs in Table 5.2.

In Figure 5.5, we show a comparison of the best-fitting planet-induced lightcurves for fundamental and second harmonic ECMI to the observed emission from WX UMa presented in Davis et al. (2021). The planet-induced flux densities obtained are predominantly negative, in agreement with the observations and the assumption that the emission occurs in the *o*-mode. The surface field of the star exhibits a predominantly negative polarity in the North pole. As a result, the open field lines connecting to the planetary orbits identified tend to connect back to the North pole as opposed to the South pole, producing a negative flux density.

We note that there is not a unique set of best-fitting values; rather, those presented here represent those that produce the lowest value of χ^2. We find a few additional values that produce reasonable fits to the observations. These typically have values of $\chi^2 \lesssim 1.3$. We list all sets of best-fitting values for fundamental and second harmonic emission in Table 5.3.

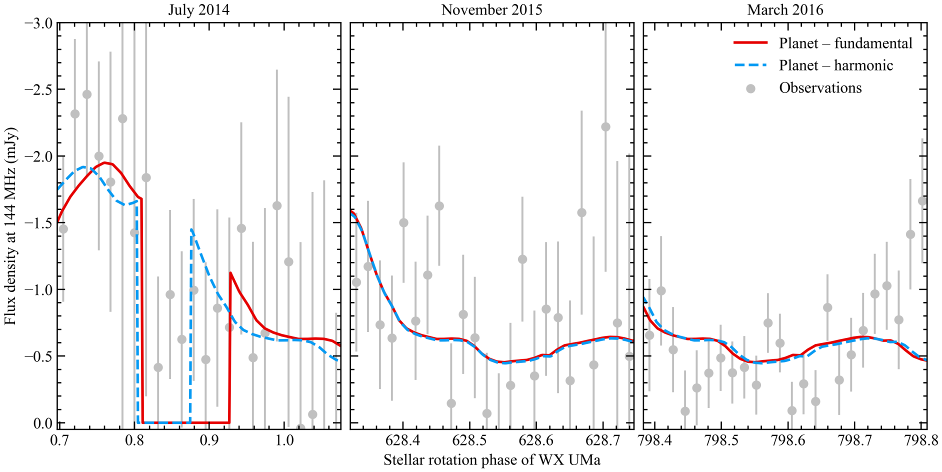

Figure 5.5: Best-fitting planet-induced radio lightcurves of WX UMa at 144 MHz, for fundamental (red) and second harmonic (blue) ECMI emission. In both cases, the predicted planet orbits at $\sim$ 0.034 au, with a magnetopause size of 11.9 and 16.6 R_{Nep} respectively. For planetary magnetic field strengths of 10 – 100 G, the radius of the planet ranges from 0.9 to 1.9 R_{Nep} in the case of fundamental ECMI, and 1.3 to 2.7 R_{Nep} for second harmonic ECMI. The grey dots and lines show the observed flux density and respective 1σ errors from WX UMa at a temporal resolution of $\sim$ 20 minutes.

Table 5.2: Orbital phases of the predicted planet that best-reproduces the observed lightcurve of WX UMa at 144 MHz during the 3 observing epochs, for fundamental and second harmonic ECMI. The values shown here are $\phi_{\mathrm{p},0} + \phi_{\mathrm{p}}$ (see Figure 5.4).

	July 2014	November 2015	March 2016
Fundamental	0.04 – 0.08	0.49 – 0.54	0.50 – 0.54
Harmonic	0.88 – 0.92	0.36 – 0.40	0.37 – 0.42

Table 5.3: Predicted planetary and orbital parameters that reproduce the observed lightcurve of WX UMa for fundamental and second harmonic ECMI emission, listed in order of increasing orbital distance. The values from left to right are the planetary orbital distance (a), orbital period (P_{p}), magnetopause size (R_{m}), radius assuming a polar magnetic field strength of 10 G ($R_{\mathrm{p,10\ G}}$) and 100 G ($R_{\mathrm{p,100\ G}}$) calculated using Equation 5.11, initial orbital phase $\phi_{\mathrm{p},0}$, and resulting χ^2 calculated using Equation 5.15. Values of $\chi^2 \lesssim 1.3$ generally produce reasonable results.

a (au)	P_{p} (days)	R_{m} (R_{Nep})	$R_{\mathrm{p,10\ G}}$ (R_{Nep})	$R_{\mathrm{p,100\ G}}$ (R_{Nep})	$\phi_{\mathrm{p},0}$	χ^2
Fundamental:						
0.028	5.4	8.4	1.6	0.7	0.13	1.20
0.033	7.2	9.3	1.5	0.7	0.15	1.32
0.034	7.4	11.9	1.9	0.9	0.15	0.97
Harmonic:						
0.028	5.4	14.7	2.7	1.3	0.10	1.08
0.034	7.4	16.6	2.7	1.3	0.13	0.92

5.4.2 Visibility of the potential planet

With the orbital and planetary parameters identified for a planet that could reproduce the observed emission from WX UMa, the next question is how visible would this planet be at different wavelengths? Here we explore the visibility of the planetary signatures, both in the radio and using traditional exoplanet detection methods.

Radio visibility at 144 MHz

First, in the radio we compute the planet-induced lightcurve at 144 MHz using the best-fitting values for fundamental and second harmonic ECMI emission identified in Section 5.4.1, covering the planetary orbit over 1000 stellar rotations. In both cases, we find that if we observe the system at randomly chosen 8-hour window, we catch the planetary signal 26% of the time when accounting for the emission beaming and plasma frequency condition (Equations 5.3 and 5.5). The average flux density induced via fundamental ECMI that is visible to the observer is -0.85 mJy, with a 1σ standard deviation of 0.50 mJy. For second harmonic ECMI, the average flux visible to the observer is -0.85 ± 0.54 mJy. For reference, 8 hour observations with LOFAR typically reach a sensitivity level of ~ 0.1 mJy. Considering that the 144 MHz emission from WX UMa is seen nearly continuously over the three separate epochs may make it difficult to reconcile with the planet-induced case presented here. That being said, a much longer radio observing campaign will be needed to assess this further. Additionally, propagation effects such as free-free/gyroresonance absorption and refraction may also further hinder the detection/visibility of a planet-induced signal (see Appendix D).

We then investigate what the dominant periods are in the planet-induced radio signal, which is useful information for planning future radio observations of the star. To explore this, we employ the Lomb-Scargle periodogram (Lomb, 1976; Scargle, 1982). In Figure 5.6, we show the periodogram of the planet-induced radio signal at 144 MHz for fundamental ECMI emission. The periodogram of the lightcurve induced via second harmonic ECMI gives the same result, as the orbital distances in both cases are equivalent. We find prominent peaks at the fundamental and harmonics of the orbital frequency of the planet $\nu_{\mathrm{p}} = 1/P_{\mathrm{p}}$, with the most dominant peak occurring at the second harmonic ($2\nu_{\mathrm{p}}$). This can be interpreted as when the planet intercepts field lines that are in the plane of the sky, which occurs twice per orbit. Such information could prove useful in carrying out future searches for such signals in the radio. In contrast, chromospheric emission lines such as Ca II H & K (3968.47 & 3933.66 Å) and He I D3 (5875.62 Å), which are thought to be tracers of star-planet interactions, are expected to show strong periodicity with the fundamental and harmonics of the beat period of the star and planet ($P_{\mathrm{beat}} = P_{\star} P_{\mathrm{p}} / |P_{\star} - P_{\mathrm{p}}|$) and the fundamental of the planetary orbital period (Fischer & Saur, 2019; Klein et al., 2022). This highlights the benefits of simultaneous multi-wavelength observations (e.g. optical and radio) in probing star-planet interactions.

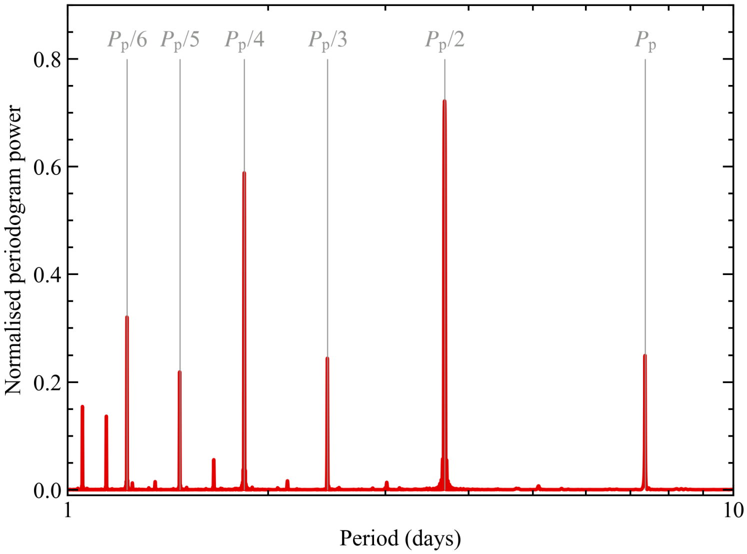

Figure 5.6: Periodogram of the planet-induced radio lightcurve at 144 MHz from WX UMa via fundamental ECMI. The lightcurve shows prominent periodicity at the fundamental and harmonics of the planetary orbital frequency $\nu_\mathrm{p} = 1/P_\mathrm{p}$, with the most dominant peak being found at the second harmonic. These are indicated by the vertical lines.

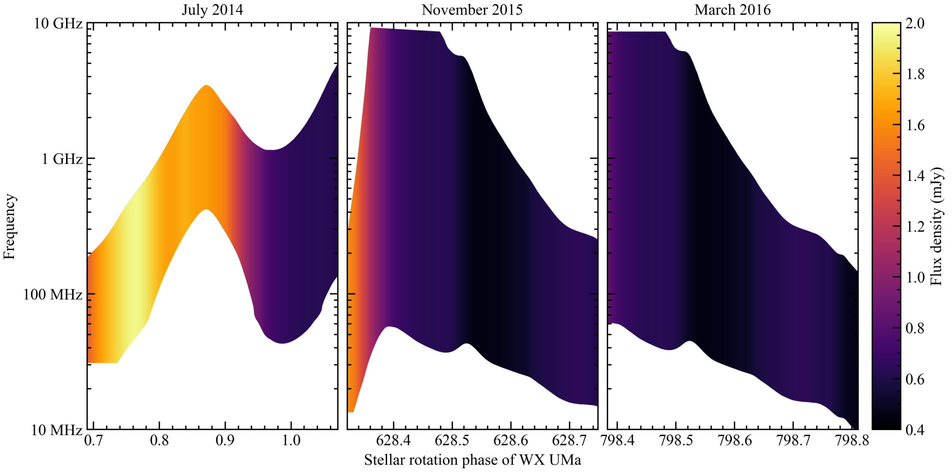

Figure 5.7: Dynamic radio spectra of WX UMa induced by the planet that best-reproduces the observed emission via fundamental ECMI at 144 MHz over the three epochs (left to right). At 144 MHz, the morphology of the flux density is that shown in Figure 5.5 for fundamental ECMI. The radio emission is only visible to the observer if it is beamed along the line of sight, and if the local cyclotron frequency exceeds the plasma frequency. Note here that we have neglected the sign of the flux density. In the LOFAR convention, this emission would be seen as a negative flux (from the Northern hemisphere).

Planet-induced dynamic radio spectrum of WX UMa

We now explore the range of possible emission frequencies along the entire magnetic field line connecting to the planet at each point in its orbit during the LOFAR observations. Provided Equation 5.5 is satisfied, and the emission is beamed towards the observer, we compute the flux density emitted from each point on the field line from 10 MHz to 10 GHz for fundamental ECMI emission, producing a dynamic radio spectrum at each of the three epochs. This frequency range covers all possible emitting frequencies via fundamental ECMI for the stellar magnetic field lines connecting to the predicted planetary orbit at ~ 0.034 au, which is determined by the field strength along each line (see Equation 5.4). The resulting dynamic spectrum is shown in in Figure 5.7. As the best-fitting orbital distance for second harmonic ECMI emission is the same as that for fundamental emission, the resulting dynamic spectrum is very similar, albeit over a bandwidth that is twice that of fundamental emission. This is shown in Figure 5.10. While both are comparable, detection of second harmonic emission may be more favourable than fundamental emission, as stellar winds are more optically thin at higher wavelengths in the radio regime (Panagia & Felli, 1975; Ó Fionnagáin et al., 2019a; Kavanagh et al., 2019, see Appendix D also). Multi-wavelength radio observations of the system could also help distinguish between the two modes (e.g. Das & Chandra, 2021).

Transit of the stellar disk

In terms of traditional exoplanet detection methods, for a planet to transit WX UMa, its orbital distance a must satisfy

$$a < \frac{R_\star + R_\mathrm{p}}{\sin i_\star}. \tag{5.16}$$

With a stellar inclination of $i_\star = 40^\circ$ (Morin et al., 2010) and a maximum radius of $\sim 2.7\ R_\mathrm{Nep}$, the planet would need to orbit WX UMa at a distance of $\lesssim 2.8\ R_\star$ (0.002 au), assuming it orbits in the equatorial plane. This value is smaller than the minimum orbital distance where fundamental or second harmonic ECMI emission can be induced in the star. Therefore, with our predicted orbital parameters, such a planet would not be detectable via transit observations.

Radial velocity signatures

While detectability via transits is not likely for the putative planet, it may be possible for it to generate measurable radial velocity signatures in spectroscopic lines from the star. The radial velocity semi-amplitude due to the presence of a planet is (Wright & Howard, 2009):

$$K = \left(\frac{G}{a}\right)^{1/2} \frac{M_\mathrm{p} \cos i_\star}{(M_\star + M_\mathrm{p})^{1/2}}, \tag{5.17}$$

where M_p is the mass of the planet. Assuming a Neptunian density of 1.6 g cm^{-3}, for a planetary radius of $0.7 - 2.7\ R_\mathrm{Nep}$ the semi-amplitude varies from $7 - 396$ m s^{-1}. A signal of this strength is well within the detection capabilities of current-generation spectrographs. However, radial velocity measurements of the star are likely to be completely dominated by stellar activity, with the associated radial velocity jitter ranging from $60 - 530$ m s^{-1} (Morin et al., 2010).

5.5 Reconnection at the edge of the magnetosphere

ECMI emission may also be generated from WX UMa without the presence of a planet. If reconnection occurs in the current sheet of the stellar wind plasma at the edge of the magnetosphere (Linsky et al., 1992; Trigilio et al., 2004; Nichols et al., 2012), electrons may be accelerated towards the magnetic polar regions. This acceleration could produce a population of high-velocity electrons in a loss-cone or horseshoe distribution, which in turn can power ECMI (see Section 5.2). Provided there is no evolution of the magnetic field or surrounding stellar wind plasma, emission generated via such a mechanism would be modulated by the stellar rotation period.

To investigate this scenario for WX UMa, we first identify the magnetic field lines connecting to the Alfvén surface in the middle of the current sheet (where the radial component of the magnetic field is zero). We then find the points along each field line which correspond to fundamental and second harmonic ECMI emission at 144 MHz using Equation 5.4. At each point, we assume that the emitted flux is proportional to an emission proxy p, which we normalise by its maximum value at the emitting points. We calculate the total flux as the sum the contributions from all emitting points at 144 MHz:

$$F = C \sum p, \tag{5.18}$$

where C is a scaling constant. Again, we check the same beaming and plasma frequency conditions described by Equations 5.3 and 5.5.

We consider two proxies for the emission in the closed field of WX UMa. The first follows the formulations of Llama et al. (2018), who illustrated that the observed radio modulation at 4 – 8 GHz of the active M dwarf V374 Peg can be reproduced by assuming the emission is proportional to the density of free electrons in the closed field. The second proxy utilised is the current density along the field lines. This is inspired by Ohmic heating, in which the energy is proportional to the square of the current density (Meyer et al., 2013; Gibb et al., 2014). Ohmic heating is thought to originate in reconnection events (Benz, 2017), such as those which may power ECMI from magnetised stars.

Utilising these two proxies, we carry out the same process as for the planet-induced scenario. By varying the scaling constant C in Equation 5.18, we determine what values minimises value of χ^2:

$$\chi^2 = \sum \frac{(F_{\mathrm{obs}} - F)^2}{n_{\mathrm{obs}} {\sigma_{\mathrm{obs}}}^2}. \tag{5.19}$$

As we assume that the large-scale magnetic field and plasma density do not change over the course of the radio observations, we phase-fold the data in our analysis here. Considering both proxies, combined with emission generated in both the x and o-mode via fundamental and second harmonic ECMI at 144 MHz, we find that only the density proxy can reproduce the observed emission via fundamental o-mode ECMI. The maximum density that we normalise the proxy by for the points emitting fundamental ECMI at 144 MHz is 1.56×10^9 cm^{-3}. The scaling constant obtained for the density proxy which best-reproduces the observed emission is $C = 0.21$ mJy, with a corresponding χ^2 of 2.03.

In Figure 5.8 we show a comparison of the phase-folded radio observations to that obtained using the density as a proxy for the emission. As the emission depends only on the structure of the magnetosphere, it is modulated by the stellar rotation period. This distinguishes it from planet-induced emission, which has prominent periodicity with harmonics of the planetary orbital frequency (e.g. Figure 5.6). We also overlay the line of sight magnetic field strength from Table A4 in Morin et al. (2010) in Figure 5.8 to compare to the phase-folded lightcurve. The modulation of these values seem to match the observed emission relatively well for rotation phases 0.3 – 0.7.

Visually, using the density as a proxy for the emission reproduces the observed phase-folded lightcurve relatively well. That being said, the drawback of the model here is that the value obtained for the scaling constant is not physically motivated, unlike those identified in the planet-induced scenario, which describe a sub-au orbit of a Neptune-sized planet around the star. Additionally, the fit to the data is poorer here than in the planet-induced scenario. However, we expect the planet-induced signal to be modulated primarily by harmonics of the orbital period of the potential planet (7.4 days), whereas for the reconnection scenario, the emission would be modulated with the stellar rotation period (0.78 days). A more stringent comparison of the two models therefore requires radio observations of the star covering multiple planetary orbits. Nevertheless, these proxies illustrate how the magnetospheric structure of the star may imprint itself in the resulting radio emission. Again, in future adaptations of a model such as this, accounting for the absorption and refraction of the generated emission may be necessary (see Appendix D). We also note that there have recently been numerous arguments made in the literature disfavouring a mechanism such as this in powering auroral emission on Jupiter, which is the inspiration for this scenario (Bonfond et al., 2020). It is also worth mentioning that recent work has illustrated that incoherent non-thermal radio emission from Jupiter's radiation belt is in agreement with that expected to be generated in the magnetospheres of hot B/A-type stars (Leto et al., 2021; Owocki et al., 2022).

5.6 Discussion & Conclusions

5.6.1 Model limitations

One caveat to the application of our models to WX UMa is the time interval between the observations used to reconstruct the stellar surface magnetic field and the radio observations. Our stellar wind simulation presented in Section 5.3 is effectively a snapshot of the wind of the star in April 2006, which is the epoch of the spectropolarimetric observations used by Morin et al. (2010) to reconstruct the surface field map implemented in our stellar wind model. The first LOFAR observations of the star then occurred in July 2014. Within this time, the magnetic field of the star could have evolved significantly. Morin et al. (2010) also derived a rotation period of 0.78 ± 0.20 days for star from the 2006 observations. Fast-forwarding to the start of the 2014 radio observations, the star had undergone over 3,800 rotations. Propagating the error in rotation period, the error in the stellar rotation phase in July 2014 is ± 99. As a result, there is a large uncertainty in the true rotation phase of the star during the radio observations. In order to mitigate this effect, near-simultaneous spectropolarimetric and radio observations and higher precision stellar rotation periods are needed.

Another set of aspects which are not addressed in our model are propagation effects on the escaping radio emission. These are not limited to refraction (Melrose & Dulk, 1982; Trigilio et al., 2011; Das et al., 2020), dispersion and scattering (Guedel & Zlobec, 1991), reflections off of density boundary layers in the corona (Melrose, 2006), and gyroresonance absorption, which is thought to be significant in the coronae of M dwarfs (Stepanov et al., 2001; Vedantham, 2021). Low-frequency radio emission can also be readily absorbed via free-free absorption (Rybicki & Lightman, 1986; Kavanagh & Vidotto, 2020). In Appendix D, we show

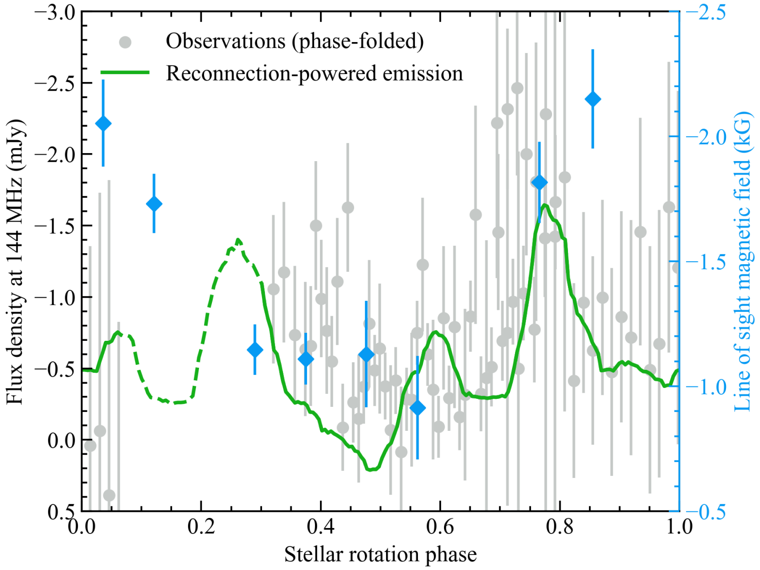

Figure 5.8: Comparison of the phase-folded radio observations of WX UMa at 144 MHz (grey dots) to that produced from the magnetosphere using the density of free electrons as the emission proxy (green line). The emission here is assumed to be generated in the *o*-mode via fundamental ECMI. The vertical bars show the 1σ errors associated with the observed flux densities. We do not consider the stellar rotation phases for the dashed part of the green line in our analysis, as there is no data available in this region. We also overlay the line of sight magnetic field strength from Morin et al. (2010) as blue diamonds. These values seem to follow the modulation of the phase-folded radio lightcurve relatively well between rotation phases 0.3 – 0.7.

both the refractive indices of x and o-mode emission, as well as the optical depth at 144 MHz. While self-consistently accounting for these processes is currently beyond the scope of this paper, their inclusion is worth exploring in the future.

There are two other parameters in our model which we did not explore in this work: the properties of the emission cone, and the conversion efficiency of the Alfvén waves produced by the star-planet sub-Alfvénic interaction to radio emission. These two parameters depend on the velocity of the accelerated electrons, which in turn is dependent on the conversion of the Alfvén wave energy. As this process of Alfvén wave generation via the sub-Alfvénic star-planet interaction is not explicitly calculated in our stellar wind simulation, we cannot determine appropriate values for these parameters in a self-consistent way.

5.6.2 Conclusions

In this paper, we presented a refined model for planet-induced radio emission from low-mass stars, based on its initial form developed by Kavanagh et al. (2021). This model utilises the realistic information about the large-scale stellar magnetic field and plasma environment that is provided by stellar wind simulations, and accounts for both the beaming and polarisation of the radio emission, as well as the respective stellar rotational and planetary orbital motion. To the best of our knowledge, it is the first of its kind in the literature.

Applying our updated model to the M dwarf WX UMa, we have shown that a Neptune-sized exoplanet with a magnetic field strength of 10 – 100 G orbiting the star at ~ 0.034 au can accurately reproduce recent radio observations of the star at 144 MHz. If the recent observations are indeed of a star-planet interaction origin, the signal with a strength of up to 2 mJy may be visible up to 26% of the time at 144 MHz, with the emission ranging from 10 MHz up to 20 GHz, depending on if the emission is generated at the fundamental or second harmonic of the local cyclotron frequency. While transits of our putative planet are unlikely due to the stellar inclination, the induced semi-amplitudes well within the detection capabilities of current-generation spectrographs are possible. That being said, the activity of the star may hinder such detections.

An interesting question arising from this work is how to distinguish between a planet inducing fundamental vs. second harmonic ECMI emission, as both can produce highly circularly polarised emission (Vedantham, 2021). Across the range of 10 MHz–20 GHz, the morphology of the emission does not differ significantly, however second harmonic emission is more prominent at higher frequencies by nature. If a planet-induced radio signature was identified, multi-wavelength radio observations would certainly aid disentangling the emission harmonic. In addition to this, fundamental ECMI emission may be more susceptible to being attenuated significantly as it propagates out of the system. As a result, detection may be more favourable in the case of second harmonic emission. Melrose & Dulk (1982) also illustrated that for a relative cool ($< 10^7$ K) and rarefied plasma ($< 3 \times 10^8$ cm^{-3}), emission at the second harmonic can escape more easily than fundamental emission, the latter of which being subjected to significant gyroresonance absorption (see Appendix D).

We also developed a model to explore an alternative proposed mechanism for generating ECMI in magnetised low-mass stars. This mechanism relies on persistent reconnection occurring at the edge of the stellar magnetosphere. We utilised the information obtained from our wind simulation about the large-scale magnetic field, and explored different emission proxies to mimic emission from the field lines associated with this region. We found that assuming the emission scales with the density of free electrons, we can reproduce the observed emission at 144 MHz to an extent, albeit with a poorer fit to the data than in the planet-induced scenario. However, we note here that there is no precedent for the associated scaling prescriptions obtained in this analysis. Future work will be needed to provide more realistically account for the energy available to power such mechanisms.

It is worth noting the differences between emission induced by a planet vs. that generated in the reconnection scenario. Over many orbital periods of the planet, there is a dominant periodicity at the fundamental and harmonics of the orbital frequency. This signature would easily distinguish it from the alternative proposed mechanism, which would show regular modulation with the stellar rotation period (assuming the magnetic field does not evolve significantly). Distinguishing between the two however would likely need a more extensive radio observing campaign.

To conclude, the planet-induced radio emission model presented here has fantastic potential for application to current and upcoming radio observations, to be used as a new tool to discover planets around nearby stars at radio wavelengths. However, alternative scenarios such as reconnection at the edge of the magnetosphere should also be explored further. Future application of our planet-induced model to radio observations of low-mass stars such as those presented by Callingham et al. (2021), as well as from upcoming developments such as the third phase of the Owens Valley Long Wavelength Array (OVRO-LWA, Hallinan et al., 2015) and FARSIDE lunar array (Hallinan et al., 2021) will be of great use in guiding follow-up observations using traditional exoplanet detection techniques.

Acknowledgements

We thank the anonymous referee for their insightful comments and suggestions. RDK acknowledges funding received from the Irish Research Council (IRC) through the Government of Ireland Postgraduate Scholarship Programme. RDK and AAV acknowledges funding from the European Research Council (ERC) under the European Union's Horizon 2020 research and innovation programme (grant agreement No 817540, ASTROFLOW). We acknowledge the provisions of the Space Weather Modelling Framework (SWMF) code from the Center for Space Environment Modeling (CSEM) at the University of Michigan, and the computational resources of the Irish Centre for High End Computing (ICHEC), both of which were utilised in this work.

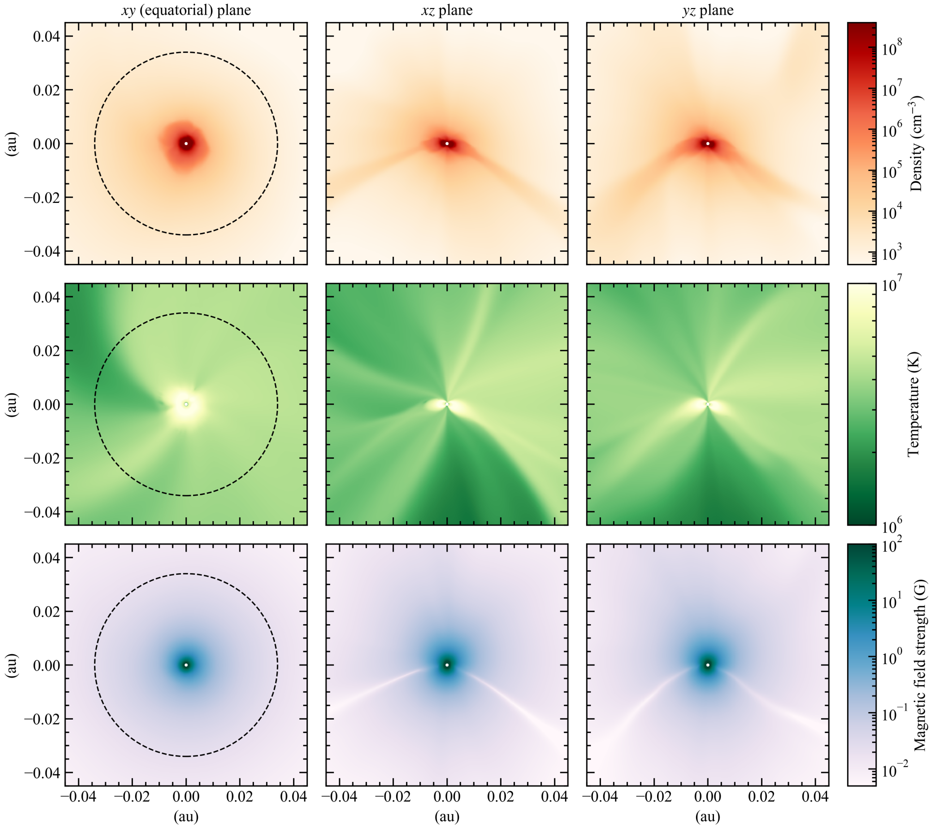

Figure 5.9: Profiles of the stellar wind density (top), electron temperature (middle), and magnetic field strength (bottom) of WX UMa, in the xy, xz, and yz planes (left to right). In the equatorial (xy) plane, we show the orbital distance (0.034 au) where a potential Neptune-sized planet can reproduce the observed radio emission from the star at 144 MHz through star-planet interactions. The z-axis is the rotation axis of the star.

Appendix A: Stellar wind plasma properties

In Figure 5.9 we present profiles of the stellar wind density, electron temperature, and magnetic field strength for each of the Cartesian planes in our model.

Appendix B: Power generated in sub-Alfvénic star-planet interactions

The power generated via the interaction between the stellar magnetic field and a planet in a sub-Alfvénic orbit is given by Equation (55) of Saur et al. (2013) in SI units:

$$P = \frac{2\pi}{\mu_0} {R_{\rm m}}^2 (\alpha M_A B_{\rm w} \cos\Theta)^2 u_{\rm A}. \tag{5.20}$$

Here μ_0 is the permeability of free space, α is the interaction strength, which is ≈ 1 for M-dwarfs (Turnpenney et al., 2018), $M_{\rm A} = \Delta u / u_{\rm A}$ is the Alfvénic Mach number, and Θ is the angle between vector $\Delta \boldsymbol{u}$ and the perpendicular component of the vector $\boldsymbol{B}_{\rm w}$. We write our Equation 5.8 in terms of θ, which is the angle between the vectors $\Delta \boldsymbol{u}$ and $\boldsymbol{B}_{\rm w}$. Comparing to Saur et al. (2013), $\theta = \pi/2 - \Theta$, and so in Equation 5.20 we have $\cos\Theta \equiv \sin\theta$. Rewriting Equation 5.20 in CGS units, we then have

$$P = \frac{1}{2} R^2 (M_{\rm A} B_{\rm w} \sin\theta)^2 u_{\rm A}, \tag{5.21}$$

and finally, expanding the factor ${M_{\rm A}}^2 / u_{\rm A}$ gives

$$P = \pi^{1/2} R^2 B_{\rm w} {\rho_{\rm w}}^{1/2} \Delta u^2 \sin^2\theta. \tag{5.22}$$

Appendix C: Dynamic radio spectrum of second harmonic ECMI

Here, we show the dynamic radio spectrum induced by the planet that best-reproduces the observed emission from WX UMa at 144 MHz, assuming it occurs via second harmonic ECMI. Emission can be generated from 20 MHz to 20 GHz for the field lines connecting to the orbit at 60.6 $R_\star$, twice that of the dynamic spectrum for fundamental emission shown in Figure 5.7. The slight differences in morphology between the fundamental and harmonic dynamic spectra are due to the different locations of the emitting points. The second harmonic dynamic radio spectrum is shown in Figure 5.10.

Appendix D: Propagation effects at 144 MHz

As laid out in Section 5.6.1, there are propagation effects that are not taken into account in our model, which may significantly alter the resulting observed emission from WX UMa. Here, we compute both the refractive indices of o and x-mode emission, as well as the optical depth of the stellar wind at 144 MHz. The square of the refractive index for o/x-mode emission is (Melrose & Dulk, 1982):

$${n_{o,x}}^2 = 1 - \frac{X T_{o,x}}{T_{o,x} - Y \cos\alpha}, \tag{5.23}$$

where

$$T_o = -{T_x}^{-1} = -(Z^2 + 1)^{1/2} - Z, \tag{5.24}$$

$$Z = \frac{Y \sin^2\alpha}{2(1 - X)\cos\alpha}, \tag{5.25}$$

$$Y = \frac{\nu_{\rm c}}{\nu}, \tag{5.26}$$

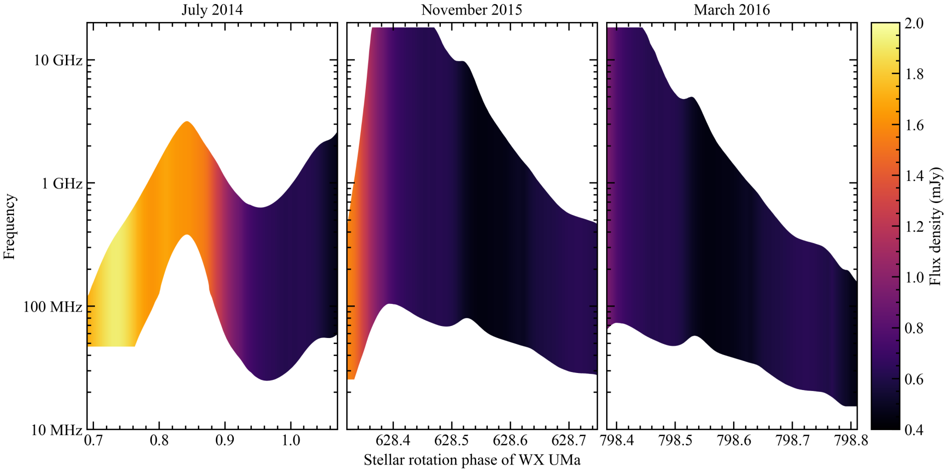

Figure 5.10: Same as Figure 5.7, but for second harmonic ECMI emission.

and

$$X = \left(\frac{\nu_\mathrm{p}}{\nu}\right)^2. \tag{5.27}$$

In Melrose & Dulk (1982), the above expressions are given as functions of the angle between the beam direction and the magnetic field. While in our analysis we consider beam angles for $\alpha \pm \Delta\alpha/2$, for brevity here we just compute the refractive indices for α. In the case where the refractive indices are real, the emission will deviate from its path as it propagates through the magnetosphere. However, if the refractive indices are imaginary, the emission will become attenuated (Leto et al., 2019). In Figure 5.11 we show the values of $n_{o,x}^2$ in the three Cartesian planes of the stellar wind. In general, x-mode emission is more likely to be absorbed as it propagates outwards, and naturally being generated further from the star, second harmonic ECMI can more readily escape. Regardless, Figure 5.11 illustrates that ECMI is likely to deviate from a straight line as it propagates outwards, passing in and out of attenuating regions in the process. Models which self-consistently account for these effects (e.g. Lo et al., 2012; Leto et al., 2016; Das et al., 2020) coupled with the planet-induced and reconnection models presented here are certainly worth exploring in the future.

Thermal free-free absorption may also attenuate the emission as it escapes the system. Here, we compute the free-free absorption of the stellar wind in the same manner as Ó Fionnagáin et al. (2019a) and Kavanagh & Vidotto (2020). The absorption coefficient for free-free emission in CGS units is (Rybicki & Lightman, 1986):

$$\alpha_\nu = 3.692 \times 10^8 Z^2 T^{-1/2} \nu^{-3} n_\mathrm{e} n_\mathrm{i} g (1 - e^{-h\nu/kT}). \tag{5.28}$$

Here, Z is the ionisation fraction of the plasma, n_e and n_i are the electron and ion number densities respectively, and g is the Gaunt factor, which at radio frequencies is (Cox, 2000):

$$g = 10.6 + 1.90 \log_{10}(T) - 1.26 \log_{10}(Z\nu). \tag{5.29}$$

As the wind is composed of fully ionised hydrogen, with temperatures of $\gtrsim 1$ MK (Figure 5.9), we set $Z = 1$, and $n_\mathrm{e} = n_\mathrm{i} = n$. The optical depth at each emitting point is the integral of the absorption coefficient along the line of sight x':

$$\tau_\nu = \int_{-\infty}^{{x_0}'} \alpha_\nu dx', \tag{5.30}$$

where ${x_0}'$ is the coordinate of the emitting point along the line of sight. Numerically, we replace the lower limit of the integral with max distance at which the wind is dense enough to increase the optical depth significantly (at around 10 $R_\star$). The optical depth then allows us to compute the factor the escaping emission is attenuated by, which is $e^{-\tau_\nu}$ (Kavanagh & Vidotto, 2020).

We compute the optical depth at the points along the stellar magnetic field lines connecting to the orbit of the potential planet identified in Section 5.4.1 that best-reproduces the LOFAR observations, accounting for the stellar inclination and rotation. The results are shown in Figure 5.12. We find a varying level of attenuation for emission during the three epochs, with fundamental ECMI being absorbed on average by 51%. Again, second harmonic ECMI is less attenuated, with 30% being absorbed on average. This is due to the emission being generated further from the star, which results in lower optical depths along the line of sight. These results clearly illustrate that accounting for free-free absorption, alongside magnetoionic refraction/absorption, should be considered in the model in a self-consistent way for future applications.

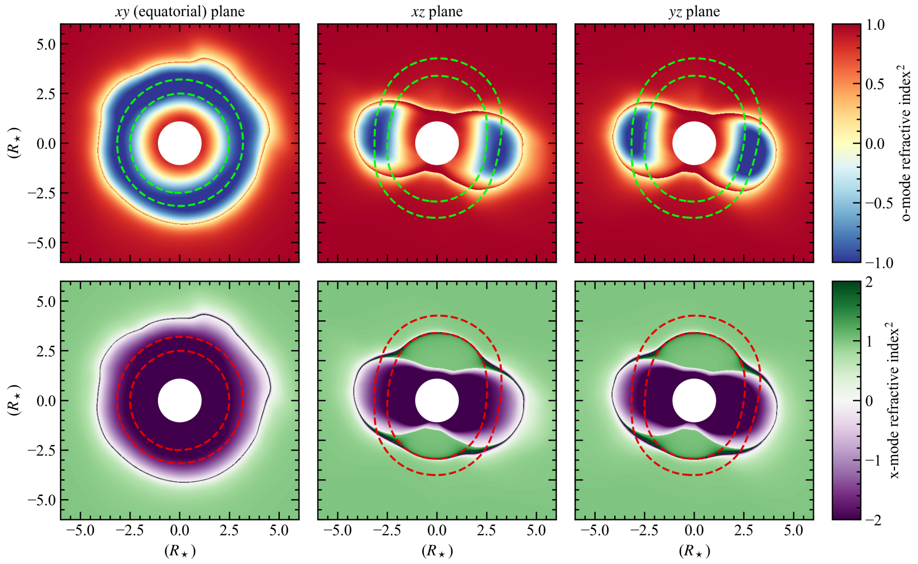

Figure 5.11: Square of the magnetoionic refractive indices of o (top) and x-mode emission (bottom) at 144 MHz of the wind of WX UMa. For a negative squared refractive index, the refractive index is imaginary, and the emission can no longer escape without being absorbed (Leto et al., 2019). The two dashed contours in each panel show the region where fundamental (inner) and second harmonic (outer) ECMI can be generated at 144 MHz.

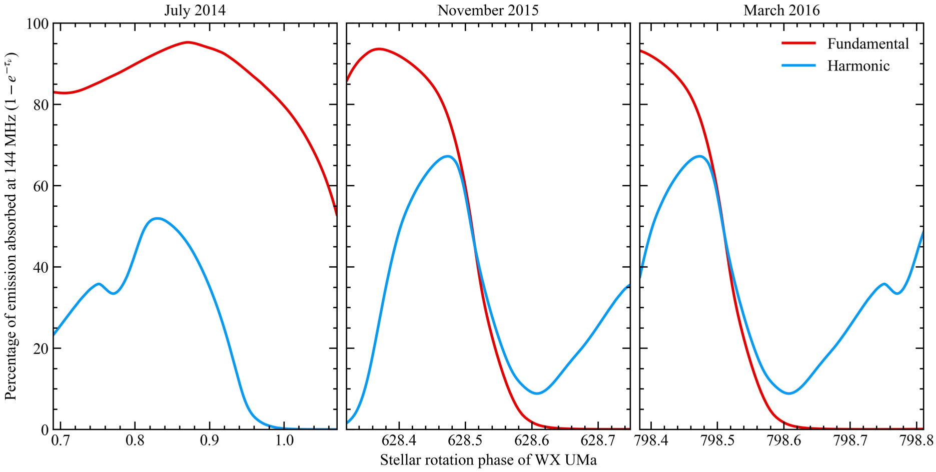

Figure 5.12: The fraction of radio emission induced in WX UMa by a planet at ~ 0.034 au that is absorbed due to free-free processes. Fundamental ECMI is more readily absorbed, as the points generating emission at this mode are more deeply embedded in the stellar wind, resulting in larger optical depths.

Bibliography

Alfvén H., 1941, Arkiv för Matematik, Astronomi och Fysik, 27A

Alfvén H., 1942, Nature, 150, 405

Alvarado-Gómez J. D., Hussain G. A. J., Cohen O., Drake J. J., Garraffo C., Grunhut J., Gombosi T. I., 2016, A&A, 588, A28

Alvarado-Gómez J. D., Garraffo C., Drake J. J., Brown B. P., Oishi J. S., Moschou S. P., Cohen O., 2019, ApJ, 875, L12

Alvarado-Gómez J. D., et al., 2020, ApJ, 895, 47

Andersen J. M., Korhonen H., 2015, MNRAS, 448, 3053

Anglada-Escudé G., et al., 2016, Nature, 536, 437

Badman S. V., Branduardi-Raymont G., Galand M., Hess S. L. G., Krupp N., Lamy L., Melin H., Tao C., 2015, Space Sci. Rev., 187, 99

Bagenal F., 2013, in Oswalt T. D., French L. M., Kalas P., eds, , Planets, Stars and Stellar Systems. Volume 3: Solar and Stellar Planetary Systems. Springer, p. 251, doi:10.1007/978-94-007-5606-9_6

Bastian T. S., Dulk G. A., Leblanc Y., 2000, ApJ, 545, 1058

Beals C. S., 1929, MNRAS, 90, 202

Benz A. O., 2017, Living Reviews in Solar Physics, 14, 2

Bhardwaj A., et al., 2007, Planet. Space Sci., 55, 1135

Biermann L., 1951, Z. Astrophys., 29, 274

Bigg E. K., 1964, Nature, 203, 1008

Bingham R., Cairns R. A., Kellett B. J., 2001, A&A, 370, 1000

Birkeland K., 1908, The Norwegian Aurora Polaris Expedition, 1902-1903. Christiania, H. Aschelhoug & Co.

Blackman E. G., Tarduno J. A., 2018, MNRAS, 481, 5146

Bonfond B., Yao Z., Grodent D., 2020, Journal of Geophysical Research (Space Physics), 125, e28152

Boro Saikia S., Jeffers S. V., Petit P., Marsden S., Morin J., Folsom C. P., 2015, A&A, 573, A17

Boro Saikia S., et al., 2016, A&A, 594, A29

Boro Saikia S., Jin M., Johnstone C. P., Lüftinger T., Güdel M., Airapetian V. S., Kislyakova K. G., Folsom C. P., 2020, A&A, 635, A178

Bourrier V., Lecavelier des Etangs A., 2013, A&A, 557, A124

Bourrier V., Lecavelier des Etangs A., Ehrenreich D., Tanaka Y. A., Vidotto A. A., 2016, A&A, 591, A121

Burn R., Schlecker M., Mordasini C., Emsenhuber A., Alibert Y., Henning T., Klahr H., Benz W., 2021, A&A, 656, A72

Callingham J. R., et al., 2021, Nature Astronomy, 5, 1233

Cameron A. G. W., 1959, ApJ, 130, 916

Carolan S., Vidotto A. A., Loesch C., Coogan P., 2019, MNRAS, 489, 5784

Carolan S., Vidotto A. A., Plavchan P., Villarreal D'Angelo C., Hazra G., 2020, MNRAS, 498, L53

Carolan S., Vidotto A. A., Villarreal D'Angelo C., Hazra G., 2021, MNRAS, 500, 3382

Cauley P. W., Shkolnik E. L., Llama J., Bourrier V., Moutou C., 2018, AJ, 156, 262

Cauley P. W., Shkolnik E. L., Llama J., Lanza A. F., 2019, Nature Astronomy, 3, 1128

Chandran B. D. G., Dennis T. J., Quataert E., Bale S. D., 2011, ApJ, 743, 197

Chiang E., Fung J., 2017, ApJ, 848, 4

Christensen U. R., Holzwarth V., Reiners A., 2009, Nature, 457, 167

Cohen O., 2011, MNRAS, 417, 2592

Cohen O., Kashyap V. L., Drake J. J., Sokolov I. V., Garraffo C., Gombosi T. I., 2011, ApJ, 733, 67

Cohen O., Drake J. J., Glocer A., Garraffo C., Poppenhaeger K., Bell J. M., Ridley A. J., Gombosi T. I., 2014, ApJ, 790, 57

Cowley S. W. H., Bunce E. J., 2001, Planet. Space Sci., 49, 1067

Cox A. N., 2000, Allen's Astrophysical Quantities, 4th edn. Springer, New York, United States of America

Cox J. J., Gibson D. M., 1985, in Hjellming R. M., Gibson D. M., eds, Radio Stars. Springer Netherlands, Dordrecht, pp 233–236

Cuntz M., Saar S. H., Musielak Z. E., 2000, ApJ, 533, L151

Curry S. M., et al., 2015, Geophys. Res. Lett., 42, 9095

Daley-Yates S., Stevens I. R., 2018, MNRAS, 479, 1194

Das B., Chandra P., 2021, ApJ, 921, 9

Das B., Mondal S., Chandra P., 2020, ApJ, 900, 156

Davis I., Vedantham H. K., Callingham J. R., Shimwell T. W., Vidotto A. A., Zarka P., Ray T. P., Drabent A., 2021, A&A, 650, L20

De Pontieu B., et al., 2007, Science, 318, 1574

Desch M. D., Kaiser M. L., 1984, Nature, 310, 755

Deutsch A. J., 1956, ApJ, 123, 210

Deutsch A. J., 1969, in Hack M., ed., Astrophysics and Space Science Library Vol. 13, Mass Loss from Stars. pp 1–14, doi:10.1007/978-94-010-3405-0_1

Donati J. F., Landstreet J. D., 2009, ARA&A, 47, 333

Donati J.-F., Semel M., Carter B. D., Rees D. E., Collier Cameron A., 1997, MNRAS, 291, 658

Donati J. F., et al., 2008a, MNRAS, 385, 1179

Donati J. F., et al., 2008b, MNRAS, 390, 545

Dougherty S. M., Beasley A. J., Claussen M. J., Zauderer B. A., Bolingbroke N. J., 2005, ApJ, 623, 447

Drake S. A., Simon T., Linsky J. L., 1989, ApJS, 71, 905

Dulk G. A., 1985, ARA&A, 23, 169

Dungey J. W., 1961, Phys. Rev. Lett., 6, 47

Eastwood J. P., Hietala H., Toth G., Phan T. D., Fujimoto M., 2015, Space Sci. Rev., 188, 251

Edlén B., 1945, MNRAS, 105, 323

Egan H., Jarvinen R., Ma Y., Brain D., 2019, MNRAS, 488, 2108

Espy P. J., Harris C. R., Steed A. J., Ulwick J. C., Haycocka R. H., Straka R., 1988, Planet. Space Sci., 36, 543

Evensberget D., Carter B. D., Marsden S. C., Brookshaw L., Folsom C. P., Salmeron R., 2022, MNRAS, 510, 5226

Fares R., et al., 2009, MNRAS, 398, 1383

Fares R., et al., 2010, MNRAS, 406, 409

Fares R., et al., 2017, MNRAS, 471, 1246

Faria J. P., et al., 2022, A&A, 658, A115

Feldman W. C., Asbridge J. R., Bame S. J., Gosling J. T., 1977, in White O. R., ed., The Solar Output and its Variation. p. 351

Fichtinger B., Güdel M., Mutel R. L., Hallinan G., Gaidos E., Skinner S. L., Lynch C., Gayley K. G., 2017, A&A, 599, A127

Finley A. J., Hewitt A. L., Matt S. P., Owens M., Pinto R. F., Réville V., 2019, ApJ, 885, L30

Fischer C., Saur J., 2019, ApJ, 872, 113

Folsom C. P., et al., 2018, MNRAS, 481, 5286

Gaia Collaboration et al., 2018, A&A, 616, A1

Gaidos E., Mann A. W., Kraus A. L., Ireland M., 2016, MNRAS, 457, 2877

Gallet F., Bouvier J., 2013, A&A, 556, A36

Garraffo C., Drake J. J., Cohen O., 2016, ApJ, 833, L4

Garraffo C., Drake J. J., Cohen O., Alvarado-Gómez J. D., Moschou S. P., 2017, ApJ, 843, L33

Gibb G. P. S., Mackay D. H., Green L. M., Meyer K. A., 2014, ApJ, 782, 71

Gombosi T. I., van der Holst B., Manchester W. B., Sokolov I. V., 2018, Living Reviews in Solar Physics, 15, 4

Grießmeier J. M., Zarka P., Spreeuw H., 2007, A&A, 475, 359

Grießmeier J.-M., Zarka P., Girard J. N., 2011, Radio Science, 46, RS0F09

Grodent D., 2015, Space Sci. Rev., 187, 23

Grotrian W., 1939, Naturwissenschaften, 27, 214

Güdel M., 2002, ARA&A, 40, 217

Güdel M., 2004, A&ARv, 12, 71

Guedel M., Zlobec P., 1991, A&A, 245, 299

Guillemot L., Octau F., Cognard I., Desvignes G., Freire P. C. C., Smith D. A., Theureau G., Burnett T. H., 2019, A&A, 629, A92

Hall D. S., 1976, in Fitch W. S., ed., Astrophysics and Space Science Library Vol. 60, IAU Colloq. 29: Multiple Periodic Variable Stars. p. 287, doi:10.1007/978-94-010-1175-4_15

Hallinan G., et al., 2015, in American Astronomical Society Meeting Abstracts #225. p. 328.01

Hallinan G., et al., 2021, in Bulletin of the American Astronomical Society. p. 379, doi:10.3847/25c2cfeb.60683360

He F., Wei Y., Wan W., 2020, National Science Review, 7, 1606

Hess S. L. G., Zarka P., 2011, A&A, 531, A29

Hess S., Cecconi B., Zarka P., 2008, Geophys. Res. Lett., 35, L13107

Hollweg J. V., 1986, J. Geophys. Res., 91, 4111

Ip W.-H., Kopp A., Hu J.-H., 2004, ApJ, 602, L53

Jardine M., Collier Cameron A., 2019, MNRAS, 482, 2853

Jin M., Manchester W. B., van der Holst B., Sokolov I., Tóth G., Vourlidas A., de Koning C. A., Gombosi T. I., 2017, ApJ, 834, 172

Johnstone C. P., Güdel M., 2015, A&A, 578, A129

Johnstone C. P., Güdel M., Brott I., Lüftinger T., 2015, A&A, 577, A28

Judge P. G., Solomon S. C., Ayres T. R., 2003, ApJ, 593, 534

Kavanagh R. D., Vidotto A. A., 2020, MNRAS, 493, 1492

Kavanagh R. D., et al., 2019, MNRAS, 485, 4529

Kavanagh R. D., Vidotto A. A., Klein B., Jardine M. M., Donati J.-F., Ó Fionnagáin D., 2021, MNRAS, 504, 1511

Kavanagh R. D., Vidotto A. A., Vedantham H. K., Jardine M. M., Callingham J. R., Morin J., 2022, MNRAS, 514, 675

Kislyakova K. G., Holmström M., Lammer H., Odert P., Khodachenko M. L., 2014, Science, 346, 981

Klein B., Donati J.-F., Hébrard É. M., Zaire B., Folsom C. P., Morin J., Delfosse X., Bonfils X., 2021a, MNRAS, 500, 1844

Klein B., et al., 2021b, MNRAS, 502, 188

Klein B., et al., 2022, MNRAS, 512, 5067

Kochukhov O., 2021, A&ARv, 29, 1

Kopparapu R. K., et al., 2013, ApJ, 765, 131

Kosirev N. A., 1934, MNRAS, 94, 430

Kulikov Y. N., Lammer H., Lichtenegger H. I. M., Penz T., Breuer D., Spohn T., Lundin R., Biernat H. K., 2007, Space Sci. Rev., 129, 207

Lamers H. J. G. L. M., Cassinelli J. P., 1999, Introduction to Stellar Winds. Cambridge University Press, Cambridge, doi:10.1017/CBO9781139175012

Lamy L., 2020, Philosophical Transactions of the Royal Society of London Series A, 378, 20190481

Lamy L., Zarka P., Cecconi B., Prangé R., 2010, Journal of Geophysical Research (Space Physics), 115, A09221

Lanza A. F., 2009, A&A, 505, 339

Lanza A. F., 2012, A&A, 544, A23

Lanza A. F., Boisse I., Bouchy F., Bonomo A. S., Moutou C., 2011, A&A, 533, A44

Lavail A., Kochukhov O., Wade G. A., 2018, MNRAS, 479, 4836

Lazio T. J. W., Carmichael S., Clark J., Elkins E., Gudmundsen P., Mott Z., Szwajkowski M., Hennig L. A., 2010a, AJ, 139, 96

Lazio T. J. W., Shankland P. D., Farrell W. M., Blank D. L., 2010b, AJ, 140, 1929

Lecavelier des Etangs A., et al., 2012, A&A, 543, L4

Lecavelier des Etangs A., Sirothia S. K., Gopal-Krishna Zarka P., 2013, A&A, 552, A65

Leto P., Trigilio C., Buemi C. S., Umana G., Ingallinera A., Cerrigone L., 2016, MNRAS, 459, 1159

Leto P., Trigilio C., Buemi C. S., Umana G., Ingallinera A., Cerrigone L., 2017, MNRAS, 469, 1949

Leto P., et al., 2019, MNRAS, 482, L4

Leto P., et al., 2021, MNRAS, 507, 1979

Linsky J. L., Drake S. A., Bastian T. S., 1992, ApJ, 393, 341

Llama J., Wood K., Jardine M., Vidotto A. A., Helling C., Fossati L., Haswell C. A., 2011, MNRAS, 416, L41

Llama J., Vidotto A. A., Jardine M., Wood K., Fares R., Gombosi T. I., 2013, MNRAS, 436, 2179

Llama J., Jardine M. M., Wood K., Hallinan G., Morin J., 2018, ApJ, 854, 7

Lo K. K., et al., 2012, MNRAS, 421, 3316

Lomb N. R., 1976, Ap&SS, 39, 447

Louis C. K., Lamy L., Zarka P., Cecconi B., Hess S. L. G., 2017, Journal of Geophysical Research (Space Physics), 122, 9228

Mahadevan S., et al., 2021, ApJ, 919, L9

Martioli E., et al., 2020, A&A, 641, L1

Martioli E., Hébrard G., Correia A. C. M., Laskar J., Lecavelier des Etangs A., 2021, A&A, 649, A177

Mayor M., Queloz D., 1995, Nature, 378, 355

McIntosh S. W., de Pontieu B., Carlsson M., Hansteen V., Boerner P., Goossens M., 2011, Nature, 475, 477

McIvor T., Jardine M., Holzwarth V., 2006, MNRAS, 367, L1

Melrose D. B., 2006, ApJ, 637, 1113

Melrose D. B., Dulk G. A., 1982, ApJ, 259, 844

Meyer K. A., Mackay D. H., van Ballegooijen A. A., Parnell C. E., 2013, Sol. Phys., 286, 357

Mittag M., Robrade J., Schmitt J. H. M. M., Hempelmann A., González-Pérez J. N., Schröder K. P., 2017, A&A, 600, A119

Morin J., et al., 2008a, MNRAS, 384, 77

Morin J., et al., 2008b, MNRAS, 390, 567

Morin J., Donati J. F., Petit P., Delfosse X., Forveille T., Jardine M. M., 2010, MNRAS, 407, 2269

Narang M., et al., 2021, MNRAS, 500, 4818

Neubauer F. M., 1980, J. Geophys. Res., 85, 1171

Neugebauer M., Snyder C. W., 1966, J. Geophys. Res., 71, 4469

Newton E. R., Irwin J., Charbonneau D., Berlind P., Calkins M. L., Mink J., 2017, ApJ, 834, 85

Nichols J. D., Milan S. E., 2016, MNRAS, 461, 2353

Nichols J. D., Burleigh M. R., Casewell S. L., Cowley S. W. H., Wynn G. A., Clarke J. T., West A. A., 2012, ApJ, 760, 59

Nicholson B. A., et al., 2016, MNRAS, 459, 1907

Ó Fionnagáin D., Vidotto A. A., 2018, MNRAS, 476, 2465

Ó Fionnagáin D., et al., 2019a, MNRAS, 483, 873

Ó Fionnagáin D., et al., 2019b, MNRAS, 487, 3079

Ó Fionnagáin D., Vidotto A. A., Petit P., Neiner C., Manchester W. I., Folsom C. P., Hallinan G., 2021, MNRAS, 500, 3438

O'Gorman E., Coughlan C. P., Vlemmings W., Varenius E., Sirothia S., Ray T. P., Olofsson H., 2018, A&A, 612, A52

Owocki S. P., Shultz M. E., ud-Doula A., Chandra P., Das B., Leto P., 2022, MNRAS, 513, 1449

Panagia N., Felli M., 1975, A&A, 39, 1

Paresce F., 1979, J. Geophys. Res., 84, 4409

Parker E. N., 1958, ApJ, 128, 664

Parker E. N., 1960, ApJ, 132, 821

Pauls H. L., Zank G. P., Williams L. L., 1995, J. Geophys. Res., 100, 21595

Pérez-Torres M., et al., 2021, A&A, 645, A77

Perger M., et al., 2021, A&A, 649, L12

Peterson D. M., et al., 2006, ApJ, 636, 1087

Petit P., et al., 2008, MNRAS, 388, 80

Pevtsov A. A., Fisher G. H., Acton L. W., Longcope D. W., Johns-Krull C. M., Kankelborg C. C., Metcalf T. R., 2003, ApJ, 598, 1387

Pillitteri I., Günther H. M., Wolk S. J., Kashyap V. L., Cohen O., 2011, ApJ, 741, L18

Plavchan P., Werner M. W., Chen C. H., Stapelfeldt K. R., Su K. Y. L., Stauffer J. R., Song I., 2009, ApJ, 698, 1068

Plavchan P., et al., 2020, Nature, 582, 497

Polzin E. J., Breton R. P., Stappers B. W., Bhattacharyya B., Janssen G. H., Osłowski S., Roberts M. S. E., Sobey C., 2019, MNRAS, 490, 889

Pope B. J. S., Withers P., Callingham J. R., Vogt M. F., 2019, MNRAS, 484, 648

Powell K. G., Roe P. L., Linde T. J., Gombosi T. I., De Zeeuw D. L., 1999, Journal of Computational Physics, 154, 284

Pryor W. R., et al., 2011, Nature, 472, 331

Puls J., Vink J. S., Najarro F., 2008, A&ARv, 16, 209

Reiners A., Basri G., 2009, A&A, 496, 787

Réville V., Brun A. S., 2017, ApJ, 850, 45

Réville V., Brun A. S., Matt S. P., Strugarek A., Pinto R. F., 2015, ApJ, 798, 116

Roberts M. S. E., 2011, in Burgay M., D'Amico N., Esposito P., Pellizzoni A., Possenti A., eds, American Institute of Physics Conference Series Vol. 1357, American Institute of Physics Conference Series. pp 127–130 (`arXiv:1103.0819`), doi:10.1063/1.3615095

Rodríguez L. F., Lizano S., Loinard L., Chávez-Dagostino M., Bastian T. S., Beasley A. J., 2019, ApJ, 871, 172

Rubenstein E. P., Schaefer B. E., 2000, ApJ, 529, 1031

Rybicki G. B., Lightman A. P., 1986, Radiative Processes in Astrophysics, 1st edn. Wiley-VCH, Weinheim, Germany

Saar S. H., Cuntz M., 2001, MNRAS, 325, 55

Saur J., Neubauer F. M., Connerney J. E. P., Zarka P., Kivelson M. G., 2004, Plasma interaction of Io with its plasma torus. Cambridge University Press, pp 537–560

Saur J., Grambusch T., Duling S., Neubauer F. M., Simon S., 2013, A&A, 552, A119

Saur J., Willmes C., Fischer C., Wennmacher A., Roth L., Youngblood A., Strobel D. F., Reiners A., 2021, A&A, 655, A75

Scargle J. D., 1982, ApJ, 263, 835

Schmitt J. H. M. M., Liefke C., 2004, A&A, 417, 651

Schmitt J. H. M. M., Golub L., Harnden F. R. J., Maxson C. W., Rosner R., Vaiana G. S., 1985, ApJ, 290, 307

See V., et al., 2019, ApJ, 876, 118

Semel M., 1989, A&A, 225, 456

Shimwell T. W., et al., 2017, A&A, 598, A104

Shkolnik E., Walker G. A. H., Bohlender D. A., 2003, ApJ, 597, 1092

Shkolnik E., Walker G. A. H., Bohlender D. A., Gu P. G., Kürster M., 2005, ApJ, 622, 1075

Shkolnik E., Bohlender D. A., Walker G. A. H., Collier Cameron A., 2008, ApJ, 676, 628

Shulyak D., Reiners A., Engeln A., Malo L., Yadav R., Morin J., Kochukhov O., 2017, Nature Astronomy, 1, 0184

Shulyak D., et al., 2019, A&A, 626, A86

Sirothia S. K., Lecavelier des Etangs A., Gopal-Krishna Kantharia N. G., Ishwar-Chandra C. H., 2014, A&A, 562, A108

Smith A. M. S., Collier Cameron A., Greaves J., Jardine M., Langston G., Backer D., 2009, MNRAS, 395, 335

Sokolov I. V., et al., 2013, ApJ, 764, 23

Stallard T. S., et al., 2019, Philosophical Transactions of the Royal Society of London Series A, 377, 20180405

Stassun K. G., Collins K. A., Gaudi B. S., 2017, AJ, 153, 136

Stepanov A. V., Kliem B., Zaitsev V. V., Fürst E., Jessner A., Krüger A., Hildebrandt J., Schmitt J. H. M. M., 2001, A&A, 374, 1072

Stern D. P., 1989, Reviews of Geophysics, 27, 103

Strugarek A., Brun A. S., Donati J. F., Moutou C., Réville V., 2019, ApJ, 881, 136

Tóth G., et al., 2012, Journal of Computational Physics, 231, 870

Treumann R. A., 2006, A&ARv, 13, 229

Trigilio C., Leto P., Leone F., Umana G., Buemi C., 2000, A&A, 362, 281

Trigilio C., Leto P., Umana G., Leone F., Buemi C. S., 2004, A&A, 418, 593

Trigilio C., Leto P., Umana G., Buemi C. S., Leone F., 2011, ApJ, 739, L10

Turner J. D., Grießmeier J.-M., Zarka P., Vasylieva I., 2019, A&A, 624, A40

Turner J. D., et al., 2021, A&A, 645, A59

Turnpenney S., Nichols J. D., Wynn G. A., Burleigh M. R., 2018, ApJ, 854, 72

Uchida Y., Sakurai T., 1983, in Byrne P. B., Rodono M., eds, Astrophysics and Space Science Library Vol. 102, IAU Colloq. 71: Activity in Red-Dwarf Stars. pp 629–632, doi:10.1007/978-94-009-7157-8_90

Van Doorsselaere T., Wardle N., Del Zanna G., Jansari K., Verwichte E., Nakariakov V. M., 2011, ApJ, 727, L32

Van Haarlem M. P., et al., 2013, A&A, 556, A2

Varela J., Réville V., Brun A. S., Zarka P., Pantellini F., 2018, A&A, 616, A182

Vedantham H. K., 2021, MNRAS, 500, 3898

Vedantham H. K., et al., 2020, Nature Astronomy, 4, 577

Verscharen D., Klein K. G., Maruca B. A., 2019, Living Reviews in Solar Physics, 16, 5

Vidotto A. A., 2021, Living Reviews in Solar Physics, 18, 3

Vidotto A. A., Bourrier V., 2017, MNRAS, 470, 4026

Vidotto A. A., Cleary A., 2020, MNRAS, 494, 2417

Vidotto A. A., Donati J.-F., 2017, A&A, 602, A39

Vidotto A. A., Jardine M., Helling C., 2010, ApJ, 722, L168

Vidotto A. A., Fares R., Jardine M., Donati J.-F., Opher M., Moutou C., Catala C., Gombosi T. I., 2012, MNRAS, 423, 3285

Vidotto A. A., Jardine M., Morin J., Donati J. F., Lang P., Russell A. J. B., 2013, A&A, 557, A67

Vidotto A. A., et al., 2014, MNRAS, 441, 2361

Vidotto A. A., Fares R., Jardine M., Moutou C., Donati J. F., 2015, MNRAS, 449, 4117

Vidotto A. A., et al., 2016, MNRAS, 455, L52

Vidotto A. A., Feeney N., Groh J. H., 2019, MNRAS, 488, 633

Villadsen J., Hallinan G., Bourke S., Güdel M., Rupen M., 2014, ApJ, 788, 112

Weber E. J., Davis Leverett J., 1967, ApJ, 148, 217

Weber C., Erkaev N. V., Ivanov V. A., Odert P., Grießmeier J.-M., Fossati L., Lammer H., Rucker H. O., 2018, MNRAS, 480, 3680

Wood B. E., 2004, Living Reviews in Solar Physics, 1, 2

Wood B. E., 2018, in Journal of Physics Conference Series. p. 012028 (`arXiv:1809.01109`), doi:10.1088/1742-6596/1100/1/012028

Wood B. E., Alexander W. R., Linsky J. L., 1996, ApJ, 470, 1157

Wood B. E., Linsky J. L., Müller H.-R., Zank G. P., 2001, ApJ, 547, L49

Wood B. E., et al., 2021, ApJ, 915, 37

Wright A. E., Barlow M. J., 1975, MNRAS, 170, 41

Wright J. T., Howard A. W., 2009, ApJS, 182, 205

Zaghoo M., Collins G. W., 2018, ApJ, 862, 19

Zaitsev V. V., Stepanov A. V., 1983, Sol. Phys., 88, 297

Zarka P., 1998, J. Geophys. Res., 103, 20159

Zarka P., 2004, Planet. Space Sci., 52, 1455

Zarka P., 2007, Planet. Space Sci., 55, 598

Zarka P., Treumann R. A., Ryabov B. P., Ryabov V. B., 2001, Ap&SS, 277, 293

Zarka P., Cecconi B., Kurth W. S., 2004, Journal of Geophysical Research (Space Physics), 109, A09S15

Zarka P., Magalhães F. P., Marques M. S., Louis C. K., Echer E., Lamy L., Cecconi B., Prangé R., 2021, Journal of Geophysical Research (Space Physics), 126, e29780

de Gasperin F., Lazio T. J. W., Knapp M., 2020, A&A, 644, A157

van der Holst B., Sokolov I. V., Meng X., Jin M., Manchester W. B. I., Tóth G., Gombosi T. I., 2014, ApJ, 782, 81

Summary

Low-mass main-sequence stars like our Sun are continuous sources of outflowing hot magnetised plasma. In the case of the Sun, this is known as the *solar wind*, whereas for other stars they are called *stellar winds*. These types of stars comprise 93% of all stars in our galaxy, and also host the bulk of all exoplanets discovered to date. Therefore, understanding their wind outflows and how they interact with the planets they host is crucial to assessing the long-term evolution of planetary atmospheres, which in turn determines their potential to support life as we know it. The interactions between stellar winds and planets can also produce signals which could be detected with current-generation telescopes.

Current measurements of the winds of low-mass main-sequence stars are limited, and have only been successful in a handful of cases. However, by coupling state-of-the-art magnetohydrodynamic (MHD) models of stellar winds with observational constraints, 3-dimensional snapshots of the wind environments around planet-hosting stars can be obtained. In this thesis, I utilise such models to explore the winds of these stars, and predict the potentially-observable signatures that may arise from their interactions with orbiting planets.

Finding exoplanets with radio telescopes

Analogous of what is observed for the magnetised planets in the solar system, planets orbiting around other stars are expected to exhibit auroral emission at their magnetic poles, particularly at radio wavelengths. Such emission is thought to be generated via the interaction between the planet's own magnetic field and the wind of its host star. If detectable, the emission emanating from the planet's magnetic poles could provide a new window for discovering exoplanets.

The winds of low-mass main sequence stars are predominantly composed of hot magnetised hydrogen, which can strongly absorb the low frequency radio emission that exoplanets are thought to emit at. As a result, if the wind of the host star is very dense, radio emission from the planet may be difficult to detect. Therefore, understanding the stellar wind environment of planet-hosting stars is crucial to determining if radio emission from planets can be detected from Earth.

From our understanding of the auroral emission of the solar system planets, radio emission from exoplanets is expected to be stronger for those with larger radii and smaller orbits. Coincidentally, such planets dominate the current population

of known exoplanets. As their presence produces stronger signatures from their host stars, they are more favourable for detection via traditional methods. These planets are known as ‘hot Jupiters’, which are roughly the size of Jupiter and orbit very close to their host stars.

HD189733b is a well-known hot Jupiter, which orbits its host star at about 3 percent of the distance between the Earth and the Sun. The host star is also very active, and is likely to drive a wind that is much stronger in comparison to the solar wind. As a result, HD189733b has been of particular interest in the context of exoplanetary radio emission. Using a state-of-the-art 3-dimensional magnetohydrodynamics code, in Chapter 2 I simulate the stellar wind of the host star of HD189733b. This model is based on observationally-derived magnetic field maps for the star, which are a key input for these models. I then use the results of the stellar wind model to estimate the frequency and strength of the radio emission for the planet.

The wind of the host star is expected to be quite dense, so it will absorb a large fraction of the radio emission from HD189733b. In Chapter 2, I show that this effect is least pronounced when the planet is near conjunction of the host star, the point in its orbit where it is closest to the observer. The geometry of a planet in conjunction is shown in Figure I. This result illustrates that detection of radio emission from any exoplanet is most favourable when it is near conjunction, which can be used to guide future observations in search of such emission. Outside of conjunction, the exoplanet is said to be ‘eclipsed’ by the wind of its host star at radio wavelengths, becoming undetectable.

Exoplanets as probes of stellar winds

(i) Radio eclipses of exoplanets

With the concept of radio eclipses of exoplanets established, the next question I asked myself during this thesis was: how do the properties of the stellar wind and geometry of the planetary orbit affect the duration and severity of the eclipse? If we can determine this, we can in theory reverse-engineer observations of exoplanetary radio emission to study the winds of planet-hosting stars.

The 3-dimensional numerical models utilised in Chapter 2 are computationally expensive and time-consuming, and therefore their uses are generally limit to specific cases. As a result, they are not well-suited for parametric studies such as that described above. Simpler models that retain the key physical processes however can be deployed for this. With this in mind, in Chapter 3 I develop a 1-dimensional stellar wind model, which I then couple to another physical model that describes the propagation and absorption of low-frequency radio emission through stellar winds. This model is very fast and flexible, and provides the percentage of exoplanetary radio emission that escapes through the wind of the host star as a function of time, for any set of stellar wind and orbital properties.

Using this model, in Chapter 3 I first illustrate the effects of the stellar wind mass-loss rate and temperature on the duration of the radio eclipse. I find that

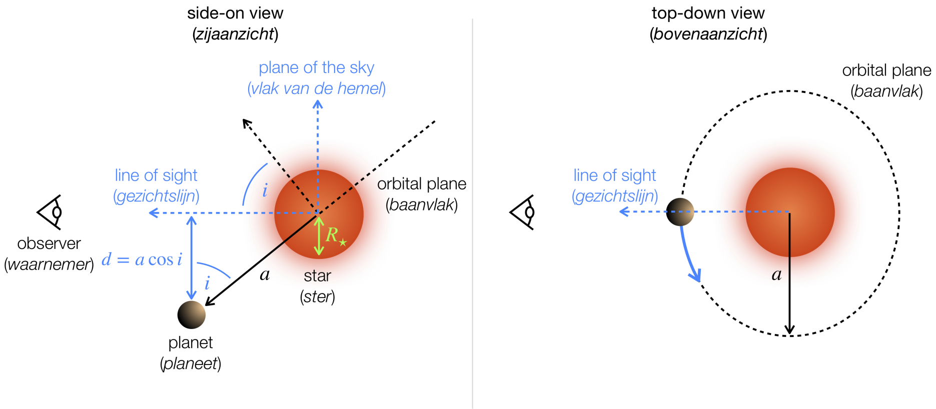

Figure I: *English:* Sketch illustrating the geometry of an exoplanet's orbit around its host star, with an orbital distance a and inclination i. When the planet is closest to the observer, it is said to be in 'conjunction'. In Chapter 2, I show that such a scenario provides the most favourable conditions for detecting exoplanets at radio wavelengths. Note that in the case where d is less than the stellar radius $R_\star$, the planet is said to 'transit' the star (neglecting the size of the planet itself), where it periodically blocks a fraction of the starlight. *Nederlands:* Schets ter illustratie van de geometrie van de baan van een exoplaneet rond zijn moederster, met een baanafstand a en inclinatie i. Wanneer de planeet het dichtst bij de waarnemer is, wordt gezegd dat deze in 'conjunctie' is. In Hoofdstuk 2 laat ik zien dat een dergelijk scenario de gunstigste omstandigheden biedt voor het detecteren van exoplaneten op radiogolflengten. Merk op dat in het geval dat d kleiner is dan de stellaire straal $R_\star$, de planeet de ster 'overgaat' (waarbij de grootte van de planeet zelf verwaarloosd wordt), waar hij periodiek een fractie van het sterlicht blokkeert.

stars with hot, low mass-loss rate winds present more favourable conditions for detecting radio emission from their orbiting planets. In terms of the orbit of the planet itself, transiting exoplanets experience the largest modulation to their radio emission, being most visible during transit of the stellar disk. Additionally, planets orbiting further from their host stars are more easily detected. I then apply the model to the hot Jupiter host τ Boo, showing that the stellar wind properties of planet-hosting stars can be constrained by the morphology of the radio eclipse. Specifically, the duration of time where a specific fraction of the exoplanetary radio emission escapes the system can be directly linked to a combination of stellar wind temperature and mass-loss rate. This provides a potential new method for estimating the properties of the winds of planet-hosting stars, which so far has only been successful in a handful of cases.

(ii) Magnetic star-planet interactions

Exoplanetary radio emission is not the only avenue for studying the winds of low-mass stars, nor is it the only type of radio emission thought to occur due to the presence of planets. Another mechanism that is thought to generate bright radio emission in exoplanetary systems is via the perturbation of the star's own magnetic field due to the motion of the planet, generally referred to as magnetic star-planet interactions (for details see Section 1.5). A key distinction between this and exoplanetary radio emission is that the emission occurs near/on the star itself, as opposed to on the planet. Another thing of note is that the emission is thought to occur at higher frequencies compared to that expected for exoplanets, as these stars can harbour surface magnetic fields that are three orders of magnitude larger than what is seen on the Sun. This is a proposed explanation for the lack of conclusive detections of exoplanetary radio emission, in that it may be generated at a frequency that is too low to penetrate the Earth's atmosphere.

Around all magnetised stars exists a region known as the Alfvén surface, inside which magnetic forces dominate over thermal forces in the solar wind plasma. Inside the Alfvén surface, radio emission can be generated near the star via the perturbation of the star's magnetic field by an orbiting planet. M dwarf stars are of particular interest in this regard, in that they exhibit very strong surface magnetic fields, which are likely to result in large Alfvén surfaces that can enclose a wide range of planetary orbits. Additionally, stars with low stellar wind mass-loss rates tend to have large Alfvén surfaces. For an illustrative sketch, see Figure II.

The two nearby M dwarfs Proxima Centauri (Prox Cen) and AU Microscopii (AU Mic) present potentially suitable conditions for magnetic star-planet interactions to occur. Both stars exhibit strong magnetic fields at their surfaces, and are hosts to multiple confirmed planets. In the case of Prox Cen, recent radio observations may be indicative of that such interactions occurring. In order to assess the viability for magnetic star-planet interactions occurring on these stars, knowing the location of their Alfvén surfaces relative to the planetary orbits is key.

To determine the location of the Alfvén surfaces of Prox Cen and AU Mic, in Chapter 4 I utilise magnetohydrodynamic models similar to those used in Chapter 2 to obtain 3-dimensional snapshots of their stellar wind environments. These

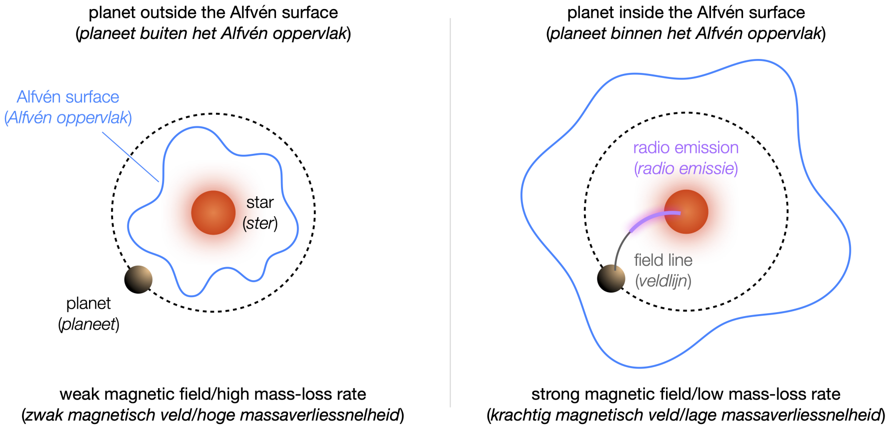

Figure II: *English:* Sketch illustrating the conditions for magnetic star-planet interactions to occur. If the star has a weak magnetic field or a high stellar wind mass-loss rate, planets are unlikely to orbit inside the Alfvén surface (left panel). However, in the case where the host star has a strong magnetic field or low stellar wind mass-loss rate, the Alfvén surface becomes very large, potentially enclosing a wide range of planetary orbits (right panel). When inside the Alfvén surface, the planet can induce the generation of strong radio emission along the magnetic field line that connects it to the star. *Nederlands:* Schets die de voorwaarden illustreert voor het optreden van magnetische ster-planeet-interacties. Als de ster een zwak magnetisch veld heeft of een hoge massaverliessnelheid, is het onwaarschijnlijk dat planeten binnen het Alfvén-oppervlak (linker paneel) draaien. In het geval dat de moederster echter een sterk magnetisch veld heeft of een lage massaverliessnelheid door stellaire wind, wordt het Alfvén-oppervlak erg groot en kan het een breed scala aan planetaire banen insluiten (rechterpaneel). Als de planeet zich binnen het Alfvén-oppervlak bevindt, kan ze sterke radiostraling opwekken langs de magnetische veldlijn die haar met de ster verbindt.

models were constrained using observational data, and the wind properties obtained from them allow for the location of the Alfvén surface to be determined. In the case of Prox Cen, which has an estimated upper-limit for its mass-loss rate, I show that magnetic star-planet interactions are unlikely to occur. For AU Mic however, its mass-loss rate is relatively unconstrained. By varying its mass-loss rate, I illustrate that there is a certain value which places both known planets inside the Alfvén surface. Therefore, if signatures of magnetic star-planet interactions are detected from AU Mic, an upper limit can be placed on its mass-loss rate. This illustrates that the winds of stars can be studied from the detection of magnetic star-planet interactions, complementing the results of Chapter 3.

New methods for identifying potential planet-hosting stars

It is clear that known exoplanetary systems can be studied with using sophisticated magnetohydrodynamic models to assess if different types of star-planet interactions can occur. However, in the case where a signature of such interactions is detected from a star with no known exoplanets, how do we determine if it is of a planetary origin? This is challenging for very active stars. Particularly in the case of smaller planets, the types of signals they induce on the star which are traditionally used to find exoplanets are drowned out by the stellar activity. Therefore, new theoretical models are needed to interpret such signatures, particularly at radio wavelengths.

Recent wide-field radio surveys have begun to detect potential hints of magnetic star-planet interactions from M dwarfs in the Northern sky. So far, none of these stars are confirmed to host any planets. However, WX UMa, a star in the sample of M dwarfs detected at radio wavelengths, has previously had its surface magnetic field mapped. Therefore, a realistic stellar wind environment can be constructed for the star, which in turn allows us to determine the size of its Alfvén surface.

In Chapter 5, I first present a stellar wind model obtained for WX UMa based on its previously-published magnetic field map. I then develop a model that is the first of its kind, which predicts the morphology of the radio emission generated from the star via magnetic interactions with an orbiting planet. Applying the model to WX UMa, I illustrate with this model that its observed emission is best-reproduced by a Neptune-sized planet orbiting the star around every 7 days. While alternative emission mechanisms cannot currently be ruled out for WX UMa, its application exhibits its exciting potential for identifying planet-host candidates from upcoming radio observations.

Samenvatting (Dutch summary)

Lichte hoofdreekssterren zoals onze Zon, zijn bronnen van continue uitstromend heet gemagnetiseerd plasma. In het geval van de Zon staat dit bekend als de zonnewind, terwijl het voor andere sterren *sterrenwinden* worden genoemd. Dit soort sterren omvat 93% van alle sterren in onze Melkweg, en herbergt ook het grootste deel van de exoplaneten die tot nu toe zijn ontdekt. Daarom is het cruciaal om inzicht te krijgen in hun sterrenwind en hoe ze omgaan met de planeten die ze huisvesten om de langetermijnevolutie van planetaire atmosferen te beoordelen, wat op zijn beurt hun potentieel bepaalt om leven zoals wij dat kennen te ondersteunen. De interacties tussen stellaire winden en planeten kunnen ook signalen produceren die kunnen worden gedetecteerd met telescopen van de huidige generatie.

De huidige metingen van de wind van lichte hoofdreekssterren zijn beperkt en zijn slechts in een handvol gevallen succesvol geweest. Echter, door moderne magnetohydrodynamische (MHD) modellen van sterrenwinden te koppelen aan observatiebeperkingen, kunnen driedimensionale snapshots van de windomgevingen rond sterren met planeten worden verkregen. In dit proefschrift gebruik ik dergelijke modellen om de winden van deze sterren te onderzoeken en de potentieel waarneembare kenmerken te voorspellen die kunnen ontstaan door hun interacties met hun planeten.

Exoplaneten vinden met radiotelescopen

Analoog aan wat wordt waargenomen voor de gemagnetiseerde planeten in het zonnestelsel, wordt verwacht dat planeten die rond andere sterren draaien, poollichtstraling vertonen aan hun magnetische polen, vooral bij radiogolflengten. Men denkt dat dergelijke emissie wordt gegenereerd via de interactie tussen het eigen magnetische veld van de planeet en de wind van zijn moederster. Indien detecteerbaar, zou de emissie afkomstig van de magnetische polen van de planeet een nieuw venster kunnen bieden voor het ontdekken van exoplaneten.

De winden van lichte hoofdreekssterren bestaan voornamelijk uit heet gemagnetiseerd waterstof, die de laagfrequente radio-emissie die exoplaneten zouden uitzenden sterk kan absorberen. Als gevolg hiervan, als de wind van de gastster erg dicht is, kan radio-emissie van de planeet moeilijk te detecteren zijn. Daarom is het van cruciaal belang om de stellaire windomgeving van planeet herbergende sterren te begrijpen om te bepalen of radio-emissie van planeten vanaf de Aarde kan worden gedetecteerd.

Op basis van ons begrip van de poollichtemissie van de planeten binnen ons zonnestelsel, wordt verwacht dat de radio-emissie sterker zal zijn voor exoplaneten met grotere diameters en kleinere banen. Toevallig domineren dergelijke planeten de huidige populatie van bekende exoplaneten. Omdat hun aanwezigheid sterkere kenmerken van hun moedersterren produceert, zijn ze gunstiger voor detectie via traditionele methoden. Deze planeten staan bekend als 'hete Jupiters', die ongeveer zo groot zijn als Jupiter en heel dicht om hun moedersterren draaien.

HD189733b is een bekende hete Jupiter, die om zijn moederster draait op ongeveer 3 procent van de afstand tussen de Aarde en de Zon. De gastster is ook erg actief en drijft waarschijnlijk een wind aan die heel sterk is in vergelijking met de zonnewind. Als gevolg hiervan is HD189733b van bijzonder belang geweest in de context van exoplanetaire radio-emissie. Met behulp van een moderne 3-dimensionale magnetohydrodynamische code, simuleer ik in Hoofdstuk 2 de stellaire wind van de moederster van HD189733b. Dit model is gebaseerd op van waarnemingen afgeleide magnetische veldkaarten voor de ster, die een belangrijke input vormen voor deze modellen. Vervolgens gebruik ik de resultaten van het stellaire windmodel om de frequentie en sterkte van de radio-emissie van de planeet te schatten.

De wind van de gastster is naar verwachting behoorlijk dicht, dus het zal een groot deel van de radio-emissie van HD189733b absorberen. In Hoofdstuk 2 laat ik zien dat dit effect het minst uitgesproken is wanneer de planeet zich in de buurt van de conjunctie van de moederster bevindt, het punt in zijn baan waar hij zich het dichtst bij de waarnemer bevindt. De geometrie van een planeet in conjunctie wordt getoond in Figuur I. Dit resultaat illustreert dat detectie van radio-emissie van een exoplaneet het gunstigst is wanneer deze nabij conjunctie is, wat kan worden gebruikt als leidraad voor toekomstige waarnemingen op zoek naar dergelijke emissie. Buiten de conjunctie zou de exoplaneet 'verduisterd' worden door de wind van zijn moederster op radiogolflengten en ondetecteerbaar worden, dit wordt ook wel een eclips genoemd.

Exoplaneten als sondes van stellaire winden

(i) Radioeclipsen van exoplaneten

Met het concept van radioeclipsen van exoplaneten vastgesteld, was de volgende vraag die ik mezelf tijdens dit proefschrift stelde: hoe beïnvloeden de eigenschappen van de stellaire wind en de geometrie van de planetaire baan de duur en ernst van de eclips? Als we dit kunnen bepalen, kunnen we in theorie waarnemingen van exoplanetaire radiostraling terugleiden om de winden van sterren die planeten herbergen te bestuderen.

De driedimensionale numerieke modellen die in Hoofdstuk 2 worden gebruikt, zijn rekenkundig duur en tijdrovend, en daarom is hun gebruik over het algemeen beperkt tot specifieke gevallen. Als gevolg hiervan zijn ze niet erg geschikt voor parametrische studies zoals hierboven beschreven. Hiervoor kunnen echter eenvoudiger modellen worden ingezet die de belangrijkste fysieke processen behouden. Met dit in gedachten ontwikkel ik in Hoofdstuk 3 een 1-dimensionaal stellair windmodel, dat ik vervolgens koppel aan een ander fysiek model dat de voortplanting en absorptie van laagfrequente radio-emissie door stellaire winden beschrijft. Dit model is erg snel en flexibel en levert het percentage exoplanetaire radiostraling dat ontsnapt door de wind van de gastster als functie van de tijd, voor elke set van stellaire wind- en baaneigenschappen.

Met behulp van dit model illustreer ik in Hoofdstuk 3 eerst de effecten van de snelheid van massaverlies en de temperatuur van de stellaire wind op de duur van de radioverduistering. Ik vind dat sterren met hete winden een lage snelheid van massaverlies gunstigere omstandigheden bieden voor het detecteren van radio-emissie van hun planeten. In termen van de baan van de planeet zelf ervaren transiterende exoplaneten de grootste modulatie van hun radio-emissie, en zijn ze het meest zichtbaar tijdens de overgang van de stellaire schijf. Bovendien worden planeten die verder van hun moedersterren draaien gemakkelijker gedetecteerd. Vervolgens pas ik het model toe op de hete Jupiter-gastheer τ Boo, wat aantoont dat de eigenschappen van de stellaire wind van sterren die planeten herbergen kunnen worden beperkt door de morfologie van de radio eclips. Met name de tijdsduur waarin een specifieke fractie van de exoplanetaire radio-emissie aan het systeem ontsnapt, kan direct worden gekoppeld aan een combinatie van stellaire windtemperatuur en de snelheid van massaverlies. Dit biedt een potentieel nieuwe methode voor het schatten van de eigenschappen van de winden van sterren die planeten herbergen, die tot nu toe slechts in een handvol gevallen succesvol zijn geweest.

(ii) Magnetische ster-planeet interacties

Exoplanetaire radio-emissie is niet de enige manier om de winden van sterren met een lage massa te bestuderen, en het is ook niet het enige type radio-emissie waarvan wordt aangenomen dat het optreedt als gevolg van de aanwezigheid van planeten. Een ander mechanisme waarvan wordt gedacht dat het heldere radio-emissie genereert in exoplanetaire systemen, is via de verstoring van het eigen magnetische veld van de ster als gevolg van de beweging van de planeet, in het algemeen magnetische ster-planeet interacties genoemd (zie voor details Paragraaf 1.5). Een belangrijk onderscheid tussen deze en exoplanetaire radio-emissie is dat de emissie dichtbij/op de ster zelf plaatsvindt, in tegenstelling tot op de planeet. Iets anders wat opvalt, is dat men denkt dat de emissie plaatsvindt bij hogere frequenties in vergelijking met de frequenties die worden verwacht voor exoplaneten, aangezien deze sterren magnetische velden aan het oppervlak kunnen bevatten die drie orden van grootte sterker zijn dan wat op de Zon wordt waargenomen. Dit is een voorgestelde verklaring voor het ontbreken van sluitende detecties van exoplanetaire radio-emissie, in die zin dat het een te lage frequentie heeft om de atmosfeer van de Aarde binnen te dringen.

Rond alle gemagnetiseerde sterren bestaat een gebied dat bekend staat als het Alfv'en-oppervlak, waarbinnen magnetische krachten domineren over thermische krachten in het zonnewindplasma. Binnen het Alfvén-oppervlak kan radio-emissie worden gegenereerd in de buurt van de ster via de verstoring van het magnetische veld van de ster door een in een baan om de ster draaiende planeet. M dwergsterren zijn in dit opzicht van bijzonder belang, omdat ze zeer sterke magnetische velden aan het oppervlak vertonen, wat waarschijnlijk zal resulteren in grote Alfv'en-oppervlakken die een breed scala aan planetaire banen kunnen omsluiten. Bovendien hebben sterren met lage een lage snelheid van massaverlies grote Alfvén-oppervlakken. Voor een illustratieve schets, zie Figuur II.

De twee nabijgelegen M dwergen Proxima Centauri (Prox Cen) en AU Microscopii (AU Mic) bieden potentieel geschikte omstandigheden voor het optreden van magnetische ster-planeet interacties. Beide sterren vertonen sterke magnetische velden aan hun oppervlak en zijn gastheren van meerdere bevestigde planeten. In het geval van Prox Cen kunnen recente radiowaarnemingen erop wijzen dat dergelijke interacties plaatsvinden. Om de levensvatbaarheid van magnetische ster-planeet interacties op deze sterren te beoordelen, is het essentieel om de locatie van hun Alfvén-oppervlakken ten opzichte van de planetaire banen te kennen.

Om de locatie van de Alfvén-oppervlakken van Prox Cen en AU Mic te bepalen, gebruik ik in Hoofdstuk 4 magnetohydrodynamische modellen die vergelijkbaar zijn met die gebruikt in Hoofdstuk 2 om 3-dimensionale snapshots van hun stellaire windomgevingen te verkrijgen. Deze modellen werden beperkt met behulp van waarnemingsgegevens en de daaruit verkregen windeigenschappen maken het mogelijk om de locatie van het Alfvén-oppervlak te bepalen. In het geval van Prox Cen, dat een geschatte bovengrens heeft voor zijn snelheid van massaverlies, laat ik zien dat magnetische ster-planeet interacties onwaarschijnlijk zijn. Voor AU Mic is de snelheid van massaverlies echter relatief onbekend. Door de snelheid van massaverlies te variëren, illustreer ik dat er een bepaalde waarde is die beide bekende planeten binnen het Alfvén-oppervlak plaatst. Daarom, als handtekeningen van magnetische ster-planeet interacties worden gedetecteerd van AU Mic, kan er een bovengrens worden gesteld aan de snelheid van massaverlies. Dit illustreert dat de winden van sterren kunnen worden bestudeerd aan de hand van de detectie van magnetische ster-planeet interacties, als aanvulling op de resultaten van Hoofdstuk 3.

Nieuwe methoden voor het identificeren van potentiële sterren op de planeet

Het is duidelijk dat bekende exoplanetaire systemen kunnen worden bestudeerd met behulp van geavanceerde magnetohydrodynamische modellen om te beoordelen of verschillende soorten ster-planeet interacties kunnen optreden. In het geval dat een signatuur van dergelijke interacties wordt gedetecteerd van een ster zonder bekende exoplaneten, hoe bepalen we dan of deze van een planetaire oorsprong is? Dit is een uitdaging voor zeer actieve sterren. Vooral in het geval van kleinere planeten worden de soorten signalen die ze op de ster induceren en die traditioneel worden gebruikt om exoplaneten te vinden, overstemd door de stellaire activiteit. Om deze reden zijn er nieuwe theoretische modellen nodig om dergelijke handtekeningen te interpreteren, vooral bij radiogolflengten.

Recente radio onderzoeken met een breed gezichtsveld zijn begonnen met het detecteren van mogelijke hints van magnetische ster-planeet interacties van M dwergen aan de noordelijke hemel. Tot nu toe is van geen van deze sterren bevestigd dat ze planeten herbergen. Voor WX UMa, een ster in de steekproef van M dwergen die op radiogolflengten is gedetecteerd, is echter eerder het magnetische veld aan het oppervlak in kaart gebracht. Daarom kan een realistische stellaire windomgeving voor de ster worden geconstrueerd, wat ons op zijn beurt in staat stelt de grootte van zijn Alfvén-oppervlak te bepalen.

In Hoofdstuk 5 presenteer ik eerst een stellair windmodel dat voor WX UMa is verkregen op basis van zijn eerder gepubliceerde magnetische veldkaart. Vervolgens ontwikkel ik een model, het eerste in zijn soort, dat de morfologie voorspelt van de radio-emissie die door de ster wordt gegenereerd via magnetische interacties met een planeet. Door het model toe te passen op WX UMa, illustreer ik met dit model dat de waargenomen emissie het best wordt gereproduceerd door een planeet ter grootte van Neptunus die elke 7 dagen rond de ster draait. Hoewel alternatieve emissiemechanismen momenteel niet kunnen worden uitgesloten voor WX UMa, toont de toepassing ervan zijn veelbelovende potentieel voor het identificeren van kandidaat moedersterren van planeten aan de hand van komende radiowaarnemingen.

List of publications

First-author works

- *Radio masers on WX UMa: hints of a Neptune-sized planet, or magnetospheric reconnection?*
  Robert D. Kavanagh; Aline A. Vidotto; Harish K. Vedantham; Moira M. Jardine; Joe R. Callingham; Julien Morin; MNRAS, 514, 675 (2022)
- *Planet-induced radio emission from the coronae of M dwarfs: the case of Prox Cen and AU Mic*
  Robert D. Kavanagh; Aline A. Vidotto; Baptiste Klein; Moira M. Jardine; Jean-François Donati; Dúalta Ó Fionnagáin; MNRAS, 504, 1511 (2021)
- *Radio eclipses of exoplanets by the winds of their host stars*
  Robert D. Kavanagh; Aline A. Vidotto; MNRAS, 493, 1492 (2020)
- *MOVES – II. Tuning in to the radio environment of HD189733b*
  Robert D. Kavanagh; Aline A. Vidotto; Dúalta Ó Fionnagáin; Vincent Bourrier; Rim Fares; Moira M. Jardine; Christiane Helling; Claire Moutou; Joe Llama; Peter J. Wheatley; MNRAS, 485, 4529 (2019)

Co-authored works

- *The strong suppression of galactic cosmic rays reaching AU Mic b, c, and Prox Cen b*
  Amanda L. Mesquita; Donna Rodgers-Lee; Aline A. Vidotto; **Robert D. Kavanagh**; MNRAS, 515, 1218 (2022)
- *One year of AU Mic with HARPS – II. Stellar activity and star–planet interaction*
  Baptiste Klein; Norbert Zicher; **Robert D. Kavanagh**; Louise D. Nielsen; Suzanne Aigrain; Aline A. Vidotto; Oscar Barragán; Antoine Strugarek; Belinda Nicholson; Jean-François Donati; Jérôme Bouvier; MNRAS, 512, 5067 (2022)
- *Coronal Mass Ejections and Type II Radio Emission Variability during a Magnetic Cycle on the Solar-type Star ε Eridani*

Dúalta Ó Fionnagáin; **Robert D. Kavanagh**; Aline A. Vidotto; Sandra V. Jeffers; Pascal Petit; Stephen Marsden; Julien Morin; Aaron Golden; ApJ, 924, 115 (2022)

- *PION: simulating bow shocks and circumstellar nebulae*
  Jonathan Mackey; Samuel Green; Maria Moutzouri; Thomas J. Haworth; **Robert D. Kavanagh**; Davit Zargaryan; Maggie Celeste; MNRAS, 504, 983 (2021)